5-2011

Elastic properties of complex transition metal oxides studied by Resonant Ultrasound Spectroscopy

Yanbing Luan
yluan@utk.edu

To the Graduate Council:

I am submitting herewith a dissertation written by Yanbing Luan entitled "Elastic properties of complex transition metal oxides studied by Resonant Ultrasound Spectroscopy." I have examined the final electronic copy of this dissertation for form and content and recommend that it be accepted in partial fulfillment of the requirements for the degree of Doctor of Philosophy, with a major in Materials Science and Engineering.

Veerle M. Keppens, Major Professor

We have read this dissertation and recommend its acceptance:

George M. Pharr, Chuck L. Melcher, Adriana Moreo

Accepted for the Council:
Dixie L. Thompson

Vice Provost and Dean of the Graduate School

(Original signatures are on file with official student records.)

To the Graduate Council:

I am submitting herewith a dissertation written by Yanbing Luan entitled “Elastic properties of complex transition metal oxides studied by Resonant Ultrasound Spectroscopy”. I have examined the final electronic copy of this dissertation for form and content and recommend that it be accepted in partial fulfillment of the requirements for the degree of Doctor of Philosophy, with a major in Materials Science and Engineering.

Veerle Keppens, Major Professor

We have read this dissertation
and recommend its acceptance:

George Pharr

Chuck Melcher

Adriana Moreo

Accepted for the Council:

Carolyn R. Hodges
Vice Provost and Dean of the Graduate School

(Original signatures are on file with official student records.)

ELASTIC PROPERTIES OF COMPLEX TRANSITION METAL OXIDES STUDIED BY RESONANT ULTRASOUND SPECTROSCOPY

A Dissertation
Presented for the
Doctor of Philosophy
Degree
The University of Tennessee, Knoxville

Yanbing Luan

May 2011

DEDICATION

To my husband and parents, for their love and support

ACKNOWLEDGEMENTS

Looking back at my Ph.D. research, I feel that I am fortunate to have the following people along the way. Without their help, it would have been impossible to finish this work.

First and foremost, I would like to thank Dr. Veerle Keppens, my advisor, who has patiently guided me through ups and downs in my research, and has spent valuable time editing and proofreading this dissertation. I would also like to thank Dr. George Pharr, Dr. Chuck Melcher and Dr. Adriana Moreo for serving on my Ph.D. committee.

I am also thankful to my colleagues Michael Koehler, Lindsay VanBebber, Lin Jia, Ling Li and Jordan Kilbey for their help in equipment maintenance and data analysis. Working with these great people has been a wonderful experience.

I would like to thank Haidong Zhou at National High Magnetic Field Laboratory, Katharina Fritsch and Bruce Gaulin at Mcmaster University for their generous supply of samples in this research. Special thanks go to Ronying Jin, Michael McGuire, Delphine Gout, Athena Safa-Sefat, Brian Sales, David Mandrus and Olivier Gourdon at Oak Ridge National Laboratory for their tremendous help in sample preparation and characterization. I would like to thank Dr. Migliori at Los Alamos National Laboratory for his help in low temperature RUS measurements of $Tb_2Ti_2O_7$.

Finally, I would like to thank the National Science Foundation for providing funding for this research.

ABSTRACT

The elastic properties of novel transition metal oxides have been investigated, using a powerful technique known as Resonant Ultrasound Spectroscopy (RUS). Two sets of transition metal oxides have been studied. One is the ruthenate $Ca_{2-x}Sr_xRuO_4$ series with a layered perovskite structure, a Mott transition system that connects the Mott insulator Ca_2RuO_4 with the unconventional superconductor Sr_2RuO_4. The other set contains geometrically frustrated materials, including vanadium spinels AV_2O_4 (A = Zn, Mn and Fe) and titanate pyrochlores $A_2Ti_2O_7$ (A= Y, Tb, Yb, Ho and Dy).

The elastic response of five $Ca_{2-x}Sr_xRuO_4$ single crystals (x = 2.0, 1.9, 0.5, 0.3 and 0.2) has been measured. For $2.0 \geq x \geq 0.5$, a dramatic softening over a wide temperature range is observed upon cooling, caused by the rotational instability of RuO_6 octahedra (for x = 2.0 and 1.9) or the static rotation of the octahedra (for x = 0.5). For the Ca-rich samples (x = 0.3 and 0.2), the softening occurs in a very narrow temperature range, corresponding to the structural phase transition from high-temperature-tetragonal to low-temperature-orthorhombic symmetry.

Elastic softening in ZnV_2O_4 is observed near the cubic-to-tetragonal structural phase transition at 50 K. The elastic response of MnV_2O_4 is quite unusual, displaying a softening over a wide temperature range with decreasing temperature. Upon cooling, C' of FeV_2O_4 becomes so soft that it drops to almost zero around 140 K, where the cubic-to-tetragonal structural transition occurs.

For $Y_2Ti_2O_7$, all three elastic constants show normal "Varshni" behavior. For spin liquid $Tb_2Ti_2O_7$, all three elastic constants show a pronounced softening below 50 K, indicative of a possible Jahn-Teller, cubic-to-tetragonal transition at very low temperatures. It is also found that the application of a magnetic field suppresses the elastic softening in this compound. Another spin liquid $Yb_2Ti_2O_7$ shows no elastic

softening. The elastic moduli of the spin-ice compounds, $Ho_2Ti_2O_7$ and $Dy_2Ti_2O_7$, show a broad “dip” around 100 K, which is believed to be caused by the strong crystal field effect in those two compounds.

Key words: Elastic Properties, Resonant Ultrasound Spectroscopy (RUS), Transition Metal Oxides (TMO), Geometrically Frustrated Materials

TABLE OF CONTENTS

LIST OF TABLES

LIST OF FIGURES

INTRODUCTION

Transition metal oxides represent a fascinating class of materials with a uniquely wide range of electronic properties and a distinguished, long history. Some of these properties, like the magnetism of loadstone, have been known since antiquity. The fascination in transition metal oxides was first triggered in the 1950s, when the compound $La_{1-x}Ca_xCuO_4$ revealed a variety of physical properties with the change of Ca concentration **(Wollan, 1955)**. Later, novel synthetic approaches, sophisticated computation and simulation methods, and innovative characterization techniques have led to unprecedented progress in the design and development of new generation of advanced materials based on transition metal oxides. The most important landmark in the history of transition metal oxides was the discovery of high-T_c superconductivity in layered cuprates $La_{2-x}Ba_xCuO_4$ **(Bednorz, 1986)** in 1986, which led to a strong upsurge of research interests in transition metal oxides. In addition, multiferroism, the coexistence of magnetism and ferroelectricity, was found in some materials, most of which are transition metal oxides. Those multiferroics are receiving extensive attention due to their potential application in the emerging field of spintronics and sensors. More recently, geometric frustration, an interesting phenomena leading to many exotic ground states, are also found in a variety of transition metal oxides. The electrical, magnetic and optical properties of transition metal oxides find a rich field of important technical applications. A classical example is the wide use of ferrites in electronic devices. Further examples of suitable technological applications include wide gap semiconductors, superconductors and thermoelectric materials, to mention just a few.

Before fully understanding the physics behind the exotic macroscopic properties of transition metal oxides, one has to know two essential microscopic properties of transition metal oxides. First, orbital degree of freedom of electrons in transition metal oxides ensures that the electrons can choose from several types of energetically equivalent electronic orbitals that they could occupy. Secondly, the valence electrons

in these materials interact very strongly and dramatic changes of behavior can be induced by relatively small changes in families of closely related materials. One of the characteristics of transition metal oxides is the coupling between electronic and lattice degrees of freedom. In many cases, this is mirrored by an electronic or magnetic transition which is accompanied by a change of the crystallographic structure. Even though these structural changes in most cases only involve slight distortions of a parent structure, they may induce drastic changes of the physical properties.

Our research focuses on the elastic properties of transition metal oxides, using a novel technique called Resonant Ultrasound Spectroscopy (RUS). The elastic properties of a material are amongst the most important physical properties, and are directly related to the atomic bonding and to quantities such as the sound velocity. In this dissertation, we present our findings on two classes of transition metal oxides. One is the layered ruthenate $Ca_{2-x}Sr_xRuO_4$ series, a Mott transition system that connects the Mott insulator Ca_2RuO_4 with the unconventional superconductor Sr_2RuO_4 and exhibits a variety of physical properties for different x values. The other class is transition metal oxides with geometric frustration, including vanadium spinels AV_2O_4 (A = Zn, Mn and Fe) and titanate pyrochlores $A_2Ti_2O_7$ (A= Y, Tb, Yb, Ho and Dy). The elastic study of those materials will help the understanding of the correlation between the spin, orbital and lattice degrees of freedom.

This dissertation consists of 5 chapters. In Chapter 1, we will briefly summarize the literature on layered ruthenate $Ca_{2-x}Sr_xRuO_4$ series, as well as vanadium spinels AV_2O_4 and titanate pyrochlores $A_2Ti_2O_7$. In Chapter 2, our main experimental apparatus, Resonant Ultrasound Spectroscopy (RUS), will be introduced, and single crystal growth by means of floating zone method will be covered. In Chapter 3, RUS results on the elastic properties of layered ruthenate $Ca_{2-x}Sr_xRuO_4$ series are presented, and the physics behind the experimental results are investigated. In Chapter 4, our experimental data on the vanadium spinels AV_2O_4 and titanate

pyrochlores $A_2Ti_2O_7$ are revealed and discussed. In Chapter 5, a conclusion of the whole dissertation is given.

CHAPTER 1

LITERATURE REVIEW

Transition metal oxides (TMOs) constitute one of the most exciting families of materials, by virtue of the variety of structures and the diversity of properties exhibited by them. In terms of electrical conductivity, they may be good insulators, semiconductors, metals or superconductors. Transition metal oxides are best known to play a vital role in the electronics industry. Aside from their fascinating electronic properties, some transition metal oxides serve as ideal coating materials due to the remarkable mechanical and high-temperature stability together with a strong resistance against corrosion. Many transition metal oxides exhibit high catalytic activity and are widely used in industrial applications.

In this research, we mainly work on the elastic properties of transition metal oxides. Despite the immense interest in these materials, their elastic properties have not received a lot of attention, mainly because the traditional method (pulse-echo) requires large single crystals with dimensions of the order of a centimeter, which are not easily obtained. Using a technique called Resonant Ultrasound Spectroscopy (RUS), we have measured the elastic response of two sets of TMOs. One is the ruthenate $Ca_{2-x}Sr_xRuO_4$ series with a layered perovskite structure, a Mott transition system that connects the Mott insulator Ca_2RuO_4 with the unconventional superconductor Sr_2RuO_4. The other set contains geometrically frustrated materials, including vanadium spinels AV_2O_4 (A = Zn, Mn and Fe) and titanate pyrochlores $A_2Ti_2O_7$ (A= Y, Tb, Yb, Ho and Dy).

1.1 $Ca_{2-x}Sr_xRuO_4$ series

1.1.1 Sr_2RuO_4

In 1994, Maeno et al. **(Maeno, 1994)** discovered that stoichiometric Sr_2RuO_4 is a superconductor with a T_c = 0.93 K. Figure 1.1 clearly shows the superconducting transition in resistivity data within the ab-plane and along the c axis. In spite of the low value of the superconducting transition temperature, the discovery of superconductivity in Sr_2RuO_4 is remarkable since it is the first Cu-free superconductor with a perovskite-related layered structure. Even today, Sr_2RuO_4 represents the only non-cuprate superconductor isostructural with $La_{2-x}Ba_xCuO_4$, as well as the only superconducting ruthenate.

Sr_2RuO_4 is the n = 1 member of the layered Ruddlesden-Popper series $Sr_{n+1}Ru_nO_{3n+1}$ (n = 1, 2, 3 and ∞). The $Sr_{n+1}Ru_nO_{3n+1}$ series includes the superconductor Sr_2RuO_4 (n = 1), the enhanced paramagnet $Sr_3Ru_2O_7$ (n = 2) **(Ikeda, 2000)** and ferromagnetic $Sr_4Ru_3O_{10}$ (n = 3) **(Crawford, 2000)**. It was found that the properties of $Sr_{n+1}Ru_nO_{3n+1}$ series depend strongly on the number of RuO_6 octahedral layers. The structure of the $Sr_{n+1}Ru_nO_{3n+1}$ series is shown in Figure 1.2 **(Iliev, 2005)**. Here we focus on the n = 1 member of this series and its doped varieties.

Sr_2RuO_4 adopts the tetragonal K_2NiF_4 structure with *I*4/mmm space group symmetry. Its lattice parameters are a = b = 3.87 Å and c = 12.74 Å at room temperature. Since most of the isostructural compounds, including the cuprates, exhibit structural phase transition due to the rotation or tilt of the metal oxygen octahedral, it is natural to look for a similar structural transition in Sr_2RuO_4. However, structural analysis of Sr_2RuO_4 **(Braden, 1997)** revealed that the structure remains stable even at low temperatures and no evidence was found for a structural distortion between room temperature and 100 mK.

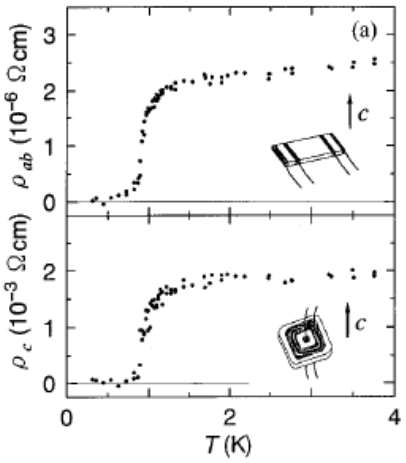

Figure 1.1 Resistivity of early single crystals of Sr_2RuO_4, indicating the superconducting transition **(Maeno, 1994)**

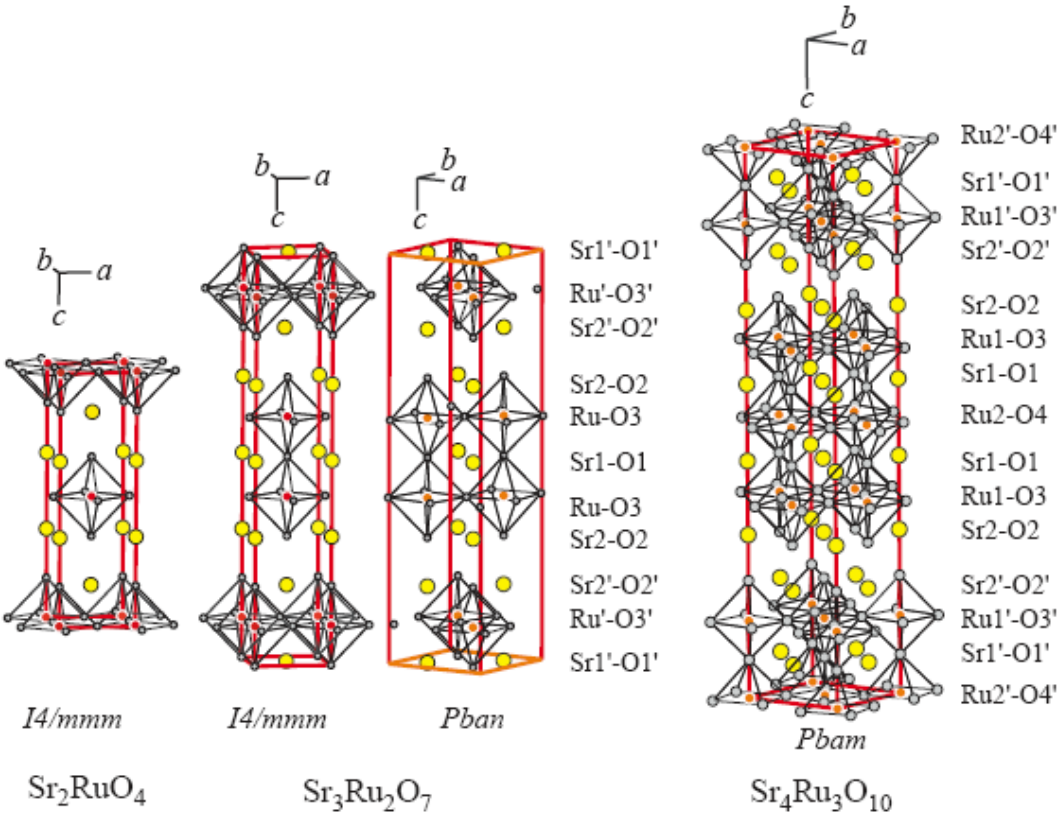

Figure 1.2 Units cells of Sr_2RuO_4 (*I*4/ mmm), $Sr_3Ru_2O_7$ (*I*4/ mmm and Pban) and $Sr_4Ru_3O_{10}$ (Pbam) **(Iliev, 2005)**

In the early work on Sr_2RuO_4 superconductivity, the T_c varied slightly, depending on the quality of the single crystals. The highest T_c result was 1.5 K, obtained from high-quality Sr_2RuO_4 single crystals. The variation of T_c also stimulated a quantitative investigation of impurity effects. It was found that the effects of impurities on the superconductivity of Sr_2RuO_4 were very strong. As seen in Figure 1.3 **(Mackenize, 1998)**, samples with low residual resistivity showed sharp superconducting transitions, and as the residual scattering increased, T_c dropped and the transition became broader, until the superconductivity was destroyed altogether.

The nature of superconductivity in Sr_2RuO_4 has been the subject of extensive research. In 1995, Rice and Sigrist **(Rice, 1995)** argued on theoretical grounds that the superconductivity in Sr_2RuO_4 is an electronic analogue to superfluid ^3He and Sr_2RuO_4 represents an unconventional p-wave spin-triplet superconductor.

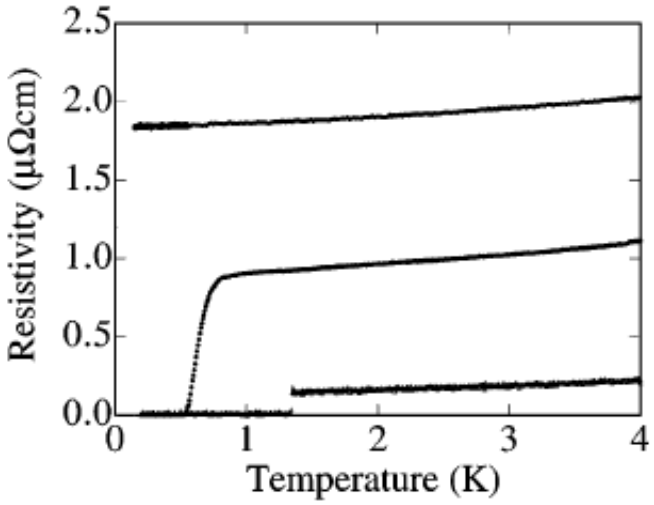

Figure 1.3 Temperature dependence of resistivity for three Sr_2RuO_4 single crystals with residual resistivities of 1.85, 0.85 and 0.15μΩ (from top to bottom) **(Mackenize, 1998)**

Rice's statement was later confirmed by experimental evidences. NMR measurements **(Ishida, 1998) (Ishida, 2001)** and polarized neutron scattering **(Duffy, 2000)** showed that the spin susceptibility remained unchanged across the superconducting transition, indicating spin triplet with the spin of Copper pairs lying within the ab-plane. It needs to be pointed out that even though the p-wave spin triplet superconductivity of Sr_2RuO_4 has been generally accepted, some theoretic calculations **(Mazin, 1999)** showed that the spin fluctuations in Sr_2RuO_4 have both a ferromagnetic (FM) and antiferromagnetic (AFM) component, of comparable magnitude, thus making d-wave superconductivity a strong competitor with the p-wave state. It is possible that the system may be driven to the d-wave superconductivity by an external force, for instance by pressure. Therefore, the nature of superconductivity in Sr_2RuO_4 is still an issue under debate.

Other experimental studies of Sr_2RuO_4 include thermal conductivity measurements **(Tanatar, 2000)**, inelastic neutron scattering studies **(Sidis, 2000)**, susceptibility measurements at high magnetic fields **(Ohmichi, 2001)** and other various studies. It is beyond the scope of this work to give an overview of all studies and their results, considering the large quantities of papers on Sr_2RuO_4. Instead, we will focus on the literature that reports studies of the elastic properties of Sr_2RuO_4. For Sr_2RuO_4 with the tetragonal crystal structure, there are six independent second-order elastic constant C_{ij}, expressed as C_{11}, C_{33}, C_{12}, C_{23}, C_{44} and C_{66}. The elastic tensor of Sr_2RuO_4 was measured on a high-quality single crystal specimen, using Resonant Ultrasound Spectroscopy (RUS) **(Paglione, 2002)**. The obtained elastic constants at room temperature were 2.32, 2.08, 0.71, 1.06, 0.657, 0.612 (unit: 10^{11} Pa) respectively for C_{11}, C_{33}, C_{12}, C_{23}, C_{44} and C_{66}. Those values of elastic constants resulted in a Debye temperature θ_D = 465 K, which can provide information on the possible role of electron-phonon coupling in the superconductivity.

Longitudinal elastic constants C_{11} and C_{33} were measured on a Sr_2RuO_4 single crystal across T_c, using pulse-echo technique **(Okuda, 2002)**. As shown in Figure 1.4,

a drop in the longitudinal elastic moduli was observed at T_c.

Transverse ultrasonic measurements were also performed on a single crystal of Sr_2RuO_4 across T_c and the transverse elastic modulus C_{66} was evaluated from the in-plane transverse sound velocity v, using the equation $C_{66} = \rho v^2$, where ρ is the density **(Okuda, 2003)**. Figure 1.5 shows the temperature dependence of the sound velocity for both the superconducting state at 0 T and the normal state at 1.5 T for Sr_2RuO_4. The jump of C_{66} at T_c (indicated by the arrow) is attributed to the coupling between the strain and the two-dimensional order parameter (OP) with broken time-reversal symmetry. This led to additional evidence for the spin-triplet superconductivity with the two-dimensional OP.

So far, there are no reports on the elastic properties of other concentrations than Sr_2RuO_4 in the $Ca_{2-x}Sr_xRuO_4$ series. Our RUS studies on different concentrations will provide an insight into the thermodynamic properties of this fascinating system.

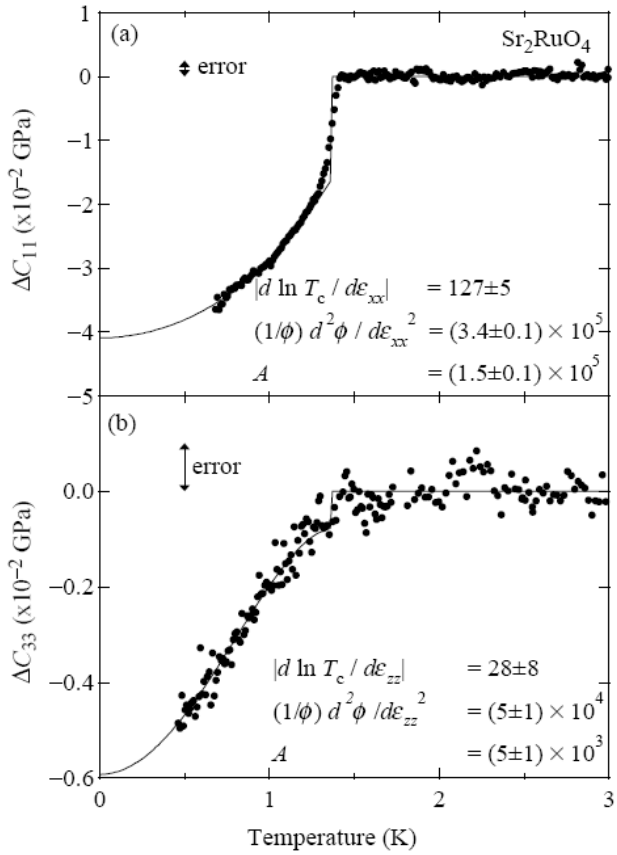

Figure 1.4 The difference in the longitudinal elastic moduli (a) C_{11} and (b) C_{33} across the superconducting transition in Sr_2RuO_4. The solid curves are calculated with a thermodynamic model **(Okuda, 2002)**

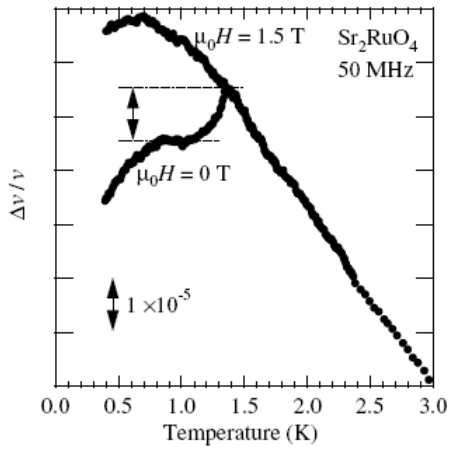

Figure 1.5 The temperature dependence of the sound velocity shown for both the superconducting state at 0 T and the normal state at 1.5 T for Sr_2RuO_4. The arrow indicates the jump of C_{66}, when T_c is approached from low temperature **(Okuda, 2003)**

1.1.2 Ca_2RuO_4

A compound closely related to the superconductor Sr_2RuO_4 is Ca_2RuO_4, which is obtained by the isovalent substitution of Sr by Ca. In contrast to Sr_2RuO_4 which is metallic, Ca_2RuO_4 shows nonmetallic behavior at room temperature. Ca_2RuO_4 is considered to be a Mott insulator, in which suppression of conductivity occurs as a result of strong interactions between electrons in a solid.

The structure of Ca_2RuO_4 is of the same layered perovskite type as that of Sr_2RuO_4. However, unlike the *I4/mmm* tetragonal symmetry in Sr_2RuO_4, Ca_2RuO_4 has the *Pbca* orthorhombic unit cell with the dimensions a = 5.402 Å, b = 5.493 Å, and c = 11.932 Å at room temperature **(Nakatsuji, 1997a)**. The presence of the orthorhombic distortion in Ca_2RuO_4 is attributed to the static rotation of the RuO_6 octahedra about an axis parallel to the c-axis combined with a tilt of the RuO_6 about an axis in ab-plane. The temperature dependence of the structural parameters of Ca_2RuO_4 indicates a structural phase transition at 356 K, as shown in Figure 1.6 **(Friedt, 2001)**. The low-temperature phase is characterized by a small c- lattice parameter (*S - Pbca)* compared to the high-temperature phase with long c (L – *Pbca).* In the temperature dependence of the partial volume fractions of the L – *Pbca* and *S - Pbca* phases, a hysteresis was observed, which indicated the first order nature of this structural transition.

The structural transition in Ca_2RuO_4 is also companied by a metal to insulator transition, as depicted in Figure 1.7 **(Alexander, 1999)**. Figure 1.7 shows the electric conductivity, ρ (T), in the ab plane as a function of temperature for $70 < T < 600$ K. An abrupt transition from a nearly metallic state to an insulating state was observed at 357 K, simultaneously with the structural transition. The metal-insulator transition is Mott-like and not associated with a magnetic transition, and it is primarily due to the coupled electronic elastic energies associated with the structural change. This is not a common phenomenon in Mott insulators, since for most Mott insulators the gap depends only on the existence of moments and is not coupled to the crystal structure.

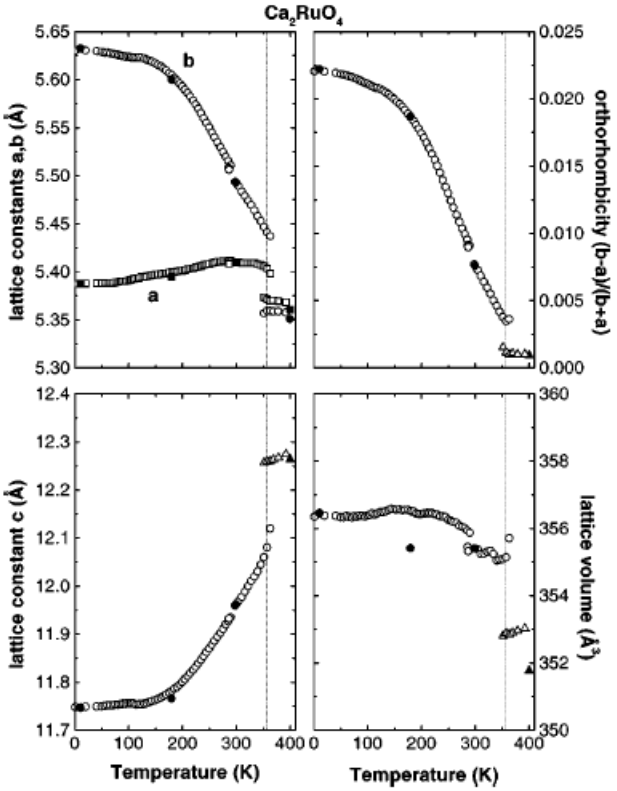

Figure 1.6 The temperature dependence of the lattice parameters in Ca_2RuO_4 **(Friedt, 2001)**

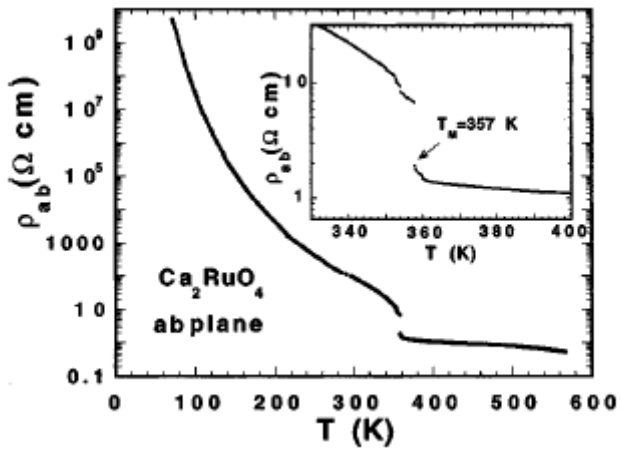

Figure 1.7 Electrical resistivity ρ (T) for the ab plane as a function of temperature for 70 < T < 600 K. Inset: Details of the abrupt jump in ρ (T) near the transition at T_M = 357 K **(Alexander, 1999)**

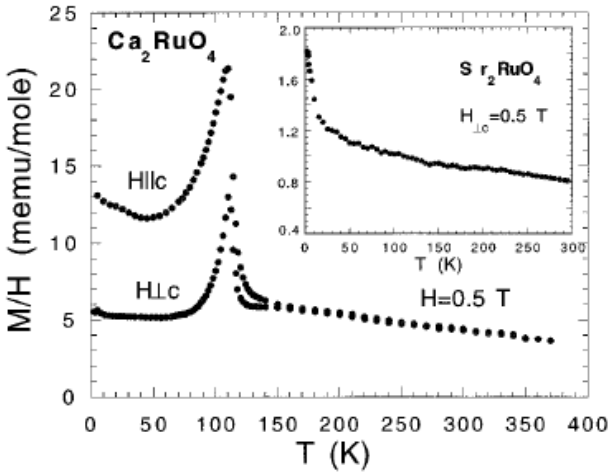

Figure 1.8 Magnetic susceptibility for single-crystal Ca_2RuO_4 **(Cao, 1997)**

In contrast to the ferromagnetic instability suggested for Sr_2RuO_4, Ca_2RuO_4 exhibits antiferromagnetic ordering at $T_N \approx 110$ K, with only a weak ferromagnetic component induced by spin canting **(Nakatsuji, 1997b) (Cao, 1997)**. Figure 1.8 **(Cao, 1997)** shows the magnetic susceptibility of a single crystal Ca_2RuO_4 sample with the applied field parallel and perpendicular to the c axis. A significant cusp is observed at 110 K, a clear evidence of the onset of antiferromagnetism. The transition in Figure 1.8 is more sharply defined than those typical of antiferromagnets. The inset of Figure 1.8 displays the magnetic susceptibility of Sr_2RuO_4 for contrast and its susceptibility is much smaller and less temperature dependent than that of Ca_2RuO_4.

1.1.3 $Ca_{2-x}Sr_xRuO_4$ series

The remarkable discovery of superconductivity in Sr_2RuO_4 stimulated a surge of investigations on the doped $Ca_{2-x}Sr_xRuO_4$ series, connecting the Mott insulator Ca_2RuO_4 with the superconductor Sr_2RuO_4.

It should be noted that since Sr and Ca are isoelectronic, Ca substitution does not change the valence electron numbers, in contrast to carrier doping in the cuprate high-T_c superconductors. The rich physical phenomena in this series result rather from the changes in the interplay between electronic correlations and the band

structures induced by the crystal structure changes **(Wang, 2004)**.

S. Nakatsuji and Y. Maeno **(Nakatsuji, 2000a) (Nakatsuji, 2000b)** first revealed the entire experimental phase diagram of $Ca_{2-x}Sr_xRuO_4$ by resistivity, magnetic susceptibility and x-ray diffraction measurements. The phase diagram, as shown in Figure 1.9 **(Nakatsuji, 2000b)**, exhibits rich behavior, including an antiferromagnetic (AF) transition, a metal-insulator transition (MIT), a structural transition and a ferromagnetic instability. The phase diagram consists of three regions:

(I) $(0 \leq x < 0.2)$ AF insulating ground state

Antiferromagnetic ordering occurs for all $x < 0.2$ compositions. In addition, the metal-insulator transition occurs in this region , and the transition temperature decreases with Sr addition until it reaches zero for $x = 0.2$. Even though for Ca_2RuO_4 ($x = 0$), the metal-insulator transition temperature T_c, which is about 360K, is far above the Néel temperature $T_N = 110$ K, slight doping of Sr can shift T_c and T_N to the same value. Figure 1.10 **(Nakatsuji, 2000a)** clearly indicates the abrupt increase by factors more than 10^4 in resistivity at 155 K and 70 K for $x = 0.09$ and 0.15 respectively.

(Π) $(0.2 \leq x < 0.5)$ Magnetic metallic (M-M) region

In this region, the system becomes metallic at all temperatures with AF correlation at low temperatures. Even though long-range order (LRO) does not emerge, an AF short-range order (AF-SRO) is well stabilized, as evidenced by the broad peak in the temperature dependence of the susceptibility and also by the anisotropy of the susceptibility below the peak temperature.

Another characteristic of region Π is a second-order structural phase transition from high-temperature-tetragonal (HTT) to low-temperature-orthorhombic (LTO) phase. The structural transition temperature is close to room temperature for $Ca_{1.8}Sr_{0.2}RuO_4$ ($x = 2$) and continues to drop to lower temperatures with more Sr addition until it reaches zero at $x_c \underline{\sim} 0.5$.

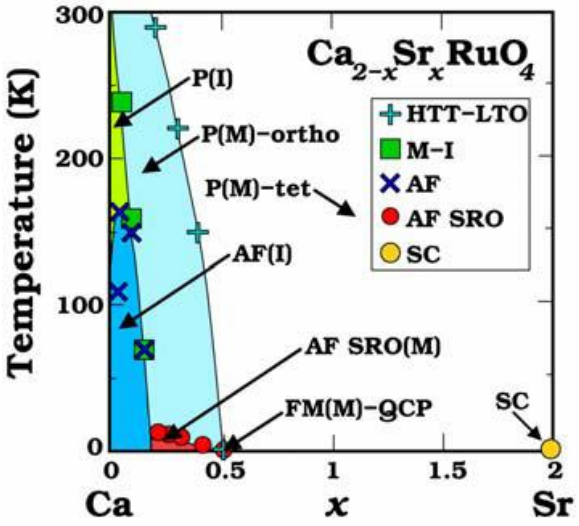

Figure 1.9 Phase diagram of $Ca_{2-x}Sr_xRuO_4$ with abbreviations: P for paramagnetic, AF for antiferromagnetic, FM for ferromagnetic, (M) for metallic phase, (I) for insulating phase, SC for superconducting phase, HTT for high-temperature-tetragonal, LTO for low-temperature-orthorhombic, SRO for short range order and QCP for quantum critical point **(Nakatsuji, 2000b)**

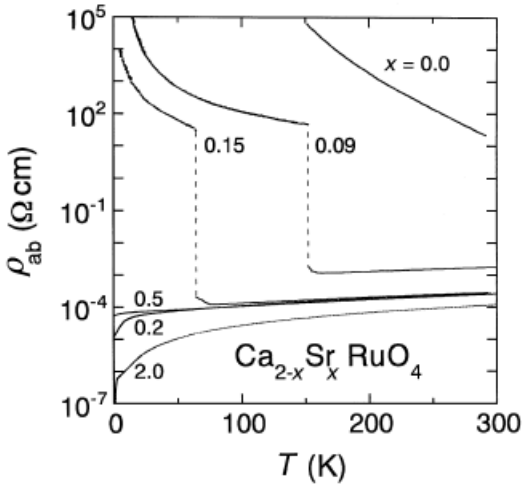

Figure 1.10 Temperature dependence of the in-plane resistivity for $Ca_{2-x}Sr_xRuO_4$ with different values of x **(Nakatsuji, 2000a)**

(III) $(0.5 \leq x \leq 2)$ Paramagnetic metal. Superconductivity emerges at x = 2.

For Sr_2RuO_4, the χ (T) curve is typical for a Pauli-paramagnet, showing little temperature dependence. Upon Ca substitution, however, the susceptibility becomes Curie-Weiss–like. The susceptibility, at the zero temperature limit, increases gradually with increasing Ca concentration until it is substantially enhanced at x_c = 0.5 and reached a value that is more than 100 times larger than the susceptibility of Sr_2RuO_4. The critical enhancement of the low-temperature susceptibility at x_c is correlated to the disappearance of AF-SRO in region Π at $x \simeq 0.5$, indicating a drastic change of the ground state to a nearly ferromagnetic one. The critical enhancement of susceptibility at x_c is also correlated to the zero temperature HTT to LTO structural transition at this point, which is believed to have quantum-critical character **(Nakatsuji, 2000b)**. A quantum-critical phase transition takes place at the absolute zero of temperature, where crossing the phase boundary means that the quantum ground state of the system changes in some fundamental way **(Sondhi, 1997)**.

Figure 1.11 shows the magnetic phase diagram of $Ca_{2-x}Sr_xRuO_4$ constructed using first principle calculations, in the space spanned by structural distortions **(Fang, 2001)**. From right to left of the phase diagram, first the RuO_6 starts to rotate along the c axis by up to 12°, and then with the 12° rotation being fixed, the RuO_6 starts to tilt up to 12°. The basic tendency suggested by this calculated phase diagram is that RuO_6 rotation will drive the system from a non-magnetic (NM) state to a ferromagnetic (FM) state, while the subsequent tilting plus the flattening of RuO_6 will push the system to an antiferromagnetic (AF) region. This general tendency is quite consistent with the experimental phase diagram.

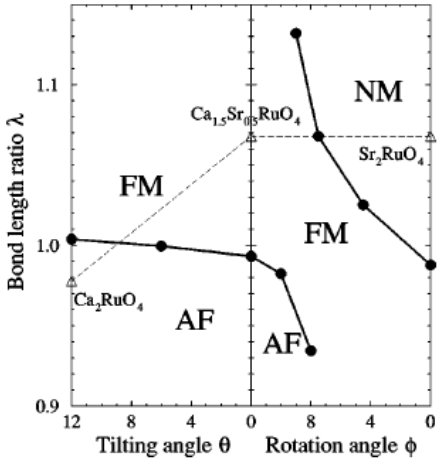

Figure 1.11 The calculated magnetic phase diagram of $Ca_{2-x}Sr_xRuO_4$ with structural distortion. Here, the degree of flattening of RuO_6 octahedron was defined by $\lambda = d_c / d_{ab}$, with d_c (d_{ab}) denoting the Ru-O bond length along the *c* axis (in the *ab* plane) with the RuO_6 volume fixed **(Fang, 2001)**.

1.2 Geometrically frustrated materials

The second class of materials in our study are transition metal oxides with geometric frustration, including vanadium spinels AV_2O_4 (A = Zn, Mn and Fe) and titanate pyrochlores $A_2Ti_2O_7$ (A= Y, Tb, Yb, Ho and Dy). In this section, we will first talk about geometric frustration, an intriguing phenomenon in condensed matter physics, followed by literature reviews on vanadium spinels AV_2O_4 and titanate pyrochlores $A_2Ti_2O_7$.

1.2.1 Geometric frustration

Geometric frustration, a concept developed in the 1950's, has been a topic of interest during recent years **(Ramirez, 1994) (Greedan, 2001) (Bramwell, 2001) (Schiffer, 2002) (Gaulin, 2005) (Moessner, 2006) (Greedan, 2006)**. "Frustration" in physics is a term applied to the situation where the system is unable to find a unique ground state due to competing or conflicting interactions. When frustration arises purely from the geometry or topology of the lattice, it is termed geometric frustration.

A simple example of 2D geometric frustration is the arrangement of three

identical spins on the corners of an equilateral triangle (Figure 1.12 b). The spins are constrained to point either up or down, and the energy is minimized when each spin is aligned opposite to its neighbors. Once the first two spins align anti-parallel, the third one is *frustrated*: it cannot simultaneously minimize its interactions with both of the other spins and its two possible orientations, up and down, give the same energy. In other words, antiferromagnetic interactions are incompatible with triangular lattice symmetry. This situation can be contrasted with the situation for the square planar plaquette in Figure 1.12 a, which is clearly not frustrated under the same constraints. Similarly, in three dimensions, when four identical spins reside on the corner of a tetrahedron, two of the four spins may experience geometric frustration, as illustrated in Figure 1.12 c.

In frustrated systems, triangles and tetrahedra can share corners, edges or even faces (in the case of tetrahedra) to form the lattices which appear in real materials. Four representative geometrically frustrated lattices are illustrated in Figure 1.13 **(Ramirez, 1994)** and include: (a) edge-sharing triangular; (b) corner-sharing triangular, also called Kagome lattice; (c) edge-sharing tetrahedral (which leads to the classic fcc lattice); (d) corner-sharing tetrahedral, also called pyrochlore lattice. Currently, the pyrochlore lattices are attracting considerable attention in geometric frustration research. This type of 3-D network, which can be shown to be the most frustrated of all common lattice types, can be found in the spinels, laves and real pyrochlore type compounds. The primary source of the growing interest in geometrically frustrated materials is the novel and complex phenomena induced by frustration. For example, the presence of geometric frustration can inhibit the formation of long-range ordered spin ground states, even at very low temperatures. Figure 1.14 **(Ramirez, 1994)** illustrates how geometric frustration is quantified in an antiferromagnetic (AF) system. The frustration index is defined as: $F = \theta_{CW} / T_N$, with θ_{CW} the Curie-Weiss temperature, and T_N the Néel temperature. Materials with frustration index more than 10 are considered strongly frustrated.

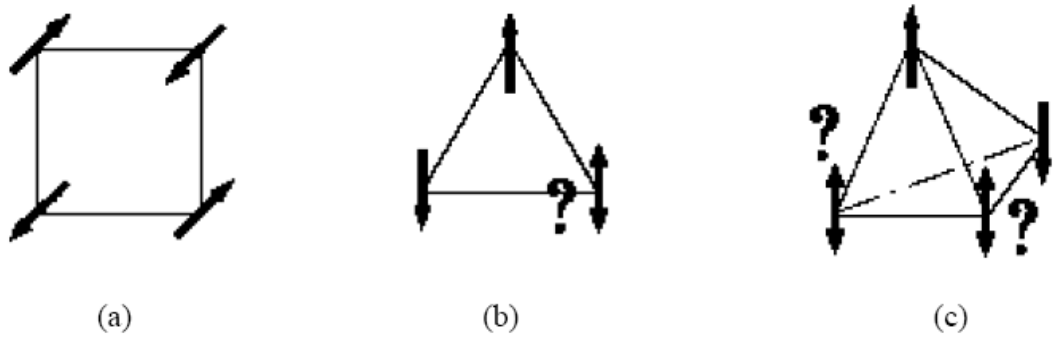

Figure 1.12 (a) square planar plaquette, not frustrated; (b) frustrated triangular plaquette; (c) frustrated tetrahedral plaquette

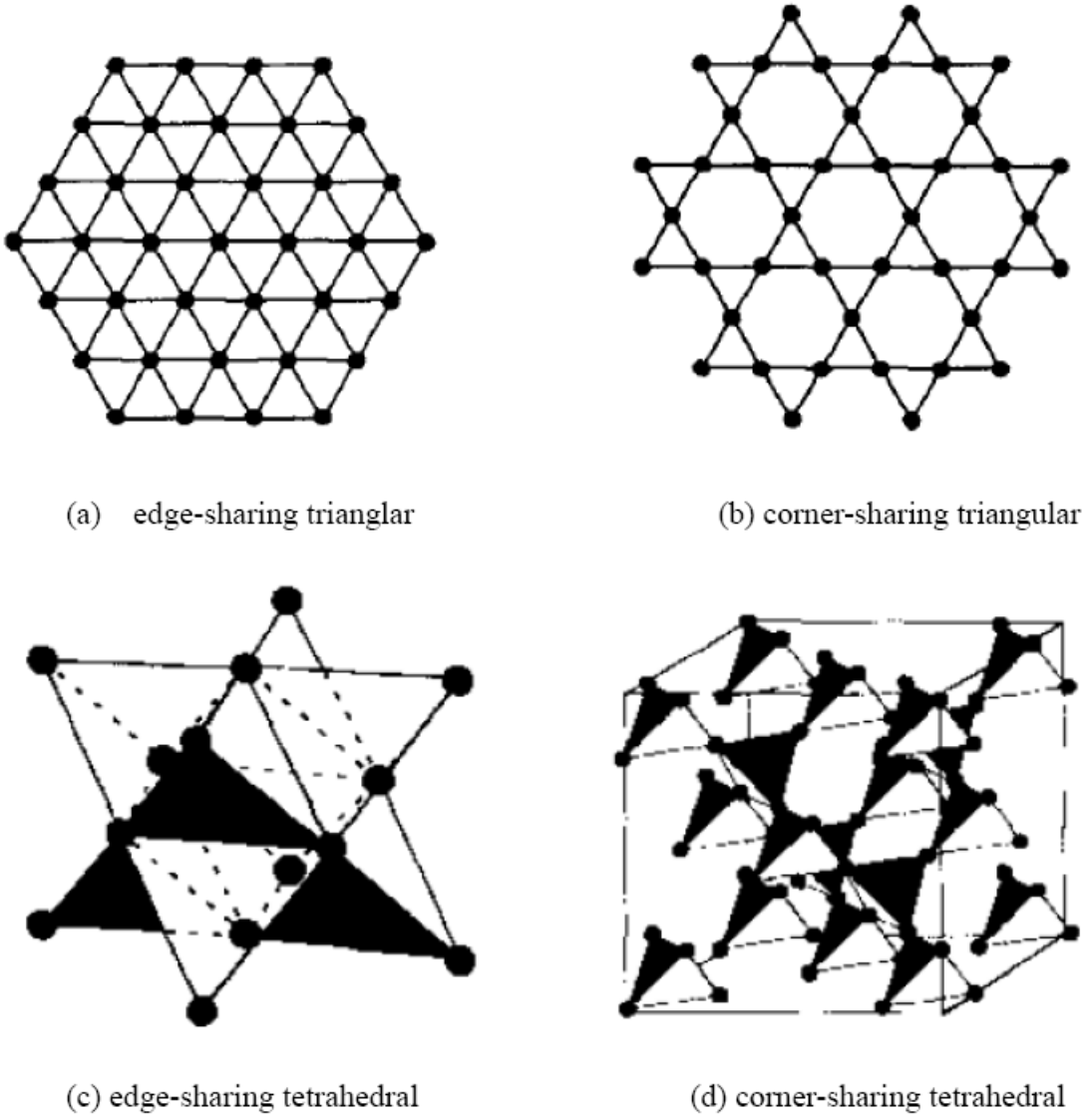

Figure 1.13 Some common frustrated lattices **(Ramirez, 1994)**

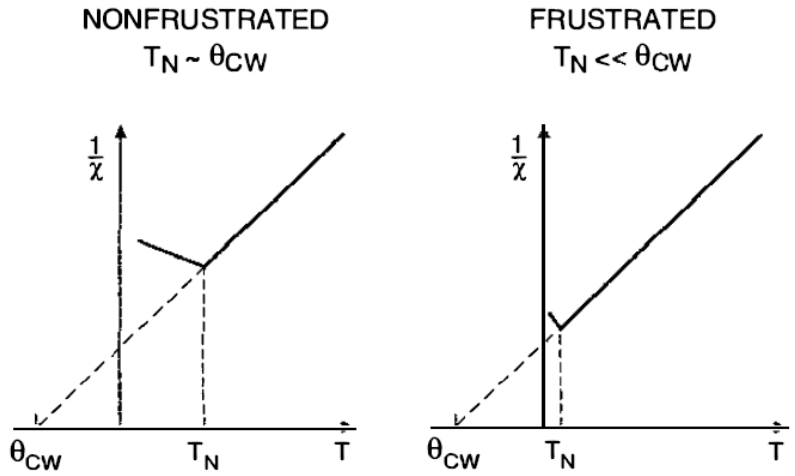

Figure 1.14 How frustration is quantified in an AF system. The left hand side shows a "normal (i.e. non-frustrated) case of the inverse susceptibility, $1/\chi$, versus temperature with $T_N \approx \theta_{cw}$, the Néel, or ordering temperature. The right-hand side shows a frustrated magnet where $T_N << \theta_{cw}$ **(Ramirez, 1994)**

In contrast to conventional materials, the ground state of frustrated system is often macroscopically degenerate, i. e., consists of a macroscopic number of different spin arrangements. How the degeneracy is eventually lifted on cooling is a matter of intense theoretical and experimental interest **(Radaelli, 2005)**. There are several possibilities. The system may distort structurally on cooling to lift the degeneracy and allow long-range charge or spin ordering. Alternatively, the system may settle into a variety of low-temperature cooperative spin states with evocative names such as "spin glass", "spin liquid", or "spin ice", all of which originate from the delicate balance of frustrated spin-spin interaction. Microscopically, the "spin glass" state is a configuration of spins frozen into a more or less random pattern. There exists a distinct freezing or glass temperature, T_f or T_g, below which the random frozen state is established from a random fluctuating state **(Greedan, 2001)**. A "spin liquid" is a cooperative paramagnet and differs from a "spin glass" in that no distinct T_f is observed, *i. e.*, the spins remain dynamic down to the lowest temperatures. A "spin ice" is an unusual system with ferromagnetic interaction, in which the configurational

disorder in the orientations of the magnetic moments is precisely the same as the distribution of protons around O atoms in solid, hexagonal water ice.

Our research interests focus on geometrically frustrated materials based on a pyrochlore lattice, including spinels AB_2O_4 (in which the B-site forms a pyrochlore sublattice) or pyrochlores $A_2B_2O_7$. Those materials play a critical role in the development of current ideas about geometric frustration.

1.2.2 Vanadium spinels AV_2O_4 (A = Zn, Mn and Fe)

1.2.2.1 Spinel structure

The spinel structure, shared by many important oxides, is named after the mineral spinel, $MgAl_2O_4$. Spinels have a general formula AB_2O_4, with A representing a divalent metal ion such as Magnesium, Manganese, Cadmium and Zinc amongst others, and B representing trivalent metal ions, such as Aluminum, Iron, Chromium and Vanadium. Spinels are cubic (space group Fd-3m) with eight formula units in the conventional unit cell. The 32 oxygen ions form a fcc lattice and the 24 cations occupy the tetrahedral and octahedral interstitial sites. Spinel structures can be divided into two types: "normal" and "inverse" spinels. In a "normal" spinel, A^{2+} ions are on the tetrahedral sites (A-sites) and B^{3+} ions are on the octahedral sites (B-sites), $[A]_T[B_2]_OO_4$. In an "inverse" spinel, the A^{2+} ions and half the B^{3+} ions are on octahedral sites and the other half of the B^{3+} are on tetrahedral sties, $[B]_T[AB]_OO_4$. Vanadium spinels AV_2O_4 in this study are normal spinels with V^{3+} cations forming a geometrically frustrated pyrochlore lattice.

1.2.2.2 Orbital degree of freedom in vanadium spinels

For the Heisenberg antiferromagnet on a pyrochlore lattice, the spins would fail to order down to the lowest temperature. In real compounds like vanadium spinels, the magnetic V^{3+}ions form the frustrated pyrochlore lattice and possess an additional

orbital degeneracy due to electron correlation. The physical behavior of those compounds is expected to be dramatically different from that of pure spin models, as the occurrence of an orbital ordering can modulate the spin exchange and partially release the geometrical degeneracy of the underlying lattice **(Jacheli, 2007)**. Vanadium spinels thus give unique opportunity to explore the interplay between strong electron correlation and geometric frustration.

In vanadium spinels, V^{3+} has the electronic configuration [Ar] $3d^{2+}$. As is widely known, there are five 3d orbitals with different orientations, as shown in Fig. 1.15. In an isolated atom, all *d* orbitals have the same energy. However, in an octahedral crystal field, the fivefold d levels of vanadium cation split into twofold e_g levels (d_{x2-y2} and d_{z2}) and three fold t_{2g} levels (d_{xy}, d_{yz}, d_{xz}), as illustrated in Fig. 1.16 **(Motome, 2005)**. In the octahedral environment of the V-atom, the e_g orbitals point toward the oxygen anions, so they are higher in energy and hybridize more strongly with the oxygen p orbitals. In accordance with Hund's rule, the two d electrons of V^{3+} have spin S = 1 and occupy two out of the three low-energy t_{2g} orbitals. Thus, vanadium ions have an orbital degree of freedom, in addition to lattice vibrations and spin. At high temperatures, the occupation of t_{2g} orbitals is expected to be random. However, as the system cools, it is expected to undergo a symmetry breaking "orbital ordering" transition in which an orbital occupation pattern develops along with a tetragonal distortion of O_6 octahedron. The distortion is called Jahn-Teller distortion, which can reduce energy by reducing the symmetry and lifting the degeneracy of t_{2g} orbitals. Since t_{2g} electrons may have a nonzero orbital angular momentum, spin-orbit coupling may play an important role in the physics of vanadium spinels **(Motome, 2005)**.

.

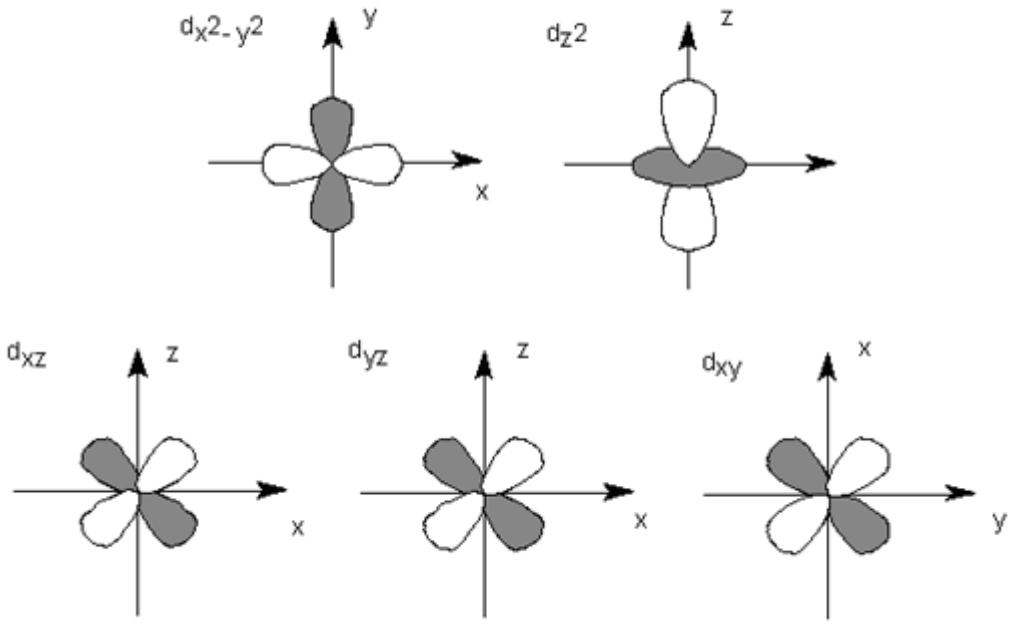

Figure 1.15 Images of five 3d-orbitals with different orientation

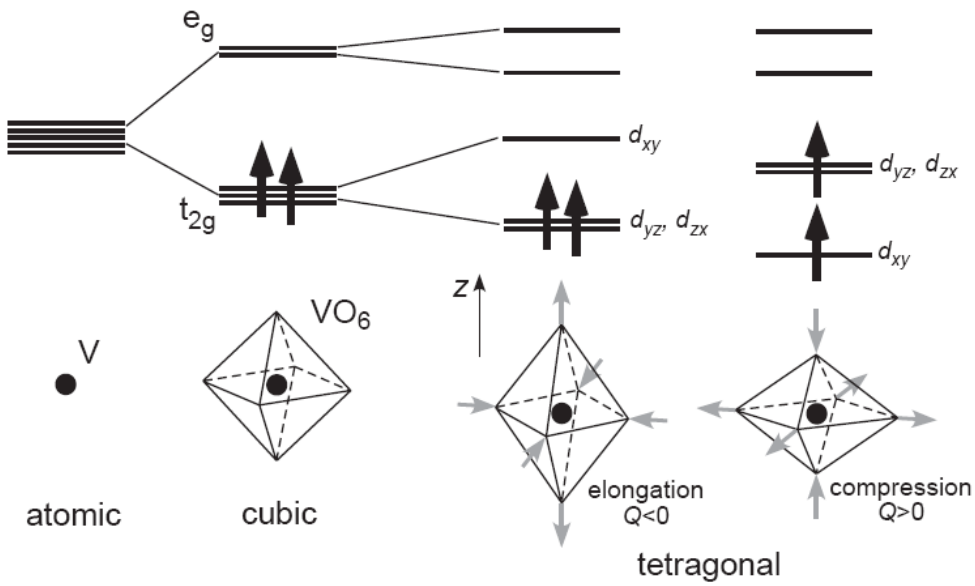

Figure 1.16 Crystal-field splitting of d levels and Jahn-Teller distortion **(Motome, 2005)**

1.2.2.3 ZnV_2O_4

ZnV_2O_4 undergoes two successive transitions at low temperatures **(Ueda, 1997)**. At T_S = 50 K, ZnV_2O_4 undergoes a cubic-to-tetragonal structural phase transition. At lower temperature T_N = 40 K, the system orders antiferromagnetically. In spite of extensive theoretical studies, there still exists controversy about the mechanism behind the two transitions. The main difficulty in obtaining a consistent theoretical picture is that the energy scales in the problem are poorly separated with Jahn-Teller, spin orbit, and magnetic interactions all having the same energy scale. One scenario proposed by Yamashita and Ueta **(Yamashita, 2000)** is based on a valence-bond-solid (VBS) approach and the effects of Jahn-Teller distortion are examined. It is proposed that the transition at T_S is due to the spin-driven Jahn-Teller effect which lifts the degeneracy of the spin-singlet local ground states at each tetrahedron unit of the pyrochlore lattice. This scenario is quite appealing, but it is difficult to explain the magnetic order below T_N, based on this quantum-spin picture. Tsunetsugu and Motome **(Motome, 2005)** **(Tsunetsugu, 2003)** propose a different scenario based on the Kugel-Khomskii Hamiltonian. In their scenario, the structural phase transition at T_S is an orbital order transition assisted by the Jahn-Teller distortion. This orbital order induces spatial modulation of the spin-exchange coupling depending on the bond direction. This partially releases the frustration and leads to a spin order observed at T_N = 40 K. This scenario is corroborated by recent inelastic neutron scattering experiments **(Lee, 2004)**, but the problem is that the symmetry of the crystal structure in this scenario is inconsistent with the spatial symmetry $I4_1/amd$ predicted by X-ray scattering experiments. This issue was later addressed by Tchernyshyov **(Tchernyshyov, 2004)**. His alternative model, which takes into the relativistic spin-orbit interaction, has $I4_1/amd$ crystallographic symmetry and is able to account for the observed magnetic structure. Figure 1.17 demonstrates two predicted orbital ordering pattern for ZnV_2O_4.

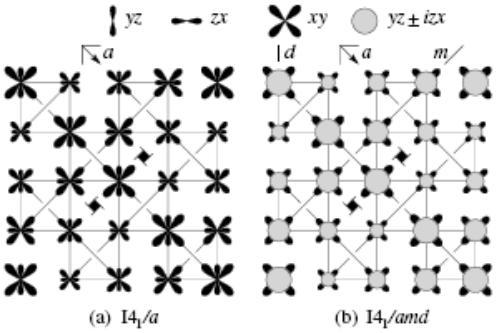

Figure 1.17 Two predicted orbital ordering patterns for ZnV_2O_4. The left pattern is from Tsunetsugu and Motome **(Motome, 2005) (Tsunetsugu, 2003)**, which is based on Kugel-Khomskii Hamiltonian and does not include spin-orbit coupling. The right pattern is from Tchernyshyov **(Tchernyshyov, 2004)** and is based on a model in which spin-orbit coupling is dominant.

1.2.2.4 MnV_2O_4

Recent attention has turned to MnV_2O_4, which, unlike ZnV_2O_4, has magnetic ions Mn^{2+} at A sites, leading to a superexchange interaction between Mn^{2+} and V^{3+}. In this compound, Mn^{2+} ion is in the $3d^5$ high-spin configuration S = 5/2 with no orbital degrees of freedom.

Studies on MnV_2O_4 demonstrated that this compound also undergoes two successive transitions at low temperatures: a ferrimagnetic phase transition at T_N = 56 K, where Mn spins and V spins align in the opposite direction, and a cubic-to-tetragonal structural transition at a lower temperature T_S = 53 K **(Plumier, 1987) (Plumier, 1989) (Plumier, 1998) (Adachi, 2005)**. Neutron diffraction on MnV_2O_4 clearly demonstrated the occurrence of a tetragonal distortion, evidenced by the splitting of the (400) peak into two peaks $(220)_T$ and $(004)_T$ in the tetragonal cell, shown in Figure 1.18 **(Garlea, 2008).** It is noteworthy that T_N reported here is higher than T_S in MnV_2O_4, opposite to most other frustrated spinels, such as ZnV_2O_4 discussed above, where T_S is higher than T_N. To understand the physics behind the behavior of MnV_2O_4, it is informative to compare it with the isostructural ZnV_2O_4. Although neighboring V spins in ZnV_2O_4 have a strong antiferromagnetic interaction, they fail to find a stable antiferromagnetic ordering due to geometric frustration.

Antiferromagnetic ordering occurs in this compound only after a cubic-to-tetragonal structural transition relieves the geometric frustration. In this case, the spin-orbit coupling is an orbital-ordering-driven one. In MnV_2O_4, on the other hand, there is an additional superexchange antiferromagnetic interaction between Mn and V, which leads to ferrimagnetic ordering at T_N. This ferrimagnetic state gives a ferromagnetic configuration of V spins, which changes the orbital-orbital interaction between neighboring V sites, and at some point results in the orbital ordering and structural phase transition at T_S. In this sense, the spin-orbit coupling in MnV_2O_4 is a magnetic-ordering-driven one. The observed magnetic field switching of crystal structure can also be explained by the same scenario. When a magnetic field is applied, the ferromagnetic configuration of V spins occurs at higher temperatures, and accordingly the orbital ordering (structural phase transition) occurs at higher temperatures **(Katsufuji, 2006)**.

However, there still exists controversy about the temperatures of the two transitions in MnV_2O_4, as there are reports that the ferrimagnetic phase transition and structural transition occur simultaneously at 57 K **(Suzuki, 2007)**. More work needs to be done to fully understand its complex physics. So far, there have been no reports on its elastic properties and our RUS measurement may provide additional insight in the coupling between spin, orbit and lattice in this compound.

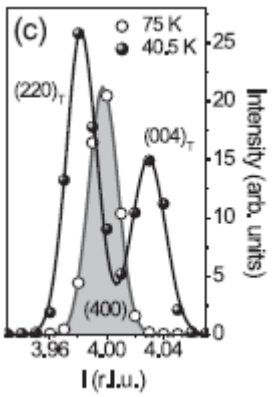

Figure 1.18 Neutron diffraction of MnV_2O_4, showing the spitting of the (400) cubic peak into two tetragonal peaks $(220)_T$ and $(004)_T$ **(Garlea, 2008)**

1.2.2.5 FeV_2O_4

Like MnV_2O_4, FeV_2O_4 has magnetic ions at both A sites and B sites. However, there is an additional degree of complexity, as the Fe^{2+} ion has the $3d^6$ high-spin electron configuration with orbital degrees of freedom.

It is found that FeV_2O_4 exhibits successive structural transitions at low temperatures **(Tanaka, 1966)**. Figure 1.19 **s**hows X-ray powder diffraction measurements on this compound, demonstrating structural phase transitions from cubic to tetragonal at 140 K, from tetragonal to orthorhombic at 110 K, and from orthorhombic to tetragonal at 70 K **(Katsufuji, 2008)**. In addition, magnetization measurement on FeV_2O_4 shows a ferrimagnetic transition at 110 K, similar to that of MnV_2O_4. The simultaneous occurrence of ferrimagnetic ordering and a structural phase transition at 110 K indicates the coupling between magnetism and the crystal structure.

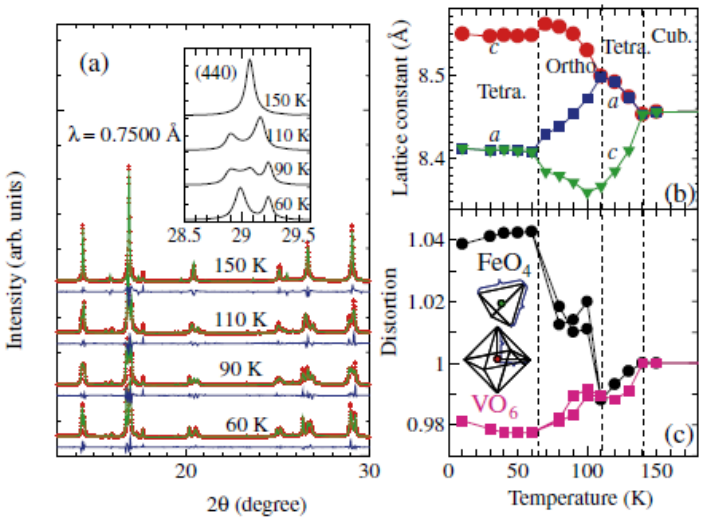

Figure 1.19 (a) X-ray powder diffraction patterns of FeV_2O_4; (b) Temperature dependence of lattice constants obtained from X-ray powder diffraction data; (c) Temperature dependence of the ratio of the O-O bond along the <101> to that along the <110> direction around Fe (closed circles), and the ratio of the V-O bond along the <001> to that along the <100> direction (closed squares), obtained from X-ray powder diffraction data **(Katsufuji, 2008)**

1.2.3 Titanate pyrochlores $A_2Ti_2O_7$ (A= Y, Tb, Yb, Ho and Dy)

The $A_2B_2O_7$ pyrochlore family crystallizes into a face centered cubic structure with eight formula units per conventional unit cell. In the $A_2B_2O_7$ pyrochlores of interest to our study, the A-sites (16d) are occupied by a trivalent rare earth and the B-sites (16c) by Ti^{4+}. The sublattices formed by each of the two metal ions result in two infinite, interpenetrating networks of corner-sharing tetrahedra, as shown in Figure 1.20 **(Gingras, 2000)**. If A, B or both are magnetic and the nearest-neighbor exchange interaction is antiferromagnetic, the system is highly geometrically frustrated. As a result, antiferromagnetically coupled classical Heisenberg spins on the pyrochlore lattice do not develop any long range order at any nonzero temperature, opening up new avenues for novel intrinsically quantum mechanical effects to emerge at low temperatures.

Many materials adopt this structure and titanate pyrochlores $A_2Ti_2O_7$ are being studied extensively. The titanate pyrochlores in our research include five compounds $Y_2Ti_2O_7$, $Tb_2Ti_2O_7$, $Yb_2Ti_2O_7$, $Ho_2Ti_2O_7$ and $Dy_2Ti_2O_7$.

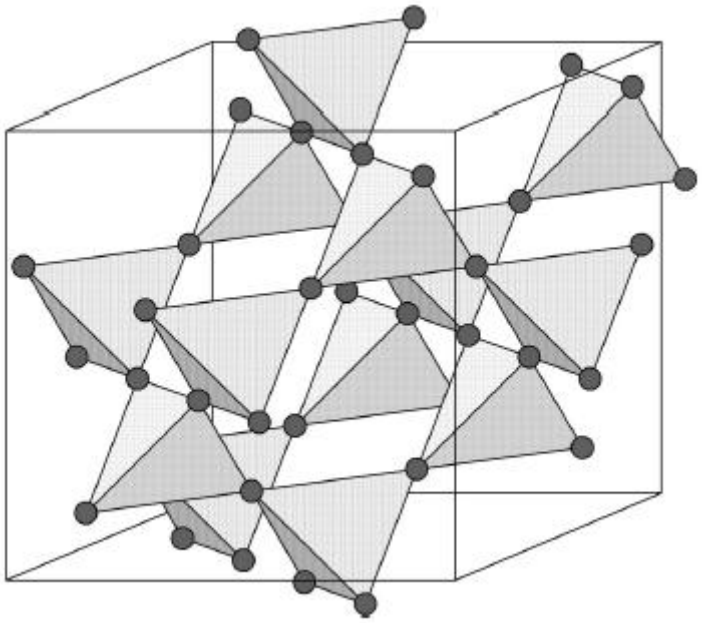

Figure 1.20 Corner-sharing tetrahedra in $A_2B_2O_7$ pyrochlore lattice **(Gingras, 2000)**

1.2.3.1 $Y_2Ti_2O_7$

Whereas Yttrium titanate $Y_2Ti_2O_7$, often abbreviated as YTO, has attracted attention for a number of applications **(Higashi, 2005) (Kramer, 1994)**, it is diamagnetic, and therefore rather uninteresting for studies of magnetism and geometric frustration. However, due to this "boring" magnetic behavior, it is expected to be an excellent reference compound for more complex titanate pyrochlores. So far, there are only a few reports on the theoretical prediction of elastic constants for single crystal $Y_2Ti_2O_7$ **(Pruneda, 2005) (Jiang, 2010)** and discrepancies exist among those reports, especially C_{44} values. No reported experimental results are available to confirm those predictions and our RUS measurement on $Y_2Ti_2O_7$ can be used to compare with the theoretical studies and will surely contribute to the understanding of elastic properties of the titanate pyrochlores.

1.2.3.2 Spin liquid $Tb_2Ti_2O_7$ and $Yb_2Ti_2O_7$

Terbium titanate, $Tb_2Ti_2O_7$, is believed to be a prime example of a spin liquid and has been extensively studied. In a perfect spin liquid, though the magnetic moments are strongly correlated, they remain paramagnetic to zero temperature, but a magnetically ordered ground state can often be stabilized upon the application of pressure or a magnetic field. Despite the onset of antiferromagnetic short-range order at ~ 50 K, $Tb_2Ti_2O_7$ displays no signs of long-range magnetic ordering down to at least 70 mK, as evidenced by the absence of anomalies in the susceptibility at low temperatures in Figure 1.21 **(Gardner, 1999)**. $Tb_2Ti_2O_7$ is thus believed to be a cooperative paramagnet, a term coined to describe such a low temperature state. There exists significant evidence, especially from neutron scattering **(Gardner, 2001)**, that strong magnetic correlations exist on a nearest neighbor length scale, ~ 5 Å, down to very low temperature. To date, $Tb_2Ti_2O_7$ appears to be the best realization of a spin liquid in three dimensions. However, the application of pressure of 8.6 GPa on

$Tb_2Ti_2O_7$ can suppress the spin fluctuation and induce long-range antiferromagnetic ordering at a Néel temperature of 2.1 K **(Mirebeau, 2004)**. High-resolution X-ray scattering measurements on a single crystal of $Tb_2Ti_2O_7$ show continuous broadening of allowed Bragg peaks below ~ 20 K, consistent with the development of fluctuations above a cooperative Jahn-Teller, cubic-to-tetragonal phase transition at very low temperatures **(Ruff, 2007)**. In the most recent X-ray diffraction studies on $Tb_2Ti_2O_7$ in pulsed magnetic fields, Bragg peaks split at a critical field of H ~ 29 T at low temperatures, which is a hallmark of a symmetry-lowering structural phase transition **(Ruff, 2010)**.

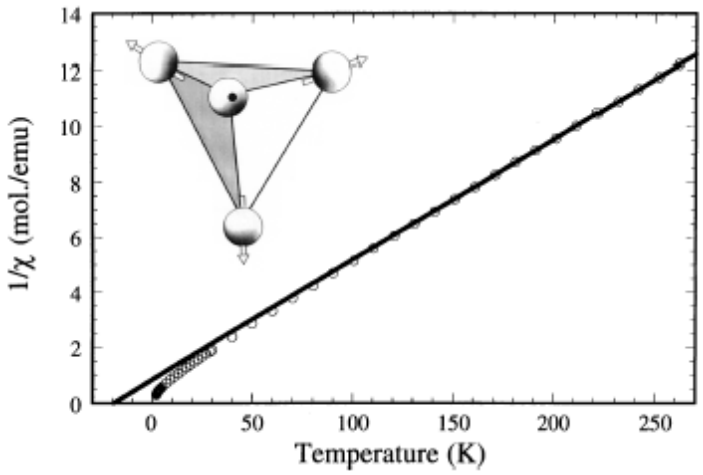

Figure 1.21 The temperature dependence of the inverse susceptibility for $Tb_2Ti_2O_7$, along with a fit of the high temperature regime of this data to a Curie-Weiss form. The inset shows the assumed local arrangement of moments on a single tetrahedron **(Gardner, 1999)**.

Ytterbium titanate, $Yb_2Ti_2O_7$, has been studied in some detail. It is an insulator with lattice parameter a_0 = 10.028 Å at room temperature **(Brixner, 1964)**. A sharp anomaly in the specific heat at 0.25K had long been interpreted as a phase transition to an ordered magnetic state, which was supported by a detailed magnetization study indicative of weak ferromagnetic coupling and a free ion moment of 3.34 μ_B **(Bramwell, 2000)**. However, spin dynamics studies by Hodges and co-workers **(Hodges, 2002)** indicated a different low-temperature scenario. As shown in Figure 1.22, they disclosed an abrupt change in the fluctuation rate of the Yb^{3+} spin at 0.24 K which corresponds to the temperature of the heat capacity anomaly. Below 0.24 K, Yb^{3+} spin fluctuation slows down by more than three orders of magnitude to several megahertz without freezing completely. This finding evidenced a first-order transition at 0.24 K which does not correspond to a transition from a paramagnetic state to a ferromagnetic state. Instead, the transition mainly concerns the time domain and involves the drastic slowing down of the spin fluctuations. The neutron powder diffraction confirmed this finding since no extra Bragg intensity was found below 0.24 K. A recent polarized neutron study by Gardner **(Gardner, 2004)** conclusively confirmed this fluctuating picture and ruled out the frozen ferromagnetic state. Now it seems well established that $Yb_2Ti_2O_7$ is a spin liquid with spins continuing to fluctuate below the 0.24 K transition.

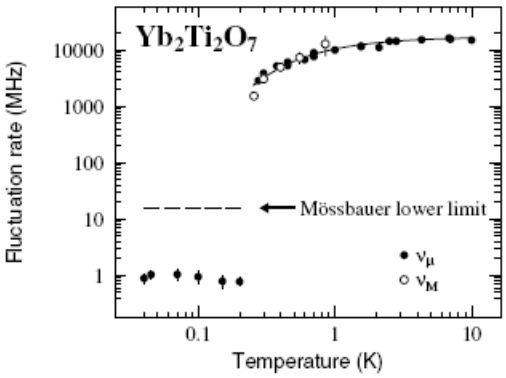

Figure 1.22 The fluctuation rate for Yb^{3+} as a function of temperature derived from muon (filled circle) and Mossbauer (open circles) spectroscopy. Note the first-order change at 0.24 K **(Hodges, 2002)**

1.2.3.3 Spin ice $Ho_2Ti_2O_7$ and $Dy_2Ti_2O_7$

A spin ice is a highly unusual magnet, since it does not order to the lowest temperatures even though it appears to have ferromagnetic interactions. There are only a few confirmed spin ice pyrochlores, which are $Ho_2Ti_2O_7$, $Dy_2Ti_2O_7$, $Ho_2Sn_2O_7$ and $Dy_2Sn_2O_7$.

Holmium titanate, $Ho_2Ti_2O_7$, was the first material proposed as a spin ice system. In 1997, Harris and collaborators **(Harris, 1997)** reported that, in zero applied magnetic field, neutron scattering on $Ho_2Ti_2O_7$ detects no evidence of a transition to long range order down to at least 0.35 K. The most surprising part of the results was that the Curie-Weiss temperature was found to be positive with $\theta_{cw} \sim +1.9$ K, indicating ferromagnetic coupling between the Ho^{3+} ions with J ~ 1 K. When a magnetic field is applied, its ground state degeneracy is broken and ordered magnetic phases are formed which display unusual history dependence. The behavior of $Ho_2Ti_2O_7$ fits well within the proposed "spin ice" model, which is a model of a ferromagnetic pyrochlore with local Ising anisotropy directed along the <111>-type directions. The ground state of Ho^{3+} spins is characterized by the simple arrangement of two spins "in" toward the center of its tetrahedron and two spins "out" of the tetrahedron, which is equivalent of the water ice rule "two protons near, two protons far" , as illustrated in Figure 1.23 **(Gardner, 2010)**. Just as water ice has extensive proton disorder entropy, spin ice $Ho_2Ti_2O_7$ also exhibits low-temperature residual entropy.

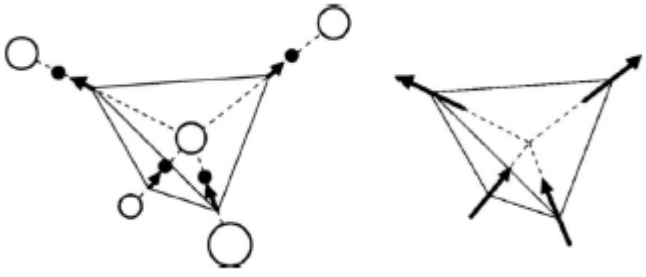

Figure 1.23 Illustration of the equivalence of the proton arrangement in water ice (left) and the spin arrangement in spin ice (right) **(Gardner, 2010)**

The unusually large hyperfine interaction between the nuclear and electronic spins of Ho^{3+} makes $Ho_2Ti_2O_7$ unsuitable for low temperature specific heat measurements. The first compelling thermodynamic evidence for the existence of a spin ice state in Ising pyrochlore systems was therefore obtained via measurements of the magnetic specific heat on another identified spin ice system: dysprosium titanate $Dy_2Ti_2O_7$ **(Ramirez, 1999)**. From the specific heat data, the residual spin entropy of $Dy_2Ti_2O_7$ was inferred, which is numerically in excellent agreement with Pauling's prediction for the entropy of water ice S = R (ln2 – ½ ln 3/2), as illustrated in Figure 1.24. This finding has provided the crucial link in the chain between spin ice and water ice.

The spin ice phenomenon exemplifies the richness of the intrinsic physics of geometric frustration and will continue to capture extensive attention for years to come.

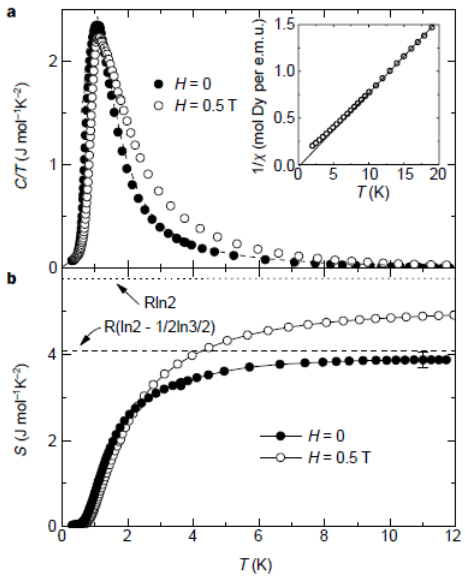

Figure 1.24 (a) Specific heat and (b) entropy of the spin ice compound $Dy_2Ti_2O_7$, showing agreement with Pauling's prediction for the entropy of water ice S = R (ln2 – ½ ln 3/2) **(Ramirez, 1999)**

CHAPTER 2

EXPERIMENTAL DETAILS

2.1 Resonant Ultrasound Spectroscopy (RUS)

Resonant Ultrasound Spectroscopy (RUS) is a relatively new technique to determine the elastic constants of solids, based on the measurement of the mechanical resonances of a freely vibrating body. The origins of RUS are traceable to the geophysics community, where solutions are needed that utilize the Earth's free-oscillation modes (e.g. excited by a major earthquake) to accurately measure the elastic moduli of materials believed to be Earth's constituents. A RUS-like method was first used for materials science problems in 1964 by Fraser and LeCraw, who used a one-transducer setup to find the elastic constants for a sphere of isotropic materials **(Fraser, 1964)**. Later, the method of Fraser and LeCraw was improved by geophysicists Anderson, Schreiber and Soga, who introduced the so-called resonance sphere technique (RST) and generated great sensation when they successfully measured the elastic moduli of small spherical lunar samples in 1970 **(Schreiber, 1970)**. In 1971, Demarest **(Demarest, 1971)** made a great breakthrough by developing the computational procedures to find the elastic moduli for a rectangular parallelepiped of an anisotropic, crystalline material with the axis of the sample oriented along high-symmetry crystallographic directions. Demarest's method was later referred to as the rectangular parallelepiped resonance (RPR) method, which has been used extensively since then. With the advantage of modern computing power, RUS in its present form was developed in 1988 by Migliori and Visscher, and was turned into a powerful method for measuring elastic constants of materials of a wide variety of shapes and symmetry **(Migliori, 1993) (Schwarz, 2000) (Zadler, 2004) (Migliori, 2008)**. Recent theoretical advances indicate that RUS technique in principle can be applied to any well-defined shape and to materials with any crystallographic symmetry.

Traditionally, the elastic constants of solids have been derived from measurements of the phase velocity of plane acoustic waves. Among the conventional techniques, the most used one is called pulse-echo method, the basic idea of which is to launch an acoustic pulse into a specimen and measure the time it takes to reflect from the face of the specimen opposite the transducer. From the measurement, the sound velocities are calculated and the elastic constants are obtained from sound velocities for various propagation and polarization directions. This technique, although quite powerful, suffers from certain limitations. Among the major restrictions are: (a) relatively large samples are required for accurate measurements, (b) a number of independent measurements, often on separate samples, are needed to fully characterize the elastic properties of a material **(Leisure, 1997)**. Those drawbacks can be avoided when using RUS, which, instead of relying on the plane-wave approximation, measures the resonant frequencies of samples of well-defined shapes and match the measured lines with the calculated spectrum to deduce the elastic tensor. This allows the accurate determination of all of the elastic constants in a single measurement, which clearly indicates a main advantage of RUS. The second advantage lies in the ability of RUS to work with small samples of mm dimensions or smaller, which is especially important when large single crystals are not available. Another advantage is the accuracy of RUS measurement, due to the fact that no bonding exists between sample and transducer, and minimal loading closely simulates stress-free boundary conditions. More remarkably, RUS has been used for the simultaneous determination of both the elastic constants and the crystalline orientation of a tantalum single crystal **(Sarrao, 1994a)**. In addition, RUS shows great promise for the study of processing-induced weak elastic anisotropy in some polycrystalline materials. RUS is especially sensitive to this anisotropy because all the elastic constants can be measured simultaneously. Over the past 20 years, RUS has become an attractive and versatile technique in materials science, condensed matter physics, and engineering.

2.1.1 Elastic tensor

As second derivatives of the free energy with respect to strain, elastic constants are directly related to the atomic bonding of the material and are of fundamental importance. They are closely connected to thermodynamic properties of the material, such as the specific heat, the Debye temperature and the Gruneisen parameter (which relates the thermal expansion coefficient to the specific heat at constant volume) and they can be used to check theoretical models **(Maynard, 1996)**. The elastic properties also play an important role in probing various phase transitions. Unlike most of the quantities used to characterize condensed matter, the elastic constants are fourth-rank tensors containing a wealth of detailed directional information about the material.

Materials are generally deformed when forces are applied. For linear elasticity, a generalized Hooke's Law holds so that

$$\sigma_{ij} = C_{ijkl}\varepsilon_{kl} \qquad (2.1)$$

where σ_{ij} is applied stress, C_{ijkl} are the elastic constants and ε_{kl} is the resulting strain. For a three dimensional object, it appears that C_{ijkl} is a 9×9 matrix with 81 elastic constants. Voigt-notation can simplify the 9×9 matrix to a 6×6 matrix with 21 independent elastic constants, as in equation (2.2). Only the lowest-symmetry crystal, triclinic with a one-fold axis of rotation, has 21 independent elastic constants. In high-symmetry crystals, this number is considerably reduced by mirror planes and n-fold rotation axes. For example, a single crystal with cubic symmetry has only 3 independent elastic constants and an isotropic material has only 2.

$$\begin{pmatrix}\sigma_1\\ \sigma_2\\ \sigma_3\\ \sigma_4\\ \sigma_5\\ \sigma_6\end{pmatrix} = \begin{pmatrix} c_{11} & c_{12} & c_{13} & c_{14} & c_{15} & c_{16}\\ c_{12} & c_{22} & c_{23} & c_{24} & c_{25} & c_{26}\\ c_{13} & c_{23} & c_{33} & c_{34} & c_{35} & c_{36}\\ c_{14} & c_{24} & c_{34} & c_{44} & c_{45} & c_{46}\\ c_{15} & c_{25} & c_{35} & c_{45} & c_{55} & c_{56}\\ c_{16} & c_{26} & c_{36} & c_{46} & c_{56} & c_{66}\end{pmatrix}\begin{pmatrix}\varepsilon_1\\ \varepsilon_2\\ \varepsilon_3\\ \varepsilon_4\\ \varepsilon_5\\ \varepsilon_6\end{pmatrix} \qquad (2.2)$$

2.1.2 Theoretical basis of RUS

As illustrated in Figure 2.1 **(Leisure, 1997)**, the mechanical resonant response of a three-dimensional solid is rather complicated. The key to the successful application of RUS is the ability to compute mechanical resonances from a body's shape, density and elastic moduli **(Migliori, 1993)**. For solids such as a sphere or rectangular parallelepiped (RP) that have a shape sufficiently simple to enable description by a few mathematical functions, the computing procedure involves seeking stationary points of the Lagrangian for a solid with free surfaces. Once the mechanical resonances are computed (the direct problem), a carefully constructed fitting procedure can be used to work backwards and find the elastic moduli from the measured resonant frequencies (the inverse problem).

The procedure for solving the direct problem begins with the general form of the Lagrangian L **(Migliori, 1997)**:

$$L = \int_V (KE - PE)dV \qquad (2.3)$$

where *KE* is the kinetic energy and *PE* is the potential energy. For an arbitrarily shaped elastic solid with volume *V* in a free surface *S* and with density ρ, the kinetic energy is given by:

$$KE = \frac{1}{2}\sum_i \rho\omega^2 u_i^2 \qquad (2.4)$$

The potential energy is given by:

$$PE = \frac{1}{2}\sum_{i,j,k,l} C_{ijkl}\frac{\partial u_i}{\partial x_j}\frac{\partial u_k}{\partial x_l} \qquad (2.5)$$

Here u_i is the *ith* component of the displacement vector, ω is the angular frequency from harmonic time dependence, C_{ijkl} is a component of the elastic tensor. Subscripts i, j, etc., refer to Cartesian coordinate directions and the summation on subscripts runs from 1 to 3.

To find the minimum of the Lagrangian, we let *u* vary arbitrarily in *V* and on *S* and calculate the variation in L (δL). This yields:

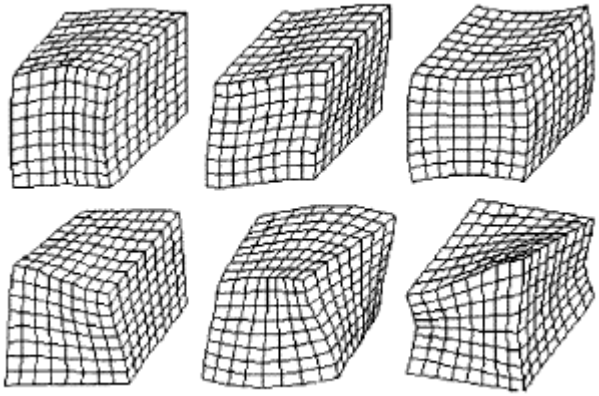

Figure 2.1 Illustration of several vibrational eigenmodes for a rectangular parallelepiped **(Leisure, 1997)**

$$\delta L = \int_V \left\{ \sum_i \left[\rho\omega^2 u_i + \sum_{j,k,l} C_{ijkl} \frac{\partial^2 u_k}{\partial x_j \partial x_l} \right] \delta u_i \right\} dV - \int_S \left\{ \sum_i \left[\sum_{j,k,l} \vec{n}_j C_{ijkl} \frac{\partial u_k}{\partial x_l} \right] \delta u_i \right\} dS \qquad (2.6)$$

Because δu_i is arbitrary in V and on S, the value of u_i that corresponds to stationary points of L (i. e. $\delta L = 0$) must satisfy the condition that the terms in square brackets in Equation 2.6 are zero. Setting the first such term in Equation (2.6) equal to zero yields the elastic wave equation:

$$\rho\omega^2 u_i + \sum_{j,k,l} C_{ijkl} \frac{\partial^2 u_k}{\partial x_j \partial x_l} = 0 \qquad (2.7)$$

The second square-bracketed term is an expression of free-surface boundary conditions:

$$\sum_{j,k,l} \vec{n}_j C_{ijkl} \frac{\partial u_k}{\partial x_l} = \sum_j \vec{n}_j \sigma_{ij} = 0 \qquad (2.8)$$

where σ_{ij} is the *ij* th component of the stress tensor.

There are no such u_i's of course, unless ω^2 is one of a discrete set of eigenvalues, the normal mode frequencies of free vibration of the system. This simple result makes possible the following procedure for obtaining the free vibrations of an object.

Using the Rayleigh-Ritz prescription, we expand the displacement vector in a

complete set of functions $\{\Phi_\lambda\}$:

$$u_i = \sum_\lambda a_{i\lambda}\Phi_\lambda \qquad (2.9)$$

and choose powers of Cartesian coordinates as our basis functions:

$$\Phi_\lambda = x^l y^m z^n \qquad (2.10)$$

where $\lambda = (l,m,n)$ is the function label, a set of three nonnegative integers. After substituting Equation (2.9) into Equation (2.3), we obtain:

$$L = \frac{1}{2}\omega^2 \vec{a}^T \overleftrightarrow{E}\vec{a} - \frac{1}{2}\vec{a}^T \overleftrightarrow{\Gamma}\vec{a} \qquad (2.11)$$

Here a is a vector with elements a_i whose transpose is a^T. E and Γ are matrices whose order R is determined by the truncation condition:

$$l + m + n \le N \qquad (2.12)$$

with R=3(N+1)(N+2)(N+3)/6. It was found that N = 10 gives a good compromise between computational accuracy, computing time and typical sample preparation errors.

The matrix E has elements:

$$E_{\lambda i\lambda' i'} = \delta_{ii'}\int_V \Phi_\lambda \rho \Phi_{\lambda'} dV \qquad (2.13)$$

and the matrix Γ has elements:

$$\Gamma_{\lambda i\lambda' i'} = \sum_{j,j'} C_{ijj'j'}\int_V \frac{\partial\Phi_\lambda}{\partial x_j}\frac{\partial\Phi_{\lambda'}}{\partial x_{j'}} dV \qquad (2.14)$$

The Equation (2.11) for the Lagrangian is stationary if the displacements u_i are solutions of the free-vibration problem. These solutions may be obtained by setting the derivatives of Equation (2.11) with respect to each of the R amplitudes $a_{i\lambda}$ equal to zero. This yields the following eigenvalue equation:

$$\omega^2 \overleftrightarrow{E}\vec{a} = \overleftrightarrow{\Gamma}\vec{a} \qquad . \qquad (2.15)$$

The matrix E is symmetric and positive definite and Γ is symmetric, so a standard eigenvalue-eigenvector subroutine package can be used to solve Equation (2.15) to obtain the eigenvalues ω^2.

This very fast and accurate solution to the direct problem is the key tool for the solution of the inverse problem. However, the inverse problem is not as straightforward. Since there is no unique solution to the inverse problem, a nonlinear optimization procedure is required. The code is based on a Levenberg-Marquard minimization and carries out a nonlinear least-square fit by minimizing the 'figure of merit' F defined by:

$$F = \sum_{i=1}^{N} w_i (f_i - g_i)^2 \qquad (2.16)$$

Here, $f_i = \omega_i/2\pi$ is the ith calculated frequency and g_i is the ith measured frequency. w_i is a weighing factor chosen based on the confidence in the measured frequencies and is customarily set to one or zero. Since many of the lower modes depend mostly on a shear mode, N must be large enough so that many non-shear modes are included. Figure 2.2 shows the block diagram for the RUS principle.

In a RUS measurement, the resonance frequencies of a sample are excited and detected by electronics shown in Figure 2.3. Then a fitting procedure follows, generating a list of calculated resonances based on the given sample dimensions and an educated guess of the elastic moduli. Using an iteration procedure that adjusts the input values of the elastic constants, the experimental frequencies are "matched" to the theoretical spectrum. The quality of a fit that is found is determined by the root-mean-square error σ_{RMS} between the calculated and experimental frequencies:

$$\sigma_{RMS} = 100 \times \sqrt{\frac{1}{N} \sum_{i=1}^{N} \left(\frac{g_i - f_i}{f_i} \right)^2} \,\% \qquad (2.17)$$

The computer repeats the fitting procedure until σ_{RMS} is minimized. If σ_{RMS} is not too high (typically below 0.5%), one can assume that the elastic constants generated by the computer accurately represent those of the sample.

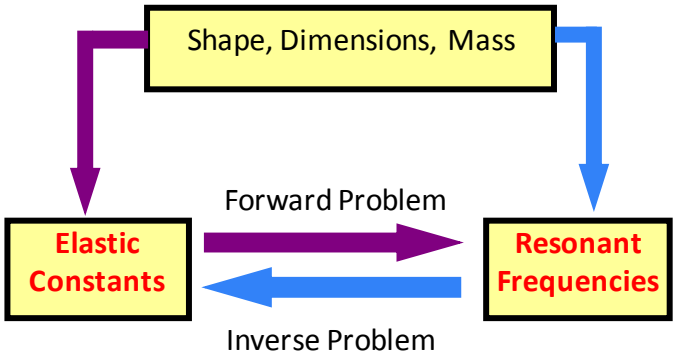

Figure 2.2 Principle of RUS

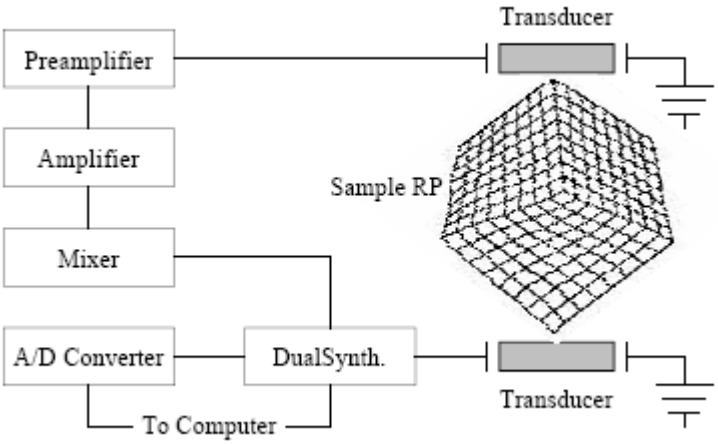

Figure 2.3 Block diagram of RUS electronics

2.1.3 RUS setup and data analysis

Because the task is to excite resonances, it is important to drive the sample at a low-symmetry location to excite as many modes as possible. The lowest symmetry point on a RP sample is the corner, thus this is a desirable point to drive and detect **(Migliori, 1993)**. Moreover, the corners have low mechanical impedance so that touching them with a transducer has minimal effect on the free-body condition. In earlier work, great pains were therefore taken to mount the sample on two of its opposite corners between two transducers, as illustrated in Figure 2.4. However, this approach has serious drawbacks. A sample mounted on its corner is easily knocked from between the transducers when the RUS probe is inserted into a cryostat. In addition, the sharp corners wear away both samples and transducers in long runs **(Migliori, 2005)**. The current trend avoids these problems by mounting the sample flat, as shown in Figure 2.5. This is also the setup in our RUS measurement. In this approach, the transducers are slightly nonparallel, so weak point contact is always achieved even though the sample is flat mounted.

In a RUS measurement, the sample is excited by one transducer, with a typical frequency range from 200 ~ 2000 KHz. A large response is detected by the other transducer when the frequency of the driving transducer corresponds to one of the sample's natural frequencies. A segment of a typical spectrum is shown in Figure 2.6. Peaks in the spectrum are marked and the fitting procedure discussed before is used to obtain the elastic constants. To obtain the temperature dependence of elastic constants or resonant frequencies, a set of RUS transducers is mounted in a Physical Property Measurement System (PPMS). With the help of a LabVIEW program, automatic measurement of resonant frequencies at different temperatures is realized.

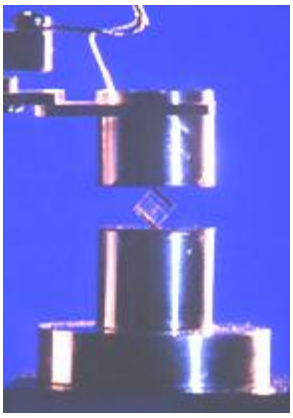

Figure 2.4 RP sample corner-mounted in RUS setup

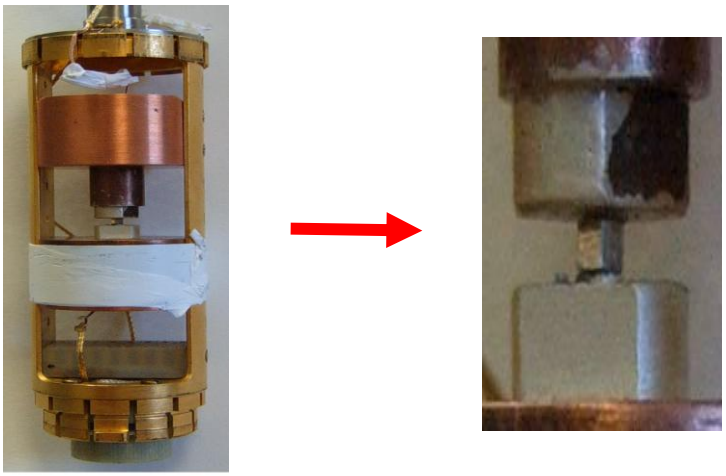

(a) (b)

Figure 2.5 (a) RP sample flat-mounted in RUS setup; (b) Enlarged image of mounted sample

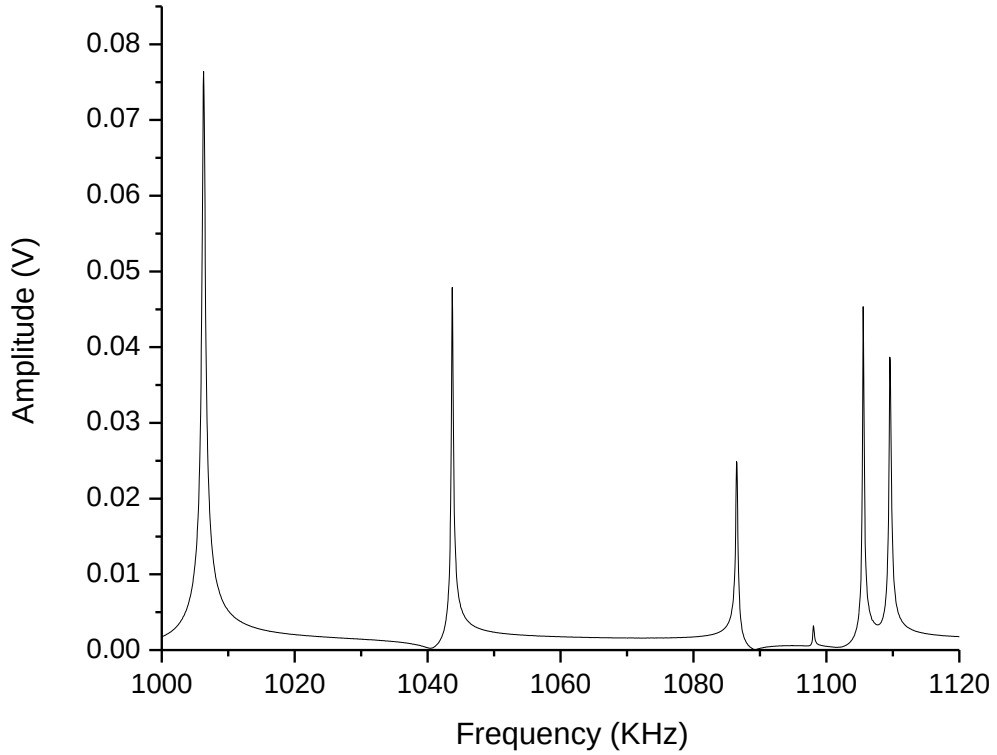

Figure 2.6 Typical resonance frequency spectrum measured by RUS

2.1.4 RUS and phase transitions

The measurement of elastic moduli is useful not only in the determination of their absolute magnitude but also in the study of their relative temperature dependence, especially in the presence of phase transitions. RUS has proved to be an ideal probe for the study of phase transitions. Sample inhomogeneities are less of a problem because of RUS's ability to use much smaller samples. Its ability to simultaneously determine all elastic moduli in one run can eliminate the worry that difference in moduli are due to extrinsic variations from run to run, as one would encounter in pulse-echo measurement. Its absence of a bond between the sample and transducers makes it possible to make measurements on systems that undergo considerable thermal contraction at the transition temperature.

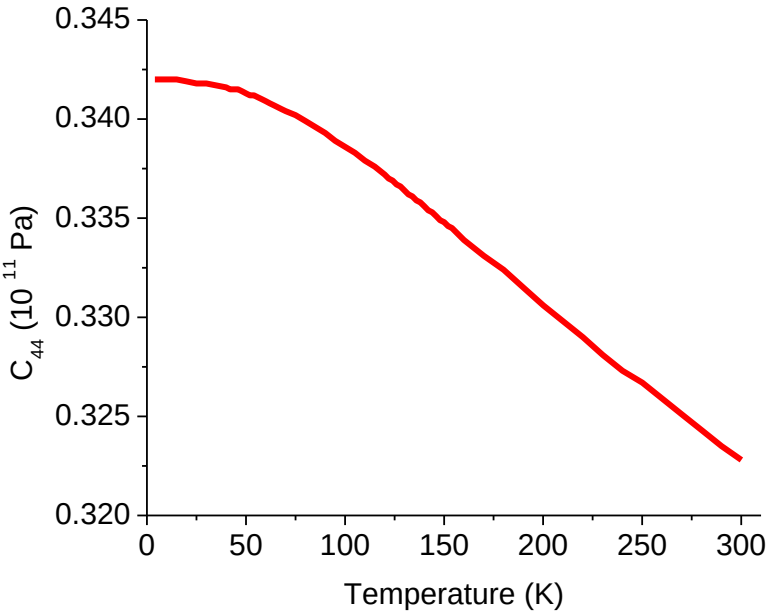

Figure 2.7 “Normal” temperature dependence of elastic constants

Figure 2.7 shows the “normal” temperature dependence of elastic constants, i.e., a smooth increase with decreasing temperature, leveling–off at the lowest temperatures. However, elastic constants will deviate from “normal” behavior when a phase transition occurs. The most common phase transitions studied by RUS are second-order transitions. At such phase transitions, many thermodynamic quantities show no obvious evidence of the transition. However, as the second derivatives of free energy with respect to strain, the elastic moduli may show discontinuities at second-order transitions. As a tensor, the elastic moduli can probe the full symmetry of the discontinuities and one may use the discontinuities to learn about the physics driving the phase transition.

A particularly noteworthy application of RUS to such a transition was realized by Migliori and collaborators, who have successfully used RUS to study the structural phase transition in single crystal perovskite $SrTiO_3$ **(Migliori, 1993)**. $SrTiO_3$ undergoes a structural phase transition at 105 K from cubic to tetragonal

symmetry. A Ginsburg-Landau analysis of this phase transition predicts a step-like decrease in elastic moduli at the transition and predicts the relative size of the step for each individual modulus by using the full crystal symmetry. RUS measurements on $SrTiO_3$ by Migliori et al. show that each modulus increases with decreasing temperature due to normal thermal contraction and then exhibits a sharp decrease in the region near the transition, in excellent agreement with the theoretical prediction. Another important example of RUS is its application to the study of the phase transition in superconducting $La_{1.86}Sr_{0.14}CuO_4$ **(Sarrao, 1994b)**. Sarrao's RUS measurements revealed a strong temperature dependence of the tetragonal elastic constants above the tetragonal-to-orthorhombic structural phase transition in $La_{1.86}Sr_{0.14}CuO_4$, and thus raised serious questions about the standard interpretation of the nature of this second-order structural transition in $La_{2-x}Sr_xCuO_4$.

For samples with irregular shape or symmetry lower than orthorhombic, the procedure for calculating the elastic moduli from the resonances becomes quite cumbersome, but a great deal of physics near phase transitions may still be studied by high-precision measurement of resonant frequencies or quality factors (which will be introduced below) as a function of temperature, pressure and isotopic content, without having to determine the absolute values of the elastic constants.

2.1.5 Quality factor in RUS

The ability to measure the quality factor Q of a mechanical resonance is another attractive feature of RUS. Q is defined as the center frequency of the resonance divided by its full width at half maximum (FWHM), as indicated in the following equation:

$$Q = \frac{f}{\Delta f(FWHM)} \tag{2.18}$$

As can be seen in the equation, the sharper the resonance peak, the higher Q. Figure 2.8 demonstrates a resonance peak with Q as high as 10^5 **(Migliori, 2008)**. The high Q values of many resonance lines surely enhance the sensitivity of RUS. However, to obtain high-Q resonances, special attention needs to be paid to the quality of RUS design and to the sample quality.

It is worth pointing out that only those processes that cause energy loss from the vibrational mode under consideration will affect the Q of that particular mode. Elastic scattering processes can change the location of the resonance, but have no effects on the Q of the resonance.

1/Q is sometimes called internal friction, since one can often obtain useful information about the ultrasonic attenuation from Q. In many cases, a sudden change in Q appears near phase transition, which can help define the transition temperature and can provide important insight into the nature of the transition.

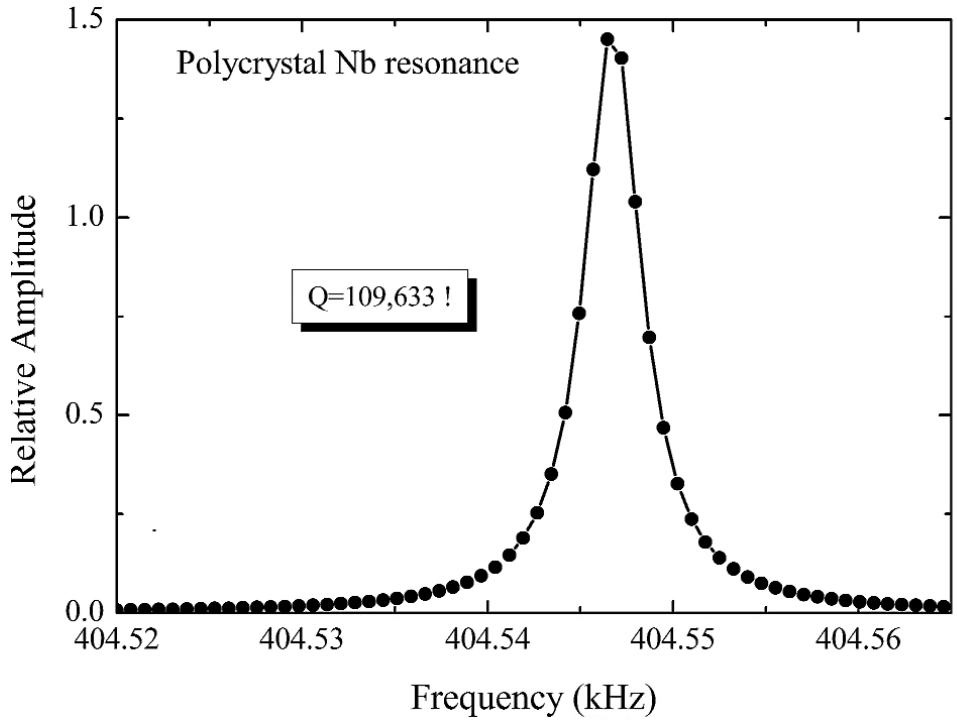

Figure 2.8 An example of a high-Q resonance acquired with RUS system **(Migliori, 2008)**

2.2 Sample preparation

As part of this research, we have grown single crystals of $Ca_{2-x}Sr_xRuO_4$, using facilities at Oak Ridge National Laboratory (ORNL). Single crystals of vanadium spinels and titanate pyrochlores were provided by Dr. Gaulin at Mcmaster University and Dr. Zhou at the National High Magnetic Field Laboratory. All the single crystals are grown in an optical floating zone furnace.

2.2.1 Floating zone technique

To study material properties in condensed matter, it is important to have high quality single crystals. Among the various techniques for single crystal growth, the optical floating zone method has been the subject of rapid development since the first use nearly fifty years ago. Following extensive development, in particular at SEC in Japan, image furnaces have become commercially available in the 1980s. The basic principle of this technique is melting a small section of a polycrystalline feed rod, by means of infrared radiation generated by two halogen or xenon light bulbs. Ellipsoidal or parabolic mirrors focus the infrared radiation onto the feed rod to produce a molten zone. Early designs of the image furnace had only one or two mirrors, but since the late 1990s, image furnaces usually have four mirrors to produce more uniform heating and to improve furnace power. The molten zone is then translated along the sample length by moving the sample with respect to the radiation focus. The crystal will grow on the solidifying end of the floating zone on a seed rod, which should be a material with a similar crystal structure as the feed rod. The crystal growth process always proceeds in vertical direction. In addition, a rotation movement of the two rods improves the microstructural homogeneity during directional solidification. As the molten zone is shielded by a quartz tube, one can choose the atmosphere and pressure under which the growth takes place. Fig. 2.9 and 2.10 respectively show the schematic of this technique and the image furnace used in our research.

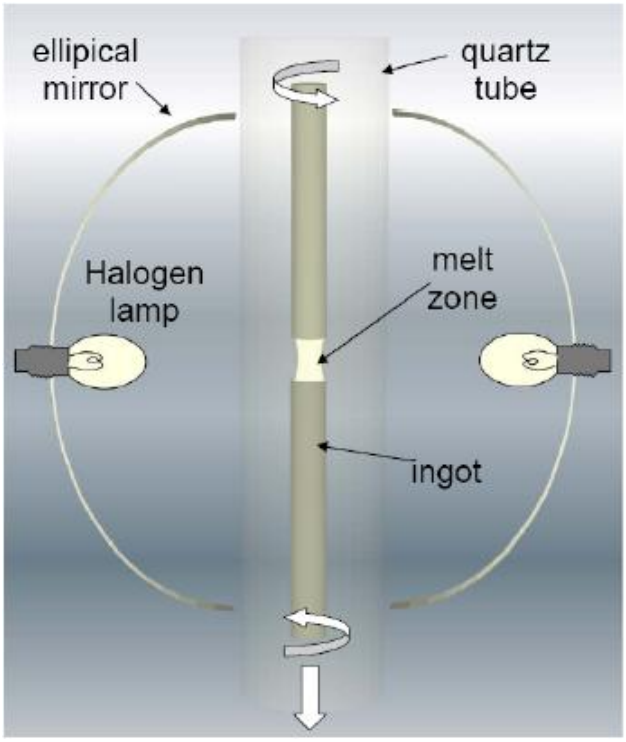

Figure 2.9 Schematic of floating zone technique

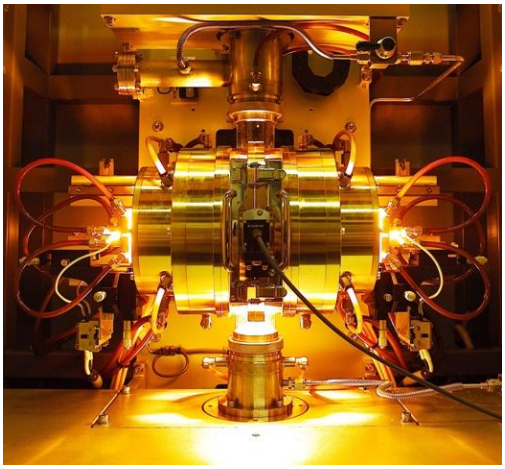

Figure 2.10 Image of floating zone furnace

When growing single crystals by floating zone technique, careful control of certain experimental parameters is of prime importance in order to optimize both the stability of the molten zone and the eventual crystal quality. Those parameters include feed rod characteristics, the growth rate and rotation rate, the temperature gradient along the sample, as well as the growth atmosphere and gas pressure, all of which can play key roles during single crystal growth. In particular, the quality of feed rod is extremely important since a poorly compacted feed rod can lead to bubble formation in the molten zone and in the growing crystal.

The floating zone technique has many advantages, as summarized below. (1) It is crucible-free so that there can be no contamination by a crucible material. (2) In contrast to crucible methods, a steady state can be achieved, which is especially beneficial for crystal growth of doped materials and for incongruent crystallization. (3) The speed of the crystallization may be well controlled, which allows the growth of materials with very complex metallurgical properties. (4) Oxides melting as high as 2500^{o}C can be grown. The growth can be conducted at high pressure (up to 10 atm) and in a specific atmosphere. However, the floating zone technique has some disadvantages as well. It is not suitable for materials that undergo a phase transition during cooling and for materials with high vapor pressure or high viscosity. In addition, the light heating used in this technique is not suitable for metallic samples that exhibit a high reflectivity in the infrared region.

Nowadays, the floating zone technique has become a preferred method for high-quality single crystal growth, especially for those showing extreme melt reactivity and high melting temperatures. In fact, it has become a standard method for single crystal growth in the semiconductor industry. The growing number of floating zone furnaces in use proves the usefulness of this method in the growth of a wide range of materials, from metals to semiconductors to various complex oxides including high-temperature superconductors, new magnetic materials and complex oxides with “exotic” oxidation states of some cations.

We have been successful in synthesizing polycrystals and in growing single crystals of $Ca_{2-x}Sr_xRuO_4$ in a wide region of x, by means of floating zone method. To prepare a polycrystalline rod, a standard solid-state reaction was used with $CaCO_3$ (99.9995% Alfa Aesar), $SrCO_3$ (99.9995% Alfa Aesar), and RuO_2 (99.99% Alfa Aesar) powders as starting materials. Those powders were mixed with appropriate molar ratio, depending on the composition of the polycrystal to be made. For example, the ratio was 1.8∶0.2∶1.15 for $Ca_{1.8}Sr_{0.2}RuO_4$ polycrystal. After the mixture was well ground in a vibratory micro mill for about an hour, a proper amount of the mixture was put in a rod-shaped rubber balloon. After being pressed in water under the pressure of 1200 kg/m^2, the rubber balloon was cut off by scissors. Then, the rod, with a typical diameter of 5 mm and a typical length of 120 mm, was sintered in a furnace at 950°C for 24 hours to yield a homogeneous polycrystal. This polycrystalline rod was used as the feed rod in the process of single crystal growth in the NEC SC-M15HD image furnace in Figure 3.2. During the growth process, both the feed rod and the seed rod rotated in the opposite direction with a rotation rate of 20 rpm. The single crystal was grown at the growth rate of 25 mm/h in the environment of oxygen and argon gases. The ratio of the two gases is 1:1 and the pressure of each gas is 0.3 MPa. During the growth process, the furnace temperature needs to be adjusted from time to time to ensure a stable molten zone. If the temperature is too high or too low, continuous single crystal growth may not be realized. Figure 2.11 shows the single crystal of Sr_2RuO_4 grown by floating zone technique.

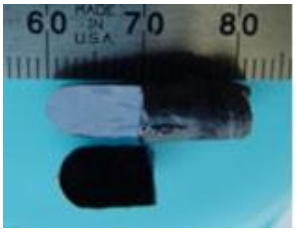

Figure 2.11 Single crystal of Sr_2RuO_4 grown by floating zone technique in ORNL

2.2.2 RUS sample preparation

To obtain the elastic moduli of a single crystal by RUS, the first step is to determine the orientation using X-ray Laue diffraction. The sample is then cut to the nearly final shape using a wire saw or wheel saw so that the faces of the sample are perpendicular to its crystallographic axes. Although it is possible to find the elastic moduli of a RP-shaped sample with crystallographic axes not parallel to its edges, this is difficult and prone to error. It is noted that a 1° error in alignment will produce an error in the final determination, which is of the order of a few parts in 10^4, an acceptable value. However, parallelism or perpendicularity errors couple linearly to some resonance modes but not others, requiring precision of the order 1 μm/mm.

To achieve such precision, it is usually necessary to polish the sample after cutting. Unlike the pulse-echo method, the entire sample must be carefully polished with sharp edges and corners. To achieve an accurate fit, the faces of the mm-sized RP sample must be accurate to 2 μm or better, which means that the geometric errors must be of the order of a part in 10^3 since the resonances are to be fit to that order.

Most samples in our research were polished by using ground steel shims and a magnet plate. The edges of the shims were squared up in an ordinary milling machine, and their surfaces were required to be 10 to 50 μm thinner than the distance between samples faces to be polished. The arrangement of four shims and the sample on a round magnet plate is shown in Figure 2.12. The X-ray oriented sample is trapped between the shims and polished using a variety of sand paper and polishing cloths. As the sample is close to completion, the shims support the sample edges to ensure that sharp edges and corners are produced. This appears to be important for an accurate fit. At least six sets of ground steel shims are required, corresponding to the two cuts required for three different edge lengths of the sample. For brittle samples like ruthenate $Ca_{2-x}Sr_xRuO_4$, the chipping of the edges can be a problem, which can be prevented by using Crystalbond or wax, an adhesive implemented by melting it on a hot plate.

It needs to be pointed out that it is preferred that a finished RP-shaped sample has three different dimensions instead of being a perfect cube. The reason is that the geometric symmetry of a cube will cause a degeneracy of resonant frequencies, which means that several modes have the same frequency. Such overlapping of resonances is undesired and in most cases it will cause difficulties when sorting out the total number of resonances and their locations, thus decreasing the possibility of obtaining reliable elastic moduli because the models will possibly not fit the measured data. Usually, a slight difference between dimensions will split the degeneracy and make it easy to spot the missing mode.

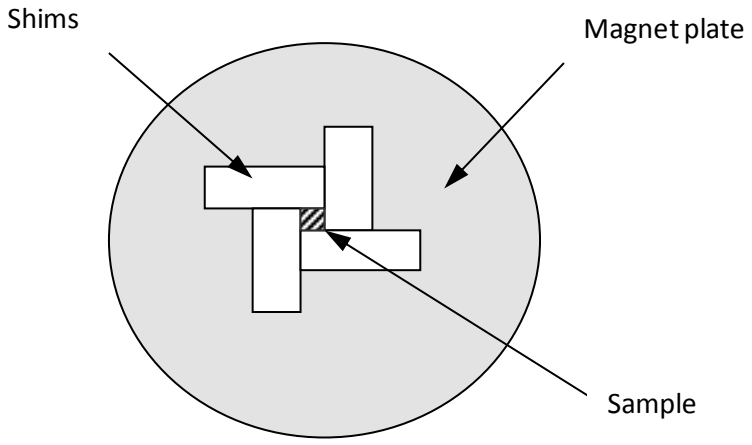

Figure 2.12 A polishing system using ground steel shims to make a RP sample

CHAPTER 3

RESONANT ULTRASOUND STUDIES OF $CA_{2-X}SR_XRUO_4$

In this chapter, we present the results of our study of the elastic response of doped ruthenates $Ca_{2-x}Sr_xRuO_4$ with $0.2 \leq x \leq 2$ **(Luan, 2009)**. The RUS data reported here were carried out as a function of temperature between 5 K and 300 K, using a custom designed RUS probe that was inserted in a commercial Quantum Design PPMS. For our study, three $Ca_{2-x}Sr_xRuO_4$ polycrystals with x = 1.0, 0.5 and 0.3 were cut and polished into rectangular parallelepipeds (RP) and their elastic constants were determined from measurements of the resonant frequencies. In addition, the temperature dependence of the resonant frequencies were measured on $Ca_{2-x}Sr_xRuO_4$ single crystals with five different compositions, *i.e.*, x = 2.0, 1.9, 0.5, 0.3 and 0.2. The shape and small size of these samples prevented crystallographic orientation, but valuable information can be obtained from the temperature dependence of the frequencies, as explained below. RUS measurements were carried out upon both cooling and warming, and no difference was observed. The results presented are based on the cooling data.

3.1 $Ca_{2-x}Sr_xRuO_4$ polycrystals

For polycrystals, only two independent elastic constants exist: the longitudinal modulus C_{11} and shear modulus C_{44}. In this research, elastic constants of three $Ca_{2-x}Sr_xRuO_4$ polycrystalline samples with x = 1, 0.5 and 0.3 were measured, using the RUS technique. The polycrystals were polished into RP-shape with parallel faces and sharp corners, and their mass and dimensions were measured. The resonant spectra were subsequently measured by RUS, and the resonant frequencies were marked, from which a text file called *rusin.dat* was generated. The *rusin.dat* file serves as the input to the fitting code and the output was written to a file called *rusout.dat*. Table 3.1 shows the output file for $CaSrRuO_4$ (x = 1) polycrystal.

Table 3.1 RUS output file for polycrystal $CaSrRuO_4$ (mass: 9 mg; density = 3.842 g/cm^3)

$CaSrRuO_4$_poly_07_9mg
free moduli are c11, c44
free dimensions are d1, d2, d3
using 10 order polynomials mass = 0.0090 gm rho = 3.842 gm/cc

n	fex	fr	%err	wt	k	i	df/d(moduli)	
1	0.745623	0.742767	-0.38	1.00	4	1	0.00	1.00
2	0.958129	0.960353	0.23	1.00	6	2	0.15	0.85
3	1.033520	1.037802	0.41	1.00	7	2	0.17	0.83
4	1.192600	1.194819	0.19	1.00	3	2	0.02	0.98
5	1.212610	1.222518	0.82	1.00	4	2	0.00	1.00
6	1.285140	1.282617	-0.20	1.00	5	1	0.07	0.93
7	1.325660	1.331594	0.45	1.00	2	2	0.02	0.98
8	1.354680	1.368326	1.01	0.00	8	2	0.08	0.92
9	1.379190	1.380100	0.07	1.00	6	3	0.30	0.70
10	1.407700	1.456065	3.44	0.00	1	2	0.11	0.89
11	1.496250	1.498298	0.14	1.00	5	2	0.09	0.91
12	1.509750	1.506108	-0.24	1.00	8	3	0.04	0.96
13	1.544270	1.543524	-0.05	1.00	2	3	0.16	0.84
14	1.621810	1.613565	-0.51	1.00	8	4	0.05	0.95
15	1.666330	1.661532	-0.29	1.00	5	3	0.08	0.92
16	1.793400	1.795972	0.14	1.00	7	3	0.08	0.92
17	1.862930	1.863633	0.04	1.00	1	3	0.02	0.98
18	1.876440	1.871709	-0.25	1.00	4	3	0.09	0.91
19	1.907450	1.896282	-0.59	1.00	3	3	0.11	0.89

Bulk Modulus= 0.598

c11	c22	c33	c23	c13	c12	c44	c55	c66
1.0077	1.0077	1.0077	0.3933	0.3933	0.3933	0.3072	0.3072	0.3072

d1	d2	d3
0.16761	0.13145	0.10634

loop# 2 rms error= 0.3570 %, changed by -.0000009 %
length of gradient vector= 0.000006 blamb= 0.000000

eigenvalues	eigenvectors				
0.04007	1.00	-0.02	-0.01	0.00	0.00
14.99146	-0.02	-0.96	-0.24	-0.03	0.10
545.83885	0.00	0.18	-0.86	0.40	-0.25
1574.31778	0.00	0.15	-0.42	-0.88	0.14
2800.65445	0.00	0.12	-0.14	0.24	0.95

chisquare increased 2% by the following % changes in independent parameters

1.46	-0.08	-0.02	0.01	-0.08
0.00	-0.24	0.16	0.18	0.18
0.00	-0.01	-0.13	-0.08	-0.03

The header of the *rusout.dat* file in Table 3.1 contains four lines. The first line is simply a comment on what material is being worked on. The second and the third lines respectively list the moduli (to be fit) and the dimensions (known). The fourth line shows the order of polynomials to be used (usually 10), together with the mass and density of the sample under investigation.

Following the header of the *rusout.dat* file is the list of modes used in the fitting procedure. In the list, the columns from left to right are the mode number *n*; the measured frequency *fex*, the fitted frequency *fr*, the error in fitting that mode *%err*, the weight used for fitting *wt* (1 or 0), the mode symmetry and order *k and i*, and the dependence of the mode on moduli to be fit (in this case, C_{11} and C_{44}) *df/d(moduli)*. For example, for the first mode (n = 1), the two numbers under *df/d(moduli)*, 0.00 and 1.00, are the sensitivities of the first fitted mode *fr* to the elastic moduli C_{11} and C_{44} respectively. This provides us a useful piece of information that the first mode depends only on shear modulus C_{44}. Of course, it is crucial to obtain a reliable fit in order to identify the mode type and its dependence on the moduli.

Further down in the output are fitted elastic moduli, dimensions, the number of iterations required for convergence, the RMS error between the fitted and measured frequencies, and the change in that error between present and previous iteration. It needs to be pointed out that C_{12} here is not an independent elastic modulus and it is related to C_{11} and C_{44} by the relation $C_{12} = C_{11} - 2C_{44}$, a relation that is only valid in elastically isotropic materials. In single crystals, C_{12} is an independent elastic modulus. The RMS error is 0.3570 %, which indicates a reliable fit. Below the moduli are the eigenvalues and vectors for references and debugging if the code crashes, and finally the all-important error matrix. The biggest entry in the first column is the approximate error bar for C_{11}. The biggest entry in the second column is the error bar for C_{44} and the third, fourth and fifth column are for d1, d2 and d3. The shear modulus always seems to fit better and have tighter error bars, because most of the lower modes are shear-like.

Table 3.2 lists the experimental values for the elastic moduli obtained at room temperature using RUS for $Ca_{2-x}Sr_xRuO_4$ polycrystals with x = 1.0, 0.5 and 0.3. Also listed in Table 3.2 are the calculated polycrystalline moduli for the parent compound Sr_2RuO_4 (x = 2), using the Voigt approximation **(Schreiber, 1973)**. The latter allows computation of the shear and bulk modulus of a polycrystalline solid based on the values of elastic moduli of the single crystal, under the assumption that the stress is uniform everywhere within the sample.

The general expressions for the Voigt approximation are:

Bulk modulus:

$$B = \frac{1}{9}(c_{11} + c_{22} + c_{33}) + \frac{2}{9}(c_{12} + c_{23} + c_{13}) \qquad (3.1)$$

Shear modulus:

$$G = \frac{1}{15}(c_{11} + c_{22} + c_{33}) - \frac{1}{15}(c_{12} + c_{23} + c_{13}) + \frac{1}{5}(c_{44} + c_{55} + c_{66}) \qquad (3.2)$$

The C_{11} and C_{44} values of Sr_2RuO_4 polycrystal are calculated from the data reported in reference **(Paglione, 2002)**. With tetragonal structure, single crystal Sr_2RuO_4 has six independent elastic constants C_{11} (= C_{22}), C_{33}, C_{12}, C_{13} (= C_{23}), C_{44} (=C_{55}) and C_{66}, and the reported values are C_{11} = 2.32, C_{33} = 2.08, C_{23} = 0.71, C_{12} = 1.06, C_{44} = 0.657, C_{66} = 0.612 (unit: 10^{11} Pa) **(Paglione, 2002)**. We put those values into equations (3.1) and (3.2) and obtained B = 1.2978 10^{11}Pa, G = 0.6679 10^{11}Pa.

For isotropic polycrystal, the following relations hold:

$$C_{44} = G \qquad (3.3)$$

$$C_{11} = B + \frac{4G}{3} \qquad (3.4)$$

yielding C_{44} = 0.6679 10^{11}Pa and C_{11} = 2.1883 10^{11}Pa.

Before comparing the elastic moduli found for the various compositions, we need to point out that the density of the polycrystals is only about 70% of the theoretical density. As the elastic moduli of a solid depend on its density, a meaningful comparison of the experimental values requires that they are corrected to zero porosity. Following the model of Ledbetter and Datta **(Ledbetter, 1986)** for spherical inclusions in a matrix and Chandra Sekhar's treatment of a porous ceramic as a composite material containing spherical voids **(Sekhar, 2003),** the moduli for zero porosity $Ca_{2-x}Sr_xRuO_4$ polycrystals are estimated, and included in Table 3.2. Figure 3.1 illustrates how the values of the elastic constants decrease with decreasing Sr-content. Since Ca atoms are smaller than Sr atoms, the replacement of Sr by Ca atoms in Sr_2RuO_4 will cause both randomness in SrO layers and lattice distortion in RuO_2 layers, and thus induce a decrease of elastic constants.

Table 3.2 Elastic constants of $Ca_{2-x}Sr_xRuO_4$ polycrystals at room temperature. The calculated values are corrected for porosity, as explained in the text.

Composition	C_{11} (10^{11} Pa)		C_{44} (10^{11} Pa)	
	experimental	corrected	experimental	corrected
Sr_2RuO_4	2.1883 [a]		0.6679 [a]	
$CaSrRuO_4$	1.008	1.946	0.307	0.534
$Ca_{1.5}Sr_{0.5}RuO_4$	0.459	0.905	0.176	0.350
$Ca_{1.7}Sr_{0.3}RuO_4$	0.364	0.722	0.155	0.320

[a] Calculated by using single crystal values in reference **(Paglione, 2002)**

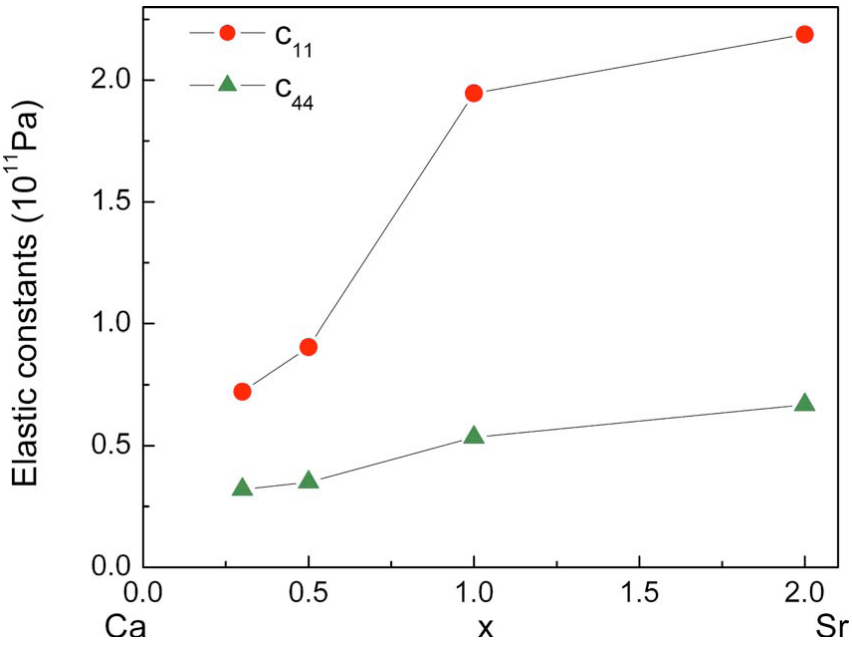

Figure 3.1 Elastic constants (corrected for porosity) versus composition x in $Ca_{2-x}Sr_xRuO_4$ polycrystals. The error for C_{11} is less than 1.5 % and less than 0.3 % for C_{44}.

3.2 $Ca_{2-x}Sr_xRuO_4$ single crystals

The resonant frequencies of five $Ca_{2-x}Sr_xRuO_4$ single crystals (x = 2.0, 1.9, 0.5, 0.3 and 0.2) were measured between 5 K and 300 K (the x = 0.2 composition was measured up to 350 K). The squared resonant frequencies are directly proportional to the elastic moduli **(Migliori, 1993) (Migliori, 1997)** and any irregularity in the elastic response is therefore reflected in the temperature dependence of the resonant frequencies.

The temperature dependence of representative squared resonant frequencies for the 5 single crystals is plotted in Figures 3.2 and 3.3. A significant softening is apparent in the behavior of all 5 crystals, but whereas this softening is rather gradual and spans more than 100 K in the compounds with $x > 0.5$, it is more abrupt in the samples with high Ca-content ($x \leq 0.5$).

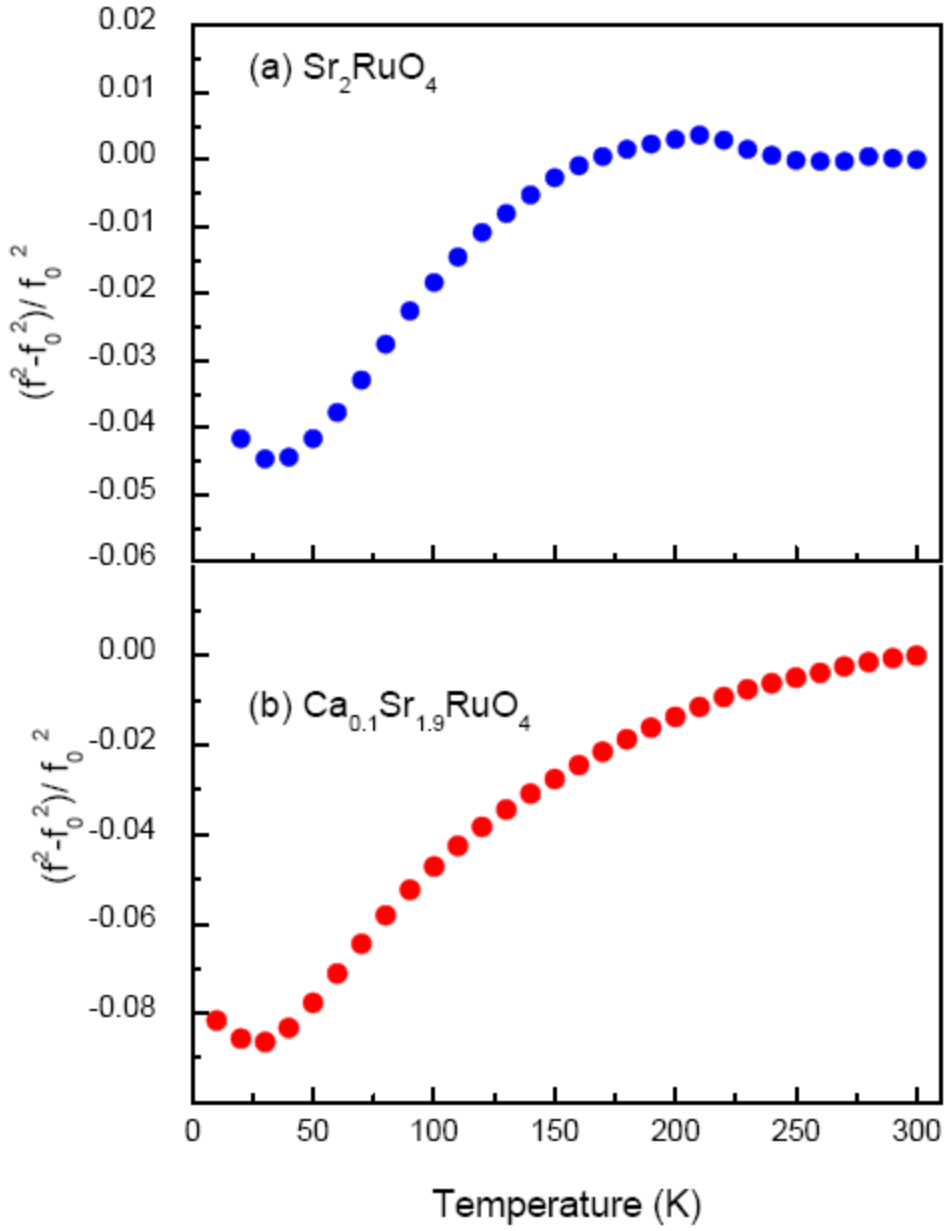

Figure 3.2 Relative change in representative squared resonant frequencies vs. temperature for Sr_2RuO_4 (a), and $Ca_{0.1}Sr_{1.9}RuO_4$ (b)

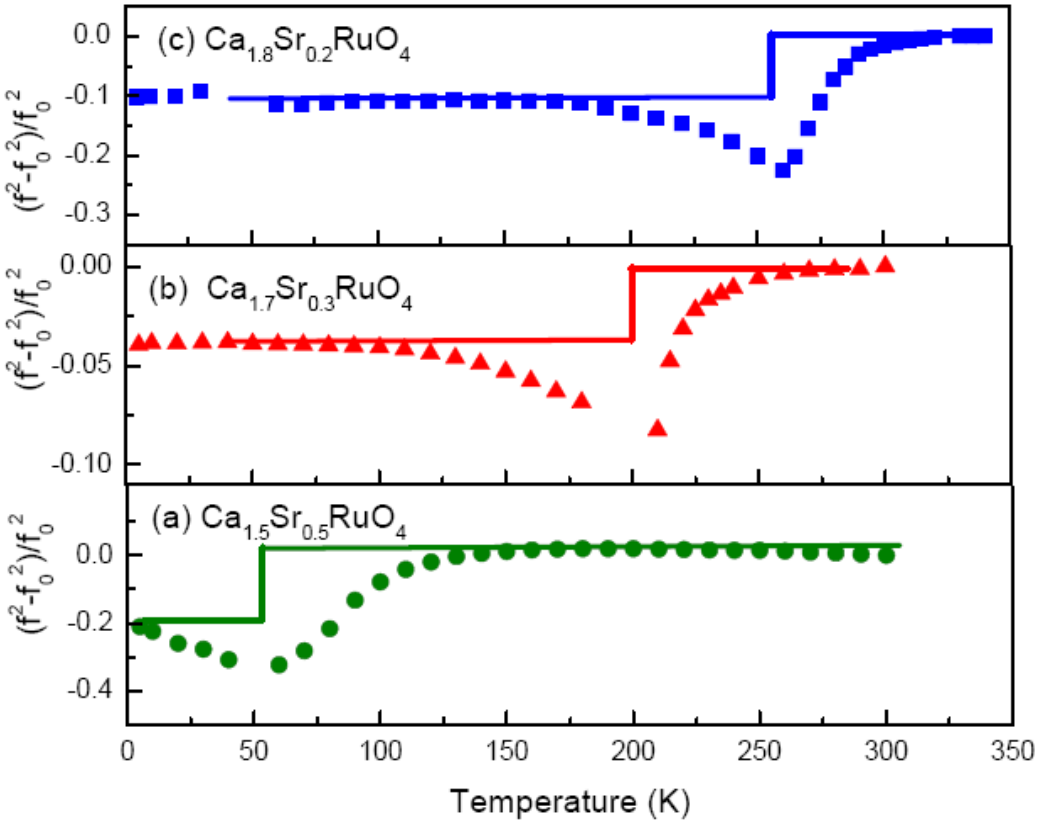

Figure 3.3 Relative change in representative squared resonant frequencies vs. temperature for $Ca_{1.5}Sr_{0.5}RuO_4$ (a), $Ca_{1.7}Sr_{0.3}RuO_4$ (b), and $Ca_{1.8}Sr_{0.2}RuO_4$ (c)

Starting with the parent compound, Sr_2RuO_4, a gradual softening of about 5% is observed upon cooling, reaching a minimum around 40 K, as shown in Figure 3.2a. While it may be tempting to attribute this softening to the superconductivity in this material, the two are most likely unrelated, since a similar -albeit more significant- softening is observed in the slightly Ca-doped (and non-superconducting) $Ca_{0.1}Sr_{1.9}RuO_4$ (Figure 3.2b). In contrast to La_2CuO_4, where tilting of the Cu-O octahedra leads to a tetragonal-to-orthorhombic phase transition, neutron diffraction on single crystals of Sr_2RuO_4 confirms that its K_2NiF_4-type structure remains undistorted **(Braden, 1997)**. Thus the observed softening of resonant frequencies in Sr_2RuO_4 upon cooling cannot be attributed to a structural transition. Instead, we believe that the softening is due to a rotational instability of RuO_6 octahedra around the c-axis. Even though neither tilting nor rotation of RuO_6 is revealed in Sr_2RuO_4, large atomic displacement parameters (ADP) **(Braden, 1997)** indicate that Sr_2RuO_4 is close to a rotational instability. Such instability has indeed been observed in the phonon dispersion relation of Sr_2RuO_4, using inelastic neutron scattering **(Braden, 1998)**. The rotation of the RuO_6 octahedra corresponds to a Σ_3 mode, whose second optical branch along [110] direction is found to soften continuously in the Brillouin zone. This softening interacts with the first optical branch and the acoustic branch of Σ_3, leading to a sharp drop in the acoustic branch near the zone boundary **(Braden, 1998)**. This steep drop in the dispersion relation of the Σ_3 mode is an indication of a rotational instability, which we believe to be the cause of the observed softening of the resonant frequencies in Sr_2RuO_4 and $Ca_{0.1}Sr_{1.9}RuO_4$ upon cooling. With increasing Ca-concentrations, the instability develops into a static rotation of RuO_6 that distorts the *I4/mmm* symmetry and results in $I4_1/acd$ symmetry when the Sr-content decreases below x = 1.5 **(Friedt, 2001)**.

Plotted in Figure 3.3a is the temperature dependence of a representative squared resonant frequency for $Ca_{1.5}Sr_{0.5}RuO_4$ (x = 0.5). The softening in this sample is more pronounced, and happens in a narrower temperature region than the softening

observed in Sr_2RuO_4 and $Ca_{0.1}Sr_{1.9}RuO_4$. This indicates that a different mechanism is most likely responsible for the sudden drop in resonant frequency, observed below 150 K in $Ca_{1.5}Sr_{0.5}RuO_4$. $Ca_{1.5}Sr_{0.5}RuO_4$ is known to be at the verge of a structural phase transition, from the tetragonal $I4_1/acd$ symmetry to orthorhombic *Pbca* symmetry. As the Ca-content increases, a tilt of RuO_6 octahedra develops in addition to the already present rotation. This tilt around an axis parallel to the *ab* plane deepens the lattice distortion and leads to the structural phase transition in the Ca-rich compounds ($x < 0.5$). Figure 3.4 illustrates the RuO_6 octahedron in different tilt and rotational configurations.

For $x = 0.5$, the transition is believed to have quantum-critical character **(Nakatsuji, 2000b)**. A quantum-critical phase transition takes place at the absolute zero of temperature, where crossing the phase boundary means that the quantum ground state of the system changes in some fundamental way **(Sondhi, 1997)**. As shown in the phase diagram (Figure 3.5), the temperature of the transition increases rapidly with increasing Ca-content. Figure 3.3 a-c illustrates how the gradual softening below 100 K, indicating the proximity of a phase-transition in $Ca_{1.5}Sr_{0.5}RuO_4$, develops into a sharp decrease in a very narrow temperature range in $Ca_{1.7}Sr_{0.3}RuO_4$ ($x = 0.3$) and $Ca_{1.8}Sr_{0.2}RuO_4$ ($x = 0.2$). The minimum in the resonant frequencies corresponds to a transition temperature T_o of 50 K for $Ca_{1.5}Sr_{0.5}RuO_4$, 210 K for $Ca_{1.7}Sr_{0.3}RuO_4$ and 260 K for $Ca_{1.8}Sr_{0.2}RuO_4$ respectively. Note that $T_o > 0$ K for $Ca_{1.5}Sr_{0.5}RuO_4$, indicating that the actual Ca content in our sample is slightly greater than 1.5. Nevertheless, these transition temperatures agree well with the phase diagram of $Ca_{2-x}Sr_xRuO_4$, and illustrate how RUS measurements probe structural phase transitions. In addition to the softening, a significant broadening of the resonance peaks is observed in the vicinity of the transition, indicating considerable ultrasonic attenuation.

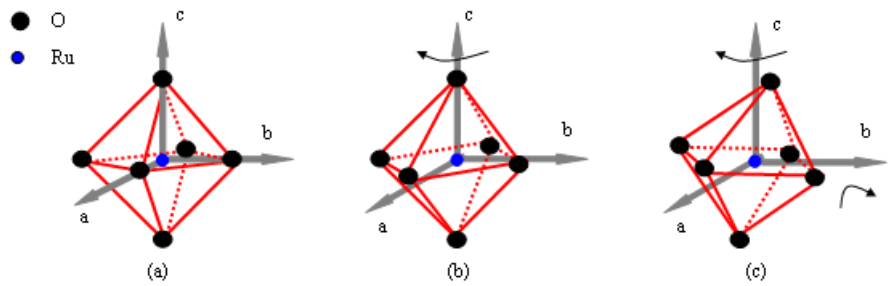

Figure 3.4 The RuO_6 octahedron in different tilt and rotational distorted configurations: (a) no distortion, (b) rotation around c axis, (c) combined tilt and rotational distortion

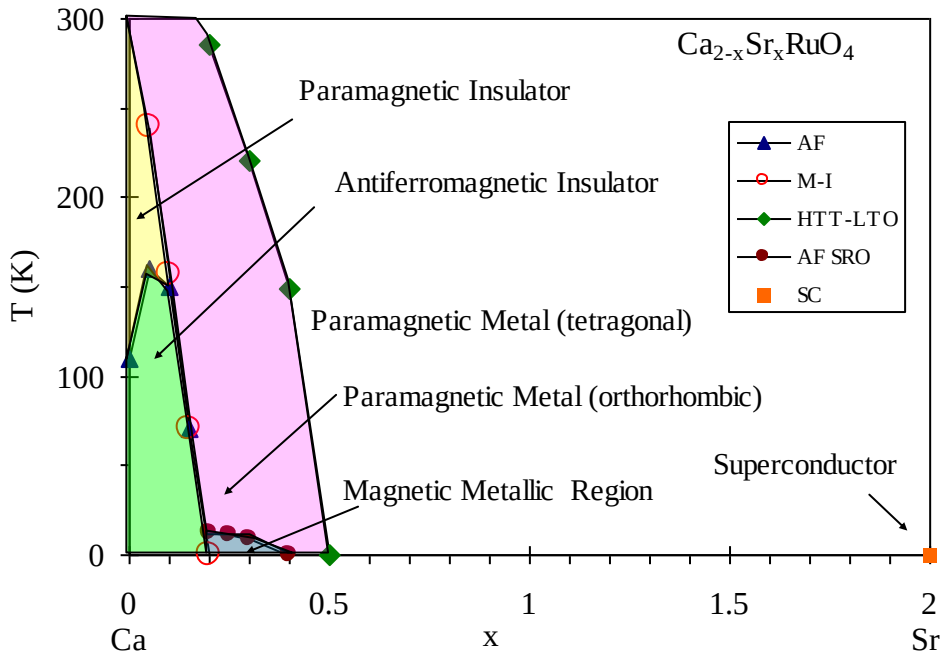

Figure 3.5 Phase diagram of $Ca_{2-x}Sr_xRuO_4$ series, based on data from reference (Nakatsuji, 2000b)

The sharp softening of resonant frequencies across the structural transition is due to the coupling between the elastic strain and the order parameter, i.e. the tilt angle of the RuO_6 octahedra. The Landau theory of structural phase transitions predicts a step-like decrease in the elastic moduli when approaching Tc from high temperatures, as observed in $Ca_{1.7}Sr_{0.3}RuO_4$ and $Ca_{1.8}Sr_{0.2}RuO_4$, when the coupling is linear in strain and quadratic in order parameter **(Rehwald, 1973)**. The deviation from true step-like behavior can be attributed to the thermal fluctuation or some imperfections in the crystals. A similar behavior of the resonant frequencies was also revealed across the tetragonal-to-orthorhombic transition in the cuprates $La_{2-x}Sr_xCuO_4$ **(Sarrao, 1994 b)** and in the pyrochlore $Cd_2Re_2O_7$ **(Sergienko, 2004)**.

Whereas the above results clearly illustrate the ability of RUS to qualitatively probe instabilities and phase transitions in a crystal lattice, a full quantitative analysis requires measurements on oriented single crystals. Since the resonant frequencies represent a "mixture" of the elastic moduli, i.e., a given frequency typically depends on a combination of elastic constants, it is not possible to evaluate the temperature dependence of individual moduli at this time. When slightly larger single crystals that can be oriented are available, a quantitative study of the elastic response of these crystals should be able to assess the individual moduli.

3.3 Conclusions

In summary, we report the elastic constants c_{11} and c_{44} for three $Ca_{2-x}Sr_xRuO_4$ polycrystals (x = 1.0, 0.5 and 0.3). It is found that the replacement of Sr by smaller Ca atoms causes a decrease of elastic constants. The temperature dependences of the resonant frequencies for five $Ca_{2-x}Sr_xRuO_4$ single crystals (x = 2.0, 1.9, 0.5, 0.3 and 0.2) all show softening, due to rotation and/or tilts of the Ru-O octahedra, and clearly illustrate the ability of RUS to qualitatively probe instabilities and phase transitions in a crystal lattice. The gradual softening of resonant frequencies over a large

temperature span in single crystals Sr_2RuO_4 (x = 2) and $Ca_{0.1}Sr_{1.9}RuO_4$ (x = 1.9) is caused by a rotational instability in the lattice. The sharp softening of resonant frequencies over a very narrow temperature range for $Ca_{1.7}Sr_{0.3}RuO_4$ (x = 0.3) and $Ca_{1.8}Sr_{0.2}RuO_4$ (x = 0.2) corresponds to the tetragonal to orthorhombic structural phase transition, which involves both rotation and tilting of RuO_6 octahedra.

CHAPTER 4

EXPERIMENTAL RESULTS OF FRUSTRATED TRANSITION METAL OXIDES

In this chapter, we will discuss the elastic properties of transition metal oxides with geometric frustration, studied using Resonant Ultrasound Spectroscopy. We have focused on three vanadium spinels AV_2O_4 (A = Zn, Mn and Fe) and five titanate pyrochlores $A_2Ti_2O_7$ (A= Y, Tb, Yb, Ho and Dy). All samples in this chapter are single crystals, except for ZnV_2O_4, which is a polycrystal.

4.1 Vanadium spinels AV_2O_4 (A = Zn, Mn and Fe)

Single crystals MnV_2O_4 and FeV_2O_4 were provided by Dr. H. Zhou at the National High Magnetic Field Laboratory. All single crystals were oriented and polished into a rectangular parallelepiped (RP) shape with faces perpendicular to the crystallographic [100] axis. Polycrystalline ZnV_2O_4 samples were home synthesized using a standard solid state reaction and its X-ray powder diffraction pattern is shown in Figure 4.1.

Table 4.1 lists the room temperature elastic constants of polycrystal ZnV_2O_4, single crystals MnV_2O_4 and FeV_2O_4, measured using RUS. For polycrystal ZnV_2O_4, only two independent elastic constants exist, C_{11} and C_{44}. For single crystals MnV_2O_4 and FeV_2O_4 with a cubic structure, three independent elastic constants exist, typically labeled C_{11}, C_{12} and C_{44} in Voigt notation. Since the sound velocity in cubic crystals is directly related to the moduli C_{11} ($v_L = (\rho/C_{11})^{1/2}$), C_{44} ($v_{T1} = (\rho/C_{44})^{1/2}$) and $C' = 1/2 * (C_{11}-C_{12})$ ($v_{T2} = (\rho/C')^{1/2}$), it is often preferred to report C_{11}, C_{44}, and C', and that is the approach we will follow in the remainder of this work. It needs to be pointed out that for polycrystals, $C' = C_{44}$.

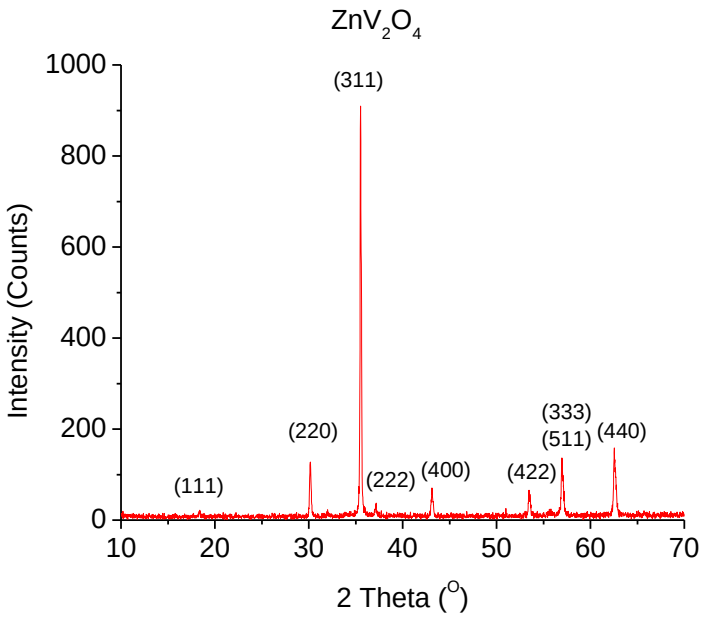

Figure 4.1 X-ray powder diffraction pattern of polycrystal ZnV_2O_4

Table 4.1 Elastic constants of vanadium spinels measured by RUS at room temperature

Composition	Mass (mg)	C_{11} (10^{11} Pa)	C' (10^{11} Pa)	C_{44} (10^{11} Pa)
ZnV_2O_4	246.8	1.3895	0.4106	0.4106
MnV_2O_4	48.8	2.1570	0.3324	0.7422
FeV_2O_4	4.9	2.4991	0.1613	0.7286

4.1.1 Polycrystal ZnV_2O_4

ZnV_2O_4 is expected to be the simplest case in vanadium spinels, since there is no magnetic moment on Zn^{2+}. As mentioned in Chapter 1, polycrystalline ZnV_2O_4 was reported to undergo two successive transitions at low temperatures: a cubic-to-tetragonal structural phase transition at T_S = 50 K followed by a transition into an antiferromagnetically ordered state at T_N = 40 K **(Ueda, 1997)**. However, single crystal ZnV_2O_4 indicated no sign of structural transition down to 2 K. Instead, it displays spin glass behavior at low temperatures without long-range magnetic order **(Ebbinghaus, 2004)**.

RUS data for polycrystalline ZnV_2O_4 are shown in Figure 4.2 and Figure 4.3. Here we only present low-temperature data below 150 K since resonant peaks of ZnV_2O_4 above 150 K have low quality factor Q and can not be well defined due to background noise. Figure 4.2 shows the temperature dependence of the shear modulus C_{44} when no magnetic field is applied. With decreasing temperature, C_{44} decreases continuously until it reaches a minimum around 50 K. This elastic softening corresponds to the cubic-to-tetragonal structural phase transition at 50 K, as reported by Ueda **(Ueda, 1997)**. However, the reported antiferromagnetic ordering at 40 K is not clear in our RUS data. Figure 4.3 shows the temperature dependence of C_{44} under different magnetic fields. No apparent field effects are observed, except that the minimum in C_{44} occurs at a slightly higher temperature under higher fields. In addition, we conducted magnetization measurement on this polycrystalline sample, and spin glass behavior is observed at low temperatures (Figure 4.4), similar to the reports by Ebbinghaus for single crystals **(Ebbinghaus, 2004)**.

Our results show that the behavior of ZnV_2O_4 is far from straight-forward, even though it was expected to be the simplest case. At this stage, it looks like the various findings are very sample-dependent and it is too early to draw major conclusions on this compound. Further investigations on well-characterized samples are needed to clarify its behavior. Neutron scattering measurements were recently carried out on

our polycrystalline sample of ZnV_2O_4 at Oak Ridge National Laboratory and refinements are currently under way.

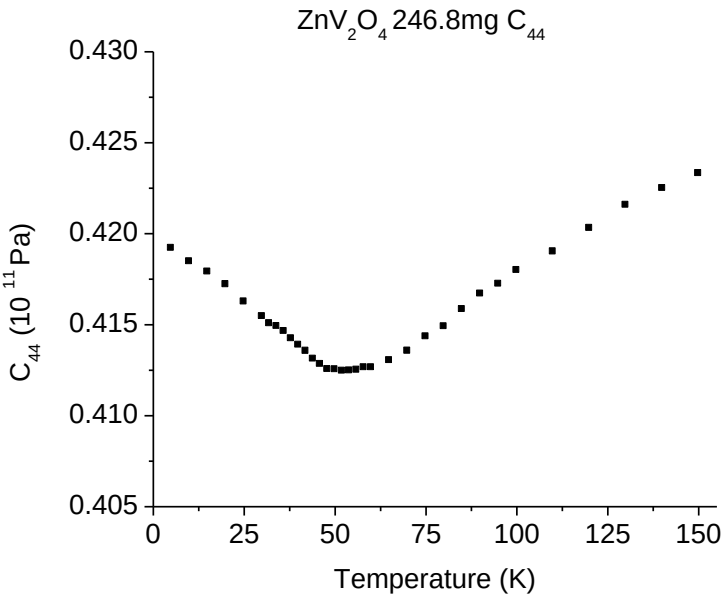

Figure 4.2 Temperature dependence of C_{44} for polycrystal ZnV_2O_4 under no magnetic field

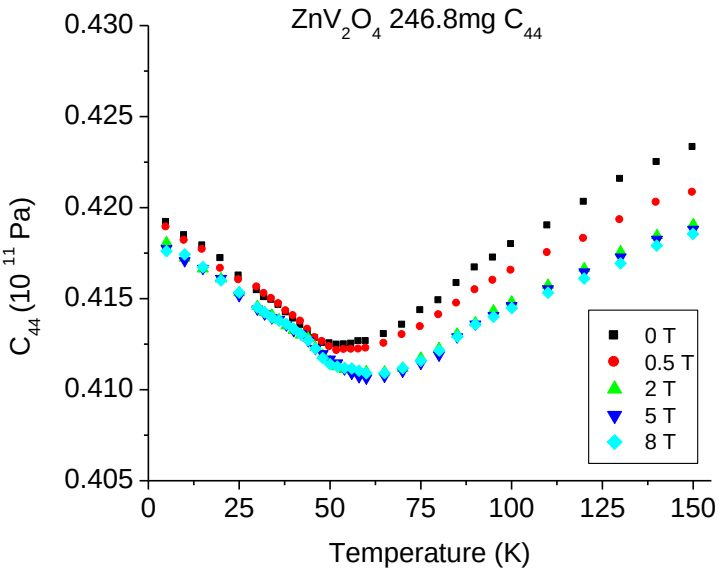

Figure 4.3 Temperature dependence of C_{44} for polycrystal ZnV_2O_4 under various magnetic fields

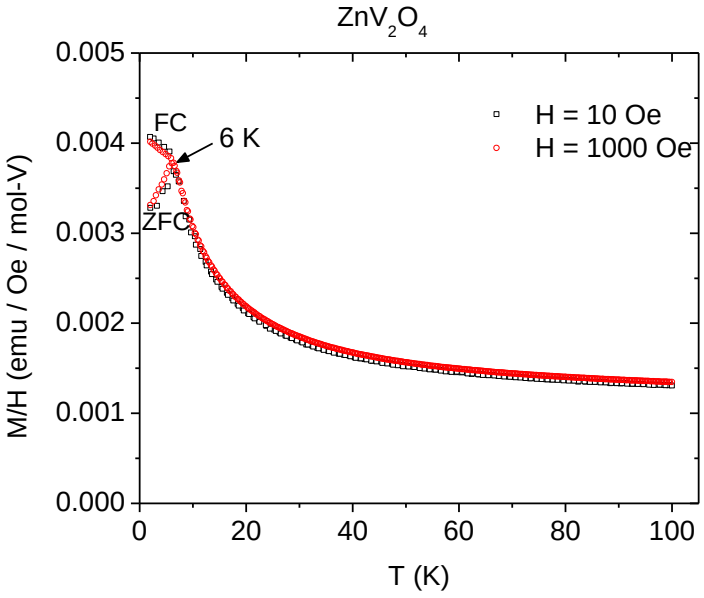

Figure 4.4 Magnetization versus temperature for polycrystal ZnV_2O_4 on the condition of field cooling (FC) and zero field cooling (ZFC) in the magnetic field of 10 Oe (black square) and 1000 Oe (red diamond)

4.1.2 MnV_2O_4 single crystal

As mentioned in Chapter 1, the case of MnV_2O_4 is more complicated than ZnV_2O_4 since magnetic ions Mn^{2+} lead to an additional superexchange interaction between Mn^{2+} and V^{3+}. MnV_2O_4 was reported to undergo two successive transitions at low temperatures: a ferrimagnetic phase transition at T_N = 56 K followed by a cubic-to-tetragonal structural transition at T_S = 53 K **(Plumier, 1987) (Adachi, 2005)**. However, there still exists controversy about the two transitions in MnV_2O_4, as there are reports that the ferrimagnetic phase transition and structural transition occur simultaneously at 57 K **(Suzuki, 2007)**.

Figure 4.5 demonstrates the temperature dependence of shear moduli C_{44} and C' under no magnetic field. Although the "normal" elastic response of a material shows a gradual "stiffening" when cooling, the elastic response of MnV_2O_4 is found to be quite unusual, displaying a softening over a wide temperature range with decreasing temperature, especially C'. The minimum of C_{44} and C' occurs at 56 K, corresponding to the cubic-to-tetragonal structural phase transition around this temperature. The small gap in the data right after 56 K is due to poor quality of the resonant spectrum during this temperature range, likely caused by the structural transition. At even lower temperatures, both C_{44} and C' are higher than the values at 56 K and C' does not change much with changing temperatures. Since the compound is tetragonal after the structural transition, the values of C_{66} are different from those of C_{44}, as shown in this figure.

The effect of a magnetic field on the elastic response of MnV_2O_4 is also investigated, and shown in Figures 4.6 and 4.7. At high temperatures, MnV_2O_4 is in the paramagnetic state and data under different magnetic fields overlap. However, at low temperatures below ~ 56 K, MnV_2O_4 is in the ferrimagnetic state, and data obtained in different magnetic fields begin to diverge. With increasing magnetic field, C' increases, while C_{44} decreases. In particular, the temperature dependence of C'

under different magnetic fields is particularly noteworthy. C' increases with decreasing temperature in the case of 0.1 T, and decreases with decreasing temperature until it flattens in the case of 0.5 T and 1 T, both of which are in contrast with the temperature-independent behavior when no field is applied. Our results are consistent with the newly found first-order transition line at low temperature under magnetic fields in the phase diagram of MnV_2O_4, ascribed to a phenomenon of field-induced alignment within the structure of tetragonal domains **(Hardy, 2008)**.

Even though further investigation is still needed to clarify the physics behind its exotic behavior, our RUS data represent direct coupling between orbital and spin degrees of freedom in MnV_2O_4 and provide insight into the complex thermodynamic behavior of this material.

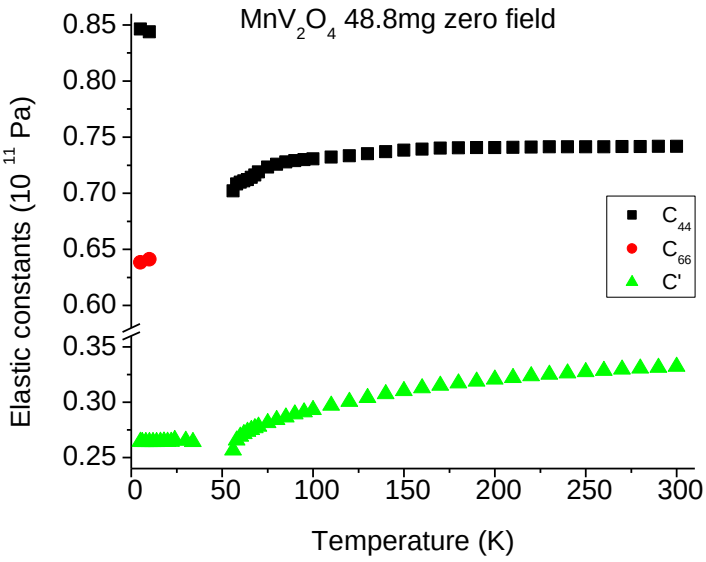

Figure 4.5 Temperature dependences of C_{44} and C' for MnV_2O_4 under no magnetic field

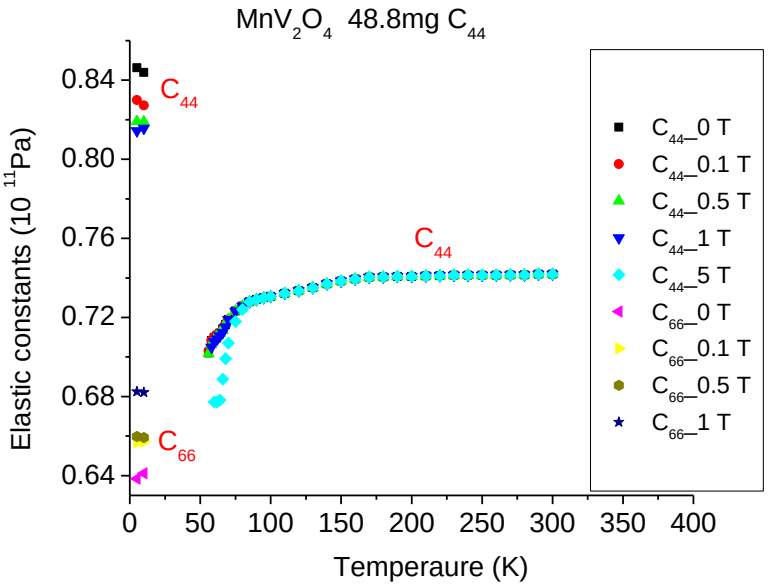

Figure 4.6 Temperature dependence of C_{44} for MnV_2O_4 under various magnetic fields

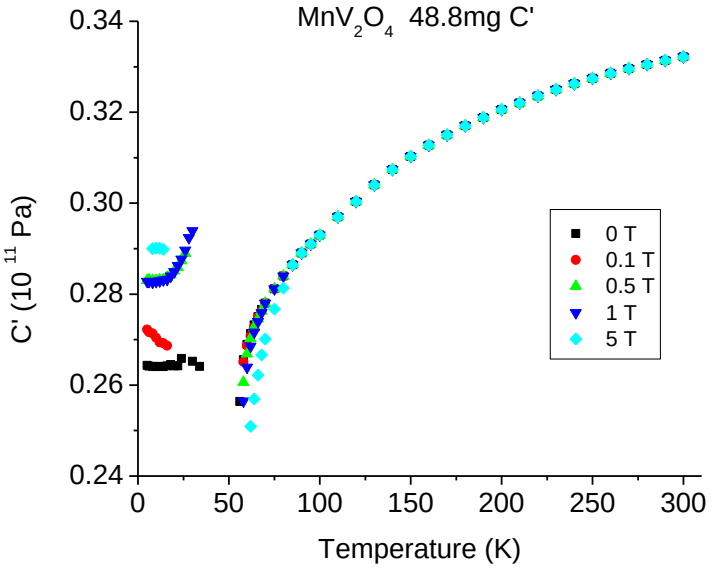

Figure 4.7 Temperature dependence of C' for MnV_2O_4 under various magnetic fields

4.1.3 FeV_2O_4 single crystal

As mentioned in Chapter 1, FeV_2O_4 has an additional degree of complexity compared to MnV_2O_4, as the Fe^{2+} ion has an additional degree of freedom. FeV_2O_4 was reported to undergo a series of structural transitions at low temperatures, including cubic-to-tetragonal transition at 140 K, tetragonal-to-orthorhombic transition at 110 K, and orthorhombic–to-tetragonal transition at 70 K **(Katsufuji, 2008)**.

The elastic response of FeV_2O_4 from 300 K to 5 K was investigated using RUS. Unfortunately, when the temperature reaches 140 K, the first structural transition temperature, all of the resonant lines disappear due to too much damping. Even though RUS data are only available above 140 K, a lot of useful information about this compound can still be deduced.

Figure 4.8 compares the temperature dependence of two resonant frequencies, Line 1 and Line 5. From the room temperature fit of FeV_2O_4 in the Appendix rusout file #3, it can be seen that Line 1 depends on shear modulus C' and Line 5 depends on shear modulus C_{44}. It is clear that those two lines behave differently upon cooling. Even though both lines show elastic softening with decreasing temperature, Line 1 decreases at a much faster pace than Line 5. Since the resonant frequencies of a given sample are directly proportional to the square-root of its elastic moduli, C' also drops much faster than C_{44} when temperature deceases, as demonstrated in Figure 4.9. Actually, C' becomes so soft that it is close to zero at 140 K. The elastic softening in this compound is a clear indication of strong correlation between elastic response and structural transition in this compound.

We also conducted magnetostriction measurement on FeV_2O_4 at low temperatures and a giant magnetostriction effect was observed, as shown in Figure 4.10. Magnetostriction is a property of ferromagnetic or ferrimagnetic materials that causes them to change dimensions during the process of magnetization. In a cubic system, the magnetostrictive strain along any arbitrary measuring direction is related

to the elastic constants by the following formula **(Engdahl, 2000)**:

$$\frac{\Delta l}{l} = \frac{-b_1}{C_{11} - C_{12}}(\alpha_x{}^2\beta_x{}^2 + \alpha_y{}^2\beta_y{}^2 + \alpha_z{}^2\beta_z{}^2 - \frac{1}{3}) + \frac{-b_2}{C_{44}}(\alpha_x\alpha_y\beta_x\beta_y + \alpha_y\alpha_z\beta_y\beta_z + \alpha_z\alpha_x\beta_z\beta_x) \quad (4.1)$$

Here, $\frac{\Delta l}{l}$ is the magnetostrictive strain. b_1 and b_2 are magneto-coupling constants. C_{11}-C_{12} (= 2 C') and C_{44} are elastic constants, α_x, α_y and α_z are the cosine of the angle between magnetization direction and axes x, y, z respectively. β_x, β_y and β_z are the cosine of the angle between the measuring direction and axes x, y, z respectively. Therefore, the soft elastic constants in FeV_2O_4 at low temperatures are expected to lead to large magnetostriction, which is exactly what we observe in Figure 4.10.

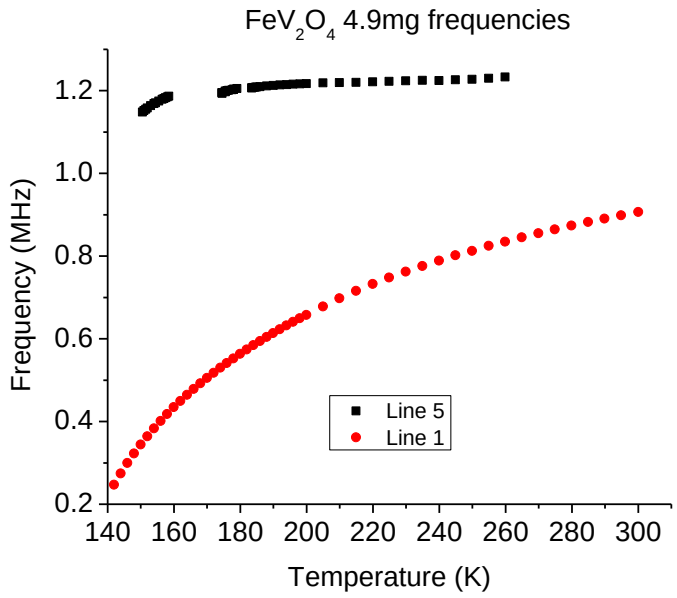

Figure 4.8 Comparison of the temperature dependence of Line 1 and Line 5 in FeV_2O_4 resonant spectrum

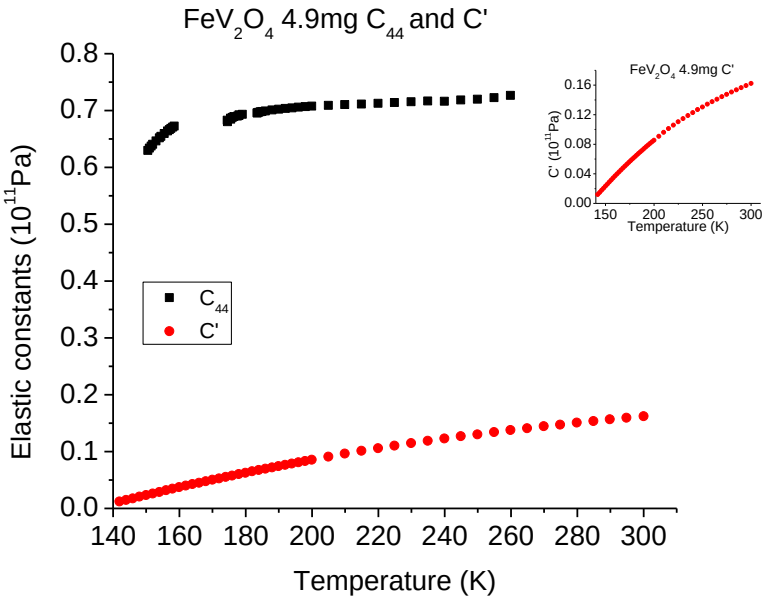

Figure 4.9 Comparison of the temperature dependence of C_{44} and C' in FeV_2O_4 (inset: magnified C' curve versus temperature)

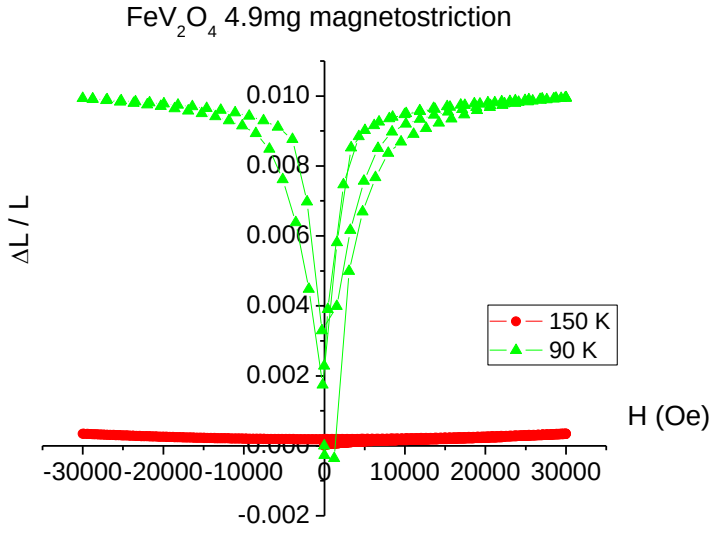

Figure 4.10 Magnetostrictive strain versus magnetic field for FeV_2O_4

4.2 Titanate pyrochlores $A_2Ti_2O_7$ (A= Y, Tb, Yb, Ho and Dy)

In this section, we will discuss the elastic response of five titanate pyrochlore compounds: $Y_2Ti_2O_7$, $Tb_2Ti_2O_7$, $Yb_2Ti_2O_7$, $Ho_2Ti_2O_7$ and $Dy_2Ti_2O_7$. $Y_2Ti_2O_7$ and two of the three $Tb_2Ti_2O_7$ samples were obtained from Bruce Gaulin's group at Mcmaster University in Canada and all the other single crystals were provided by Haidong Zhou at National High Magnetic Field Laboratory. The single crystals were oriented and cut along the [001] direction, and then polished into mm-sized samples with RP shape. Since all of the compounds are single crystals with a cubic structure, they have three independent elastic constants. Table 4.2 lists the mass and room temperature elastic constants of the titanate pyrochlore compounds used in this study.

Table 4.2 Room temperature elastic constants of various titanate pyrochlores

Composition	Mass (mg)	C_{11} (10^{11} Pa)	C' (10^{11} Pa)	C_{44} (10^{11} Pa)
$Y_2Ti_2O_7$	43.4 *	3.2945	1.1904	0.9718
$Tb_2Ti_2O_7$	116.8 *	3.6362	1.0693	0.9781
	148.2 *	3.4971	1.0759	0.9725
	30	3.4715	1.0668	0.9662
$Yb_2Ti_2O_7$	19.8	3.1841	1.0241	0.8221
$Ho_2Ti_2O_7$	67.3	3.5545	1.1623	0.9847
	69.3	3.4842	1.1617	0.9765
$Dy_2Ti_2O_7$	43.8	3.4666	1.1227	0.9738

* Samples came from Mcmaster University.

4.2.1 $Y_2Ti_2O_7$

In $Y_2Ti_2O_7$, both Y^{3+} and Ti^{4+} are nonmagnetic ions. Geometric frustration of spins is therefore not expected to be present in $Y_2Ti_2O_7$, which makes $Y_2Ti_2O_7$ an ideal reference compound for the more complex titanates with magnetic A^{3+} ions discussed below. RUS measurements on $Y_2Ti_2O_7$ were performed upon cooling between 300 K and 5 K. Figure 4.11 shows the temperature dependence of the three independent elastic constants of $Y_2Ti_2O_7$. Our experimental data are modeled quite well with the Varshni model, using equation: $C_{ij} = C_{ij}^0 - s / (e^{t/T} - 1)$ **(Varshni, 1970)**. Here, C_{ij} and C_{ij}^0 respectively represent the elastic constants at T and at 0^o K, while s and t are fitting parameters listed in Table 4.3.

As seen in Figure 4.11, all three elastic constants increase gradually with decreasing temperature until they level off at very low temperatures, which is the "normal" behavior of solids when no thermodynamic "irregularity" occurs. The elastic response of this compound is consistent with what we expected. Our RUS data confirm that no phase transition is observed in this material between 5 K and 300 K. The red lines in Figure 4.11 are Varshni model simulation of experimental data.

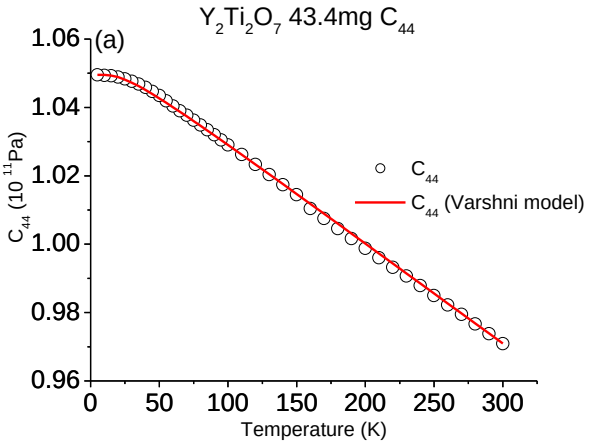

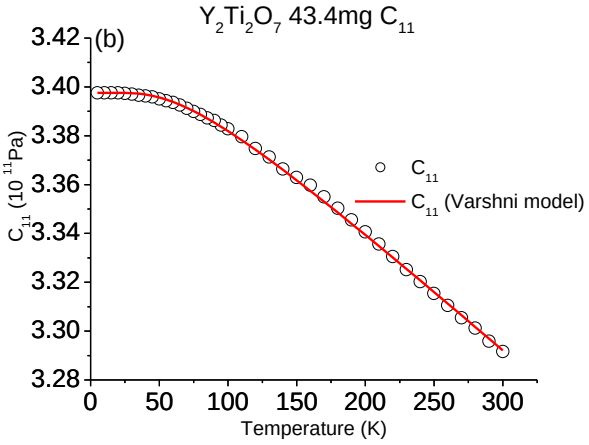

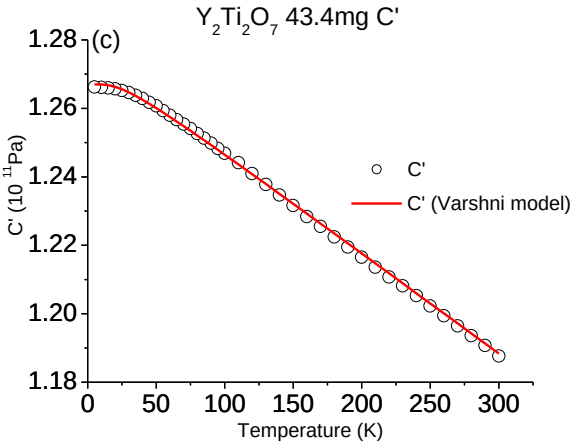

Figure 4.11 Temperature dependence of elastic constants C_{44} (a), C_{11} (b) and C' (c) for $Y_2Ti_2O_7$. Here, black open circles are experimental data, and red solid lines correspond to the Varshni model.

Table 4.3 Values of parameters in Varshni model for C_{44}, C_{11} and C' in $Y_2Ti_2O_7$

C_{ij}	C_{ij}^{0} (10^{11} Pa)	s (10^{11} Pa)	t (^{o}K)
C_{44}	1.0496	0.02	68
C_{11}	3.3976	0.1	200
C'	1.2670	0.02	68

4.2.2 Spin liquid $Tb_2Ti_2O_7$

As mentioned in Chapter 1, $Tb_2Ti_2O_7$ is a prime example of spin liquid, which displays no signs of long-range magnetic ordering down to at least 70 mK **(Gardner, 1999).**

The elastic response of three samples with the mass of 116.8 mg, 148.2 mg and 30 mg have been measured as a function of temperature (5-300 K) and magnetic field (0 – 8 T) using RUS. Sample # 2 (148.2 mg) was also sent to Los Alamos National Laboratory (LANL) for RUS measurement down to 300 mK. Since results from three samples are very similar, we only present the RUS results on sample # 2 (148.2 mg).

Figure 4.12 shows the temperature dependence of the elastic constants C_{44}, C_{11} and C' (5-300 K) for $Tb_2Ti_2O_7$ sample # 2 (148.2 mg) under zero magnetic field. The elastic constants show normal behavior at high temperatures, but all three moduli show a pronounced softening below 50 K, which is indicative of some kind of phase transition. Figure 4.13 focuses on the temperatures below 50 K, and data from LANL with temperatures below 5 K are also added to the plot. It is observed that the elastic softening continues to temperatures as low as 1.5 K. The origin of the elastic softening in $Tb_2Ti_2O_7$ is still an open question. We believe that it might be a

manifestation of a possible Jahn-Teller, cubic-to-tetragonal transition at extremely low temperature, caused by the coupling between the electronic states of a Tb^{3+} ion and the lattice strain. RUS results are in good agreement with high-resolution x-ray scattering measurements on single crystal of $Tb_2Ti_2O_7$ **(Ruff, 2007)**, which shows continuous broadening below ~ 20 K of allowed Bragg peaks and indicates the development of fluctuations above a cooperative Jahn-Teller transition at very low temperatures. Such Jahn-Teller transition is highly unusual in a pyrochlore. It needs to be pointed out that since RUS can still get a good fit with cubic structure even at 1.5 K, it is assumed that the cubic-to-tetragonal transition occurs at extremely low temperatures below 1.5 K.

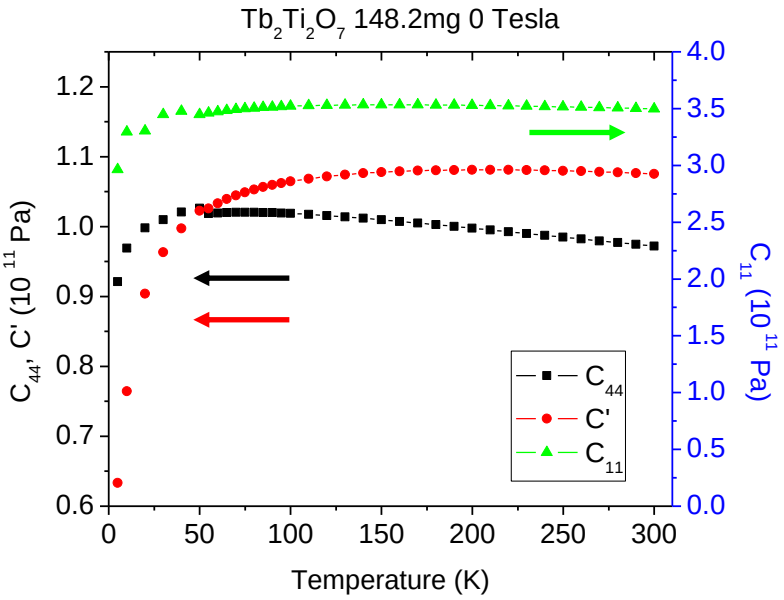

Figure 4.12 Temperature dependence of elastic constants C_{44}, C_{11} and C' under zero magnetic field for $Tb_2Ti_2O_7$ sample # 2 (148.2 mg)

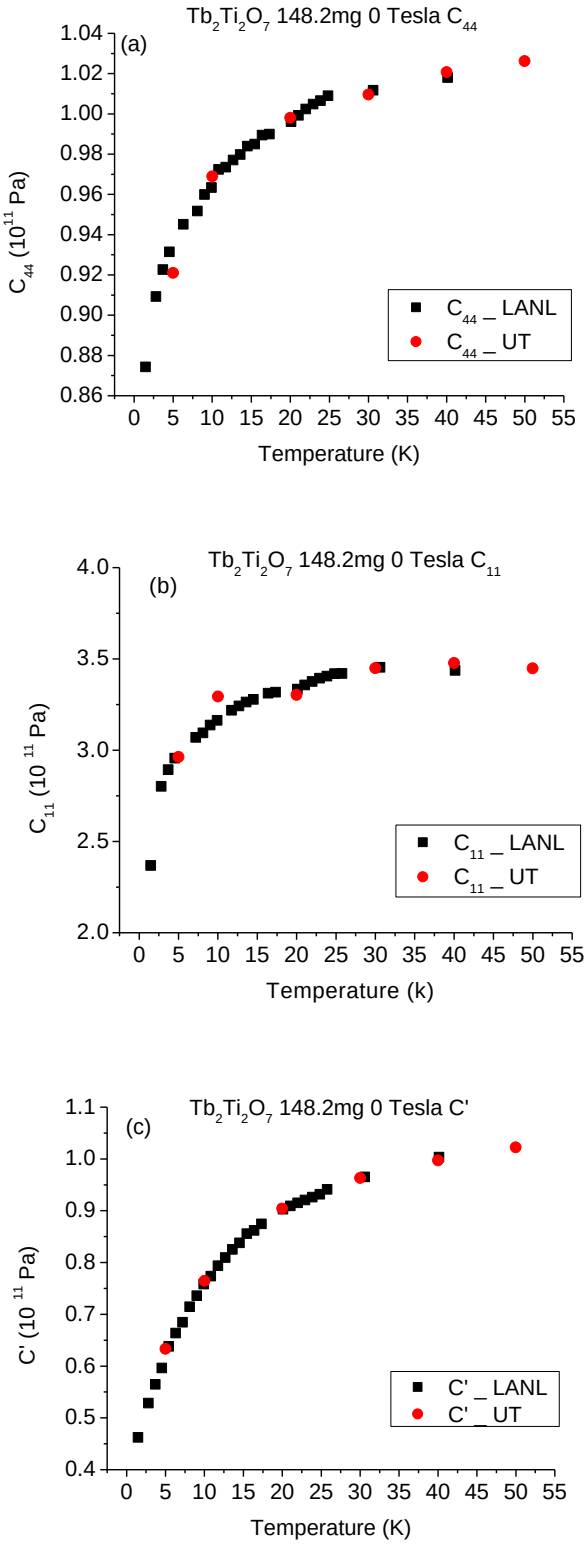

Figure 4.13 Elastic constants C_{44} (a), C_{11} (b) and C' (c) versus temperature below 50 K under zero magnetic field for $Tb_2Ti_2O_7$ sample # 2 (148.2 mg). Black squares are data taken at Los Alamos National Lab and red dots are data taken at UTK

Figures 4.14 demonstrates the temperature dependence of a representative resonant frequency of the same $Tb_2Ti_2O_7$ sample under various magnetic fields. Here we only present low temperature data, because at high temperatures above ~ 50 K, the magnetic field has no effect on the elastic response of $Tb_2Ti_2O_7$ and data at different fields overlap. Below 50 K, curves begin to diverge. In relatively small fields like 2 Tesla, large elastic softening is observed, similar to the 0 Tesla data. Starting from 5 Tesla, the elastic softening is somewhat suppressed by the magnetic field. An upturn is observed and thus a minimum in the curves is formed. The temperature where the minimum occurs, increases with increasing fields.

Figure 4.15 demonstrates that the magnetic field has similar effects on the elastic constants C_{44}, C_{11} and C' as its effect on the resonant frequencies, which is not surprising since the squared resonant frequencies are directly proportional to the elastic moduli. It needs to be pointed out that when higher fields like 5 T, 6 T and 8 T are applied and temperatures are below 10 K, RUS can only get a good fit with the tetragonal structure instead of cubic structure. This is rather surprising since no structural phase transition has been detected in other work. Only very recently did Ruff et al. perform X-ray experiments on $Tb_2Ti_2O_7$ in magnetic fields and see Bragg peak splitting, which is a hallmark of a symmetry-lowering structural phase transition **(Ruff, 2010)**.

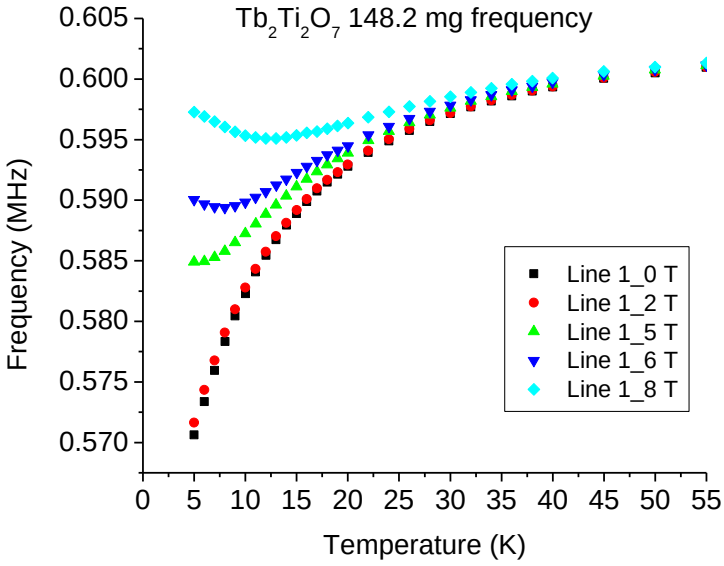

Figure 4.14 Temperature dependence of Line 1 in various magnetic fields for $Tb_2Ti_2O_7$ sample #2 (148.2 mg)

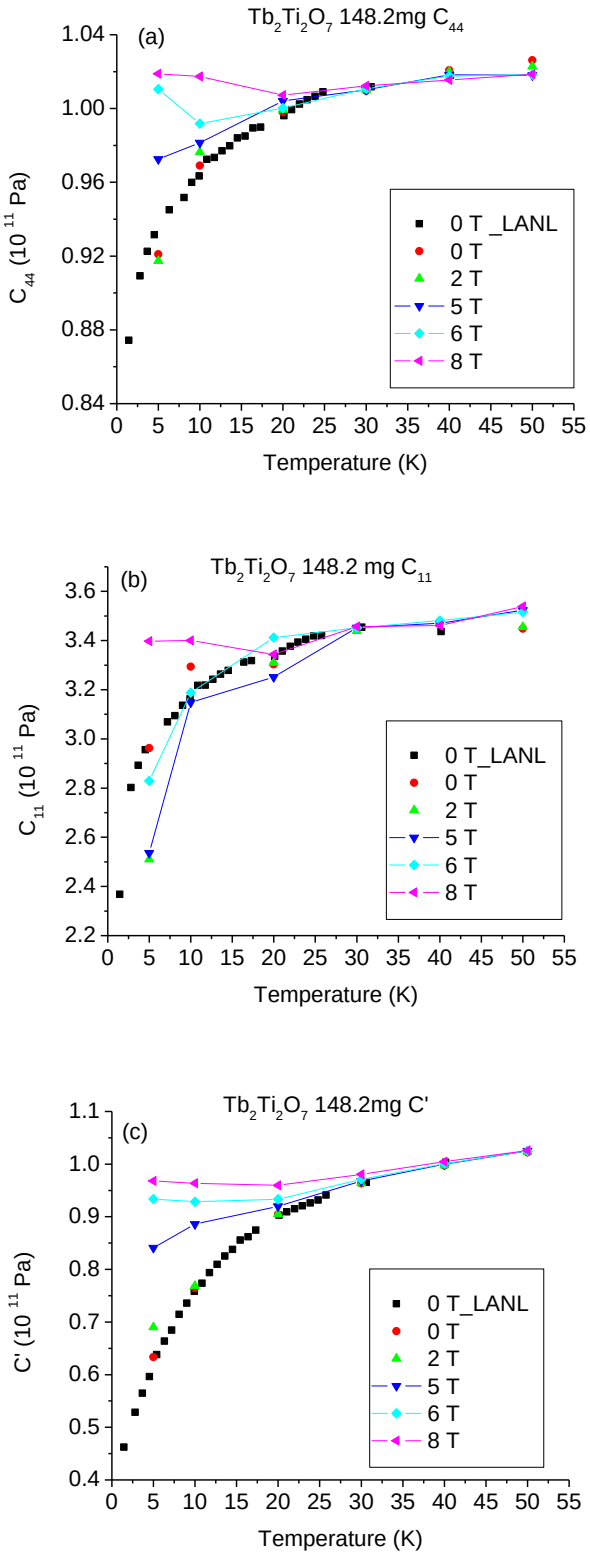

Figure 4.15 Elastic constants C_{44} (a), C_{11} (b) and C' (c) versus temperature below 50 K under various magnetic fields for $Tb_2Ti_2O_7$ sample # 2 (148.2 mg)

4.2.3 Spin liquid $Yb_2Ti_2O_7$

Like $Tb_2Ti_2O_7$, ytterbium titanate $Yb_2Ti_2O_7$ is also found to be a spin liquid. At 0.24 K, $Yb_2Ti_2O_7$ is found to experience a transition that involves the drastic slowing down of the spin fluctuations**.** RUS measurements on $Yb_2Ti_2O_7$ have been performed upon cooling between 300 K and 5 K. Figure 4.16 shows the temperature dependence of three independent elastic constants of $Yb_2Ti_2O_7$ with applied magnetic fields of 0 T, 2 T, 5 T and 9 T.

As can be seen, the elastic constants of $Yb_2Ti_2O_7$ increase with decreasing temperatures, and no elastic softening is found between 300 K and 5 K, which is consistent with the lack of structural transitions in previous studies. The temperature dependence of C_{11} shows more scatter than the other moduli, which is due to the fact that fewer resonant frequencies have significant C_{11} dependence (see Appendix Rusout file # 8), and this modulus is therefore harder to determine. Curves under different magnetic fields overlap each other, indicating no magnetic field effect in this compound. Due to the fact that our cryogenic set-up cannot reach temperatures below 5 K, we are not able to assess the reported 0.24 K transition.

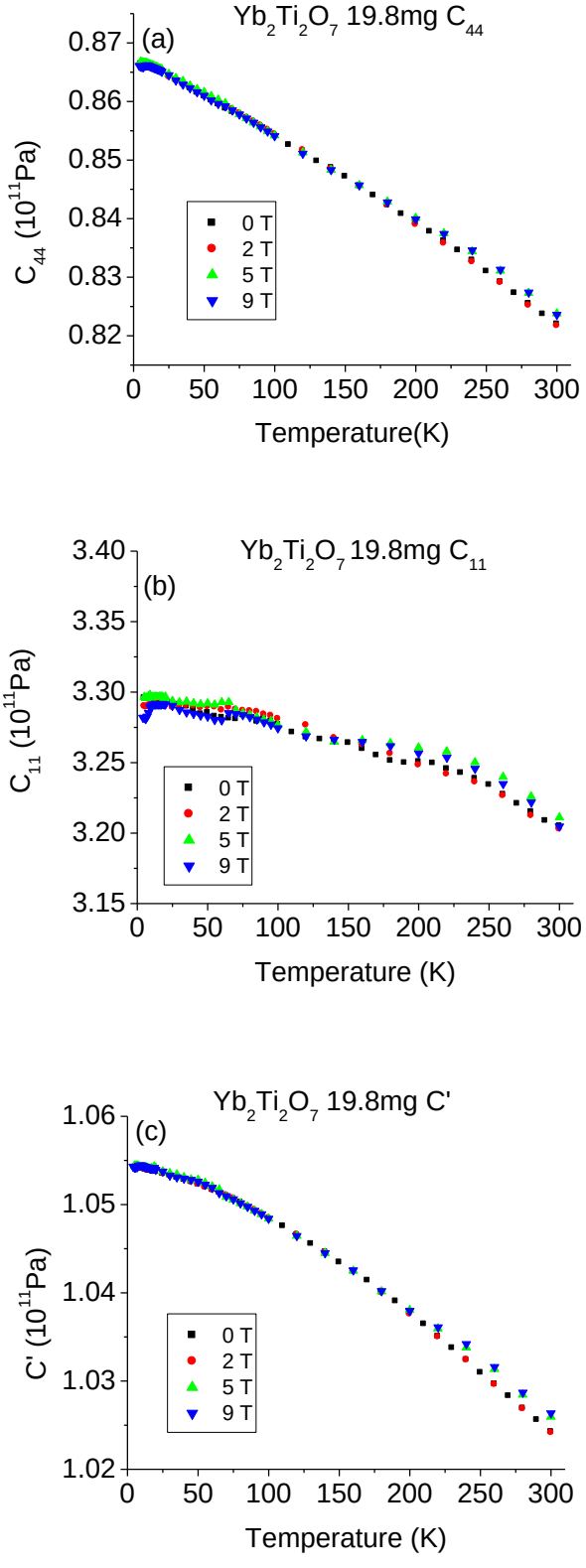

Figure 4.16 Temperature dependence of elastic constants C_{44} (a), C_{11} (b) and C' (c) in various magnetic fields for $Yb_2Ti_2O_7$

4.2.4 Spin ice $Ho_2Ti_2O_7$

$Ho_2Ti_2O_7$ was the first material proposed as a spin ice system and its elastic properties have been investigated in this section.

One $Ho_2Ti_2O_7$ sample with the mass of 67.3 mg has been measured from room temperature down to 5 K using RUS under the magnetic fields of 0 T, 5 T and 9 T. The temperature dependences of three independent elastic constants C_{44}, C' and C_{11} are illustrated in the Figure 4.17. RUS data under various magnetic fields have overlapped each other, indicating no magnetic fields effect in this compound. In addition, a second $Ho_2Ti_2O_7$ sample with the mass of 69.3 mg from the same single crystal chunk was also measured from 300 K and 5 K, and the results are demonstrated in Figure 4.18. Since magnetic field has no influence on the first sample, the RUS measurement on the second sample was only conducted under no magnetic field.

RUS data on both $Ho_2Ti_2O_7$ samples have shown no elastic anomaly in the temperature dependences of longitudinal modulus C_{11} and shear modulus C'. They increase gradually with decreasing temperature until they level off at very low temperatures. However, the temperature dependence of the shear modulus C_{44} exhibits some unusual concave behavior, which involves a clear change of slope and a bend upward at around 100 K. The deviation of C_{44} from normal behavior is somewhat puzzling. The spin ice transition occurs at ~ 0.35 K **(Harris, 1997)**, well outside our experimental range, and no other transitions have been reported for $Ho_2Ti_2O_7$. We believe that the observed anomaly is caused by the crystal electric field (CEF) effect existing in $Ho_2Ti_2O_7$. Similar concave behavior was observed in the temperature dependence of C_{55} in uranium intermetallic compound $U_2Rh_3Si_5$ and was modeled by CEF theory (**Leisure, 2005)**. The CEF effect in $Ho_2Ti_2O_7$ has been investigated by Rosenkranz et al., who determined the crystal-field parameters and corresponding energy-level scheme using neutron time-of-flight spectroscopy **(Rosenkranz, 2000)**.

Crystal field theory, developed in 1930s, is a model that describes the effect of the local environment (the crystal) on the energy levels of the atom. According to crystal

field theory, the interaction between a central metal atom and the surrounding ligands arises from the electrostatic attraction between the positively charged metal cation and negative charge on the non-bonding electrons of the ligands. As a ligand approaches the metal ion, the electrons from the ligand will be closer to some of the metal orbitals and farther away from other metal orbitals. The electrons in the metal orbitals and those in the ligands repel each other due to repulsion between like charges. Therefore, the orbital electrons closer to the ligands will have a higher energy than those further away, resulting in splitting of the metal orbital's energy. Energy splitting can occur in d- and f- orbitals. Several factors could affect the energy splitting, including the nature of the metal ion and its oxidation state, as well as the nature of the ligands and its arrangement around the metal ion. For crystals with magnetic ions, the presence of crystal field effect has played a role in the thermodynamic properties such as specific heat, magnetic susceptibility, thermal expansion and elastic constants. In particular, such effects have been reflected in the elastic behavior of many substances with rare earth ions, such as rare-earth antimonides TmSb, PrSb and SmSb **(Mullen, 1974)**, and rare-earth aluminum compounds $TmAl_2$ **(Lingner, 1983)** and $CeAl_3$ **(Niksch, 1980)**. For a system with strong CEF effect, the temperature dependence of the elastic constants depends strongly on the magneto-elastic coupling arising from the strain modulation of the CEF.

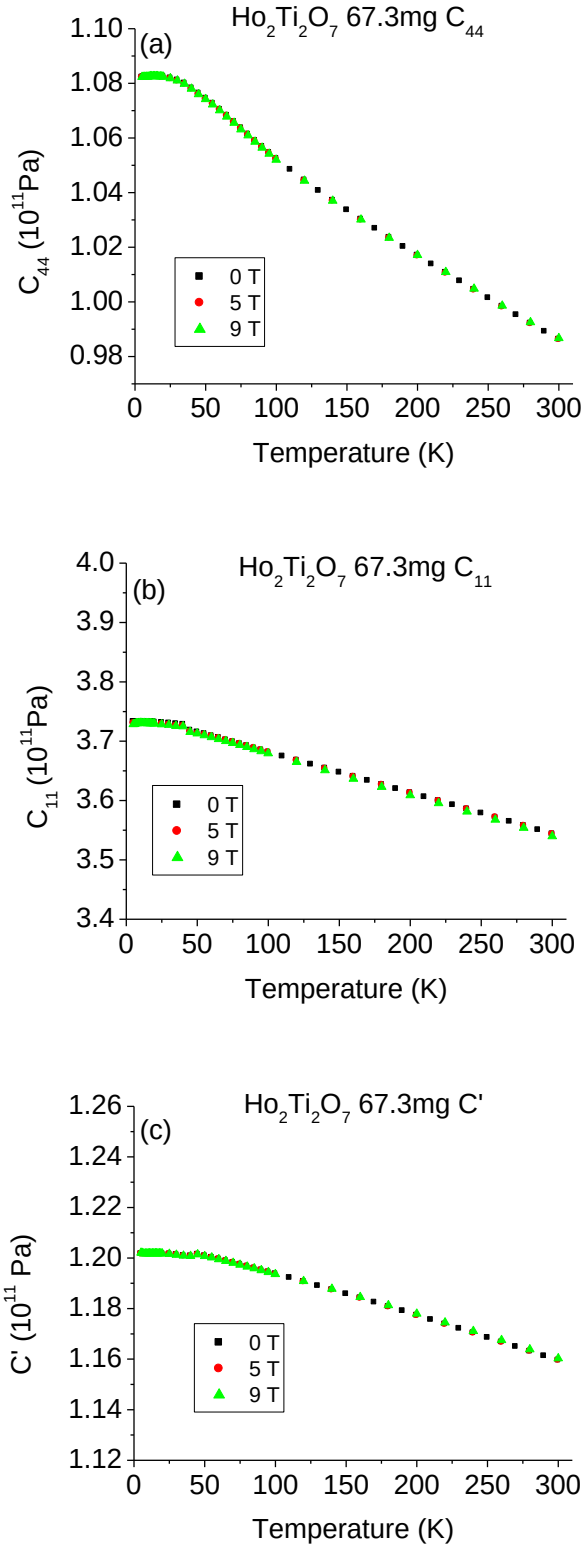

Figure 4.17 Temperature dependence of elastic constants C_{44} (a), C_{11} (b) and C' (c) in various magnetic fields for $Ho_2Ti_2O_7$ sample #1 (67.3 mg)

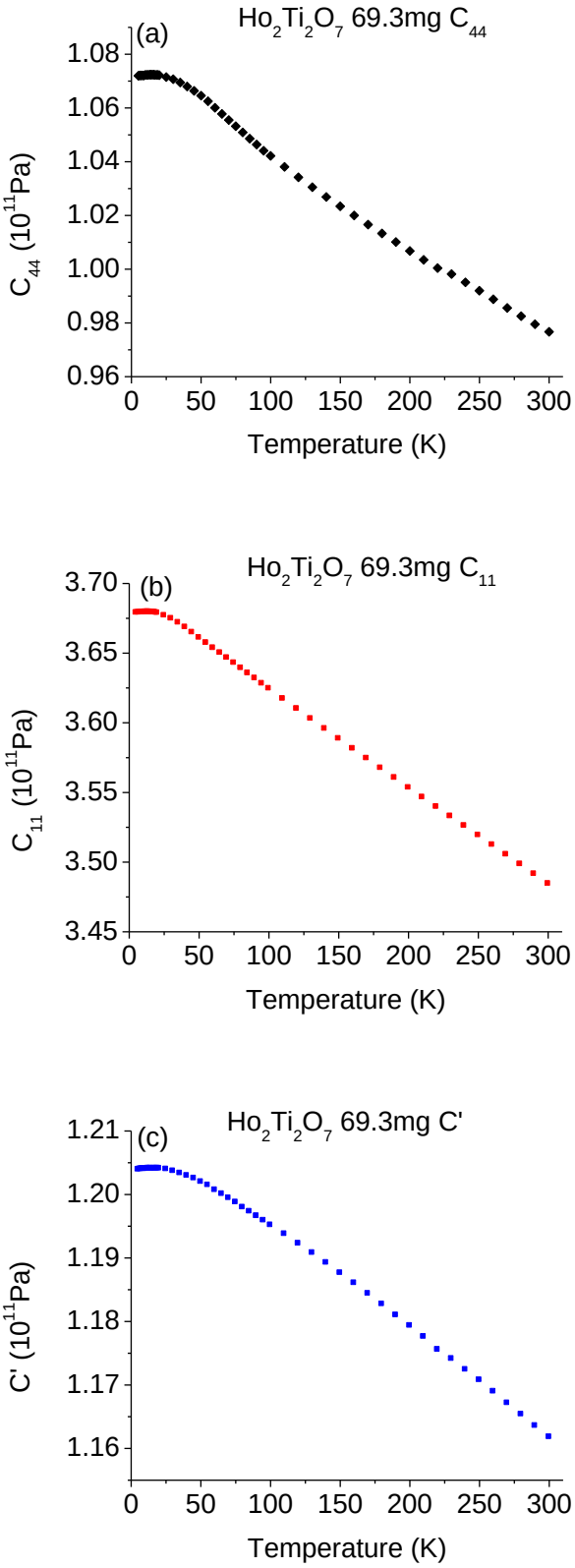

Figure 4.18 Temperature dependence of elastic constants C_{44} (a), C_{11} (b) and C' (c) under no magnetic field for $Ho_2Ti_2O_7$ sample #2 (69.3 mg)

4.2.5 Spin ice $Dy_2Ti_2O_7$

Like $Ho_2Ti_2O_7$, $Dy_2Ti_2O_7$ is also a spin ice system in which the spin ice transition occurs at ~ 0.7 K **(Ramirez, 1999)**.

The $Dy_2Ti_2O_7$ sample with a mass of 43.8 mg has been measured from room temperature down to 5 K by using RUS. The temperature dependences of three independent elastic constants C_{44}, C' and C_{11} are illustrated in Figure 4.19. The RUS measurement on the $Dy_2Ti_2O_7$ sample is only taken under no magnetic field, since no magnetic field effect is observed in similar spin ice $Ho_2Ti_2O_7$.

As can be seen in Figure 4.19, the elastic response of $Dy_2Ti_2O_7$ is very similar to that of the previously discussed spin ice $Ho_2Ti_2O_7$. No elastic anomaly is observed in the temperature dependence of longitudinal modulus C_{11} and shear modulus C', both of which increase gradually with decreasing temperature until they level off at very low temperatures. However, the temperature dependence of shear modulus C_{44} displays some unusual concave behavior, which involves a clear change of slope and a bend upward at around 100 K. It is believed that this elastic anomaly is also attributed to the strong crystal field effects of Dy^{3+} in this compound. Such effect in $Dy_2Ti_2O_7$ was investigated in previous report **(Jana, 2002)**, where the crystal field parameters were determined within 2-4% accuracy and single ion anisotropy was estimated using crystal field theory.

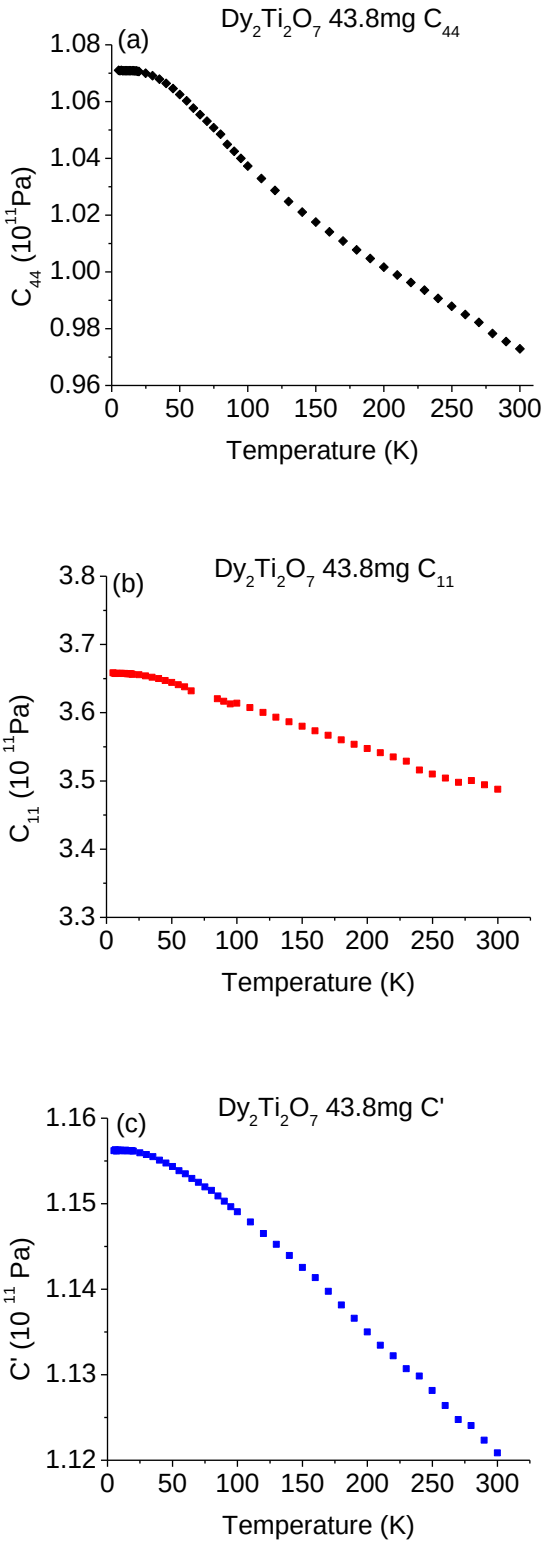

Figure 4.19 Temperature dependence of elastic constants C_{44} (a), C_{11} (b) and C' (c) for $Dy_2Ti_2O_7$

4.3 Future plans

Future plans of current research on the elastic studies of geometrically frustrated transition metal oxides include: (1) investigation of elastic response of other related vanadium spinels, such as MgV_2O_4 and CdV_2O_4; (2) measurements of elastic response of titanate pyrochlores $Yb_2Ti_2O_7$, $Ho_2Ti_2O_7$ and $Dy_2Ti_2O_7$ under higher magnetic fields and lower temperatures by collaborating with Dr. Migliori at Los Alamos National Laboratory; (3) theoretical simulation of unusual elastic behavior of spin ices $Ho_2Ti_2O_7$ and $Dy_2Ti_2O_7$, using crystal field theory; (4) investigation of elastic response of other related titanate pyrochlores, such as $Tm_2Ti_2O_7$, $Er_2Ti_2O_7$ and $Gd_2Ti_2O_7$.

CHAPTER 5

CONCLUSIONS

Resonant Ultrasound Spectroscopy has been utilized to investigate the elastic properties of two sets of transition metal oxides (TMO). One is the ruthenate $Ca_{2-x}Sr_xRuO_4$ series with a layered perovskite structure, a Mott transition system that connects the Mott insulator Ca_2RuO_4 with the unconventional superconductor Sr_2RuO_4. The other set contains geometrically frustrated materials, including vanadium spinels AV_2O_4 (A = Zn, Mn and Fe) and titanate pyrochlores $A_2Ti_2O_7$ (A = Y, Tb, Yb, Ho and Dy). RUS proves to be an excellent probe in studying these fascinating TMOs and the following conclusions have been drawn.

(1) Measurements on three $Ca_{2-x}Sr_xRuO_4$ polycrystals (x = 1.0, 0.5 and 0.3) show that the replacement of Sr by smaller Ca atoms causes a decrease of elastic constants. The gradual softening of resonant frequencies over a large temperature span in single crystals Sr_2RuO_4 (x = 2) and $Ca_{0.1}Sr_{1.9}RuO_4$ (x = 1.9) is caused by a rotational instability in the lattice. The sharp softening of resonant frequencies over a very narrow temperature range for single crystals $Ca_{1.7}Sr_{0.3}RuO_4$ (x = 0.3) and $Ca_{1.8}Sr_{0.2}RuO_4$ (x = 0.2) corresponds to the tetragonal-to-orthorhombic structural phase transition.

(2) Near the cubic-to-tetragonal structural phase transition at 50 K, elastic softening in ZnV_2O_4 is observed, while the antiferromagnetic transition at 40 K is not clear in our RUS data. With decreasing temperature, the elastic response of MnV_2O_4 displays a pronounced softening over a wide temperature range, due to the cubic-to-tetragonal structural transition around 56 K. Upon cooling, C' of FeV_2O_4 drops much faster than C_{44} and becomes so soft that it goes to almost zero around 140 K, where the cubic-to-tetragonal structural transition occurs.

(3) For $Y_2Ti_2O_7$, all three elastic constants demonstrate "normal" behavior of solids when no thermodynamic "irregularity" occurs. For spin liquid $Tb_2Ti_2O_7$, all three

elastic constants show a pronounced softening below 50 K, indicating a possible Jahn-Teller, cubic-to-tetragonal transition at very low temperatures. Upon applying magnetic field, the elastic softening in this compound is suppressed. Another spin liquid $Yb_2Ti_2O_7$ shows no elastic softening. The two spin-ice compounds, $Ho_2Ti_2O_7$ and $Dy_2Ti_2O_7$, show an unusual concave behavior in the elastic response around 100 K, which is believed to be caused by the strong crystal field effect in those two compounds.

REFERENCES

K. Adachi, T. Suzuki, K. Kato, K. Osaka, M. Takata, and T. Katsufuji, *Magnetic-field switching of crystal structure in an orbital-spin-coupled system: MnV_2O_4*, Phys. Rev. Lett. **95**, 197202 (2005) **(Adachi, 2005)**

C. S. Alexander, G. Cao, V. Dobrosavljevic, S. McCall, J. E. Crow, E. Lochner and R. P. Guertin, *Destruction of the Mott insulating ground state of Ca_2RuO_4 by a structural transition***,** Phys. Rev. B **60**, R8422 (1999) **(Alexander, 1999)**

J. G. Bednorz and K. A. Muller, *Possible high Tc superconductivity in the Ba-La-Cu-O system*, Z. Phys. B **64**, 189 (1986) **(Bednorz, 1986)**

M. Braden, A. H. Moudden, S. Nishizaki, Y. Maeno and T. Fujita, *Structural analysis of Sr_2RuO_4*, Physica C **273**, 248 (1997) **(Braden, 1997)**

M. Braden, W. Reichardt, S. Nishizaki, Y. Mori, and Y. Maeno, *Structural stability of Sr_2RuO_4***,** Phys. Rev. B **57**, 1236 (1998) **(Braden, 1998)**

S. T. Bramwell, M. N. Field, M. J. Harris and I. P. Parkin, *Bulk magnetization of the heavy rare earth titanate pyrochlores—a series of model frustrated magnets*, J. Phys.: Condens. Matter **12**, 483 (2000) **(Bramwell, 2000)**

Steven T. Bramwell and Michel J. P. Gingras, *Spin ice state in frustrated magnetic pyrochlore materials*, Science **294**, 1495 (2001) **(Bramwell, 2001)**

L. H. Brixner, *Preparation and properties of the $Ln_2Ti_2O_7$-type rare earth titanate*, Inorg. Chem **3**, 1065 (1064) **(Brixner, 1964)**

G. Cao, S. McCall, M. Shepard, J. E. Crow and R. P. Guertin, *Magnetic and transport properties of single-crystal Ca_2RuO_4: relationship to superconducting Sr_2RuO_4***,** Phy. Rev. B **56**, R2916 (1997) **(Cao, 1997)**

M. K. Crawford, R. L. Harlow,W. Marshall, Z. Li, G. Cao, R. L. Lindstrom, Q. Huang and J. W. Lynn, *Structure and magnetism of single crystal $Sr_4Ru_3O_{10}$: A ferromagnetic triple-layer ruthenate*, Phys. Rev. B **65,** 214412-1 (2002) **(Crawford, 2000)**

H. Demarest, *Cube-resonance method to determine the elastic constants of solids*, J. Acoustical Society of America **49**, 768 (1971) **(Demarest, 1971)**

J. A. Duffy,S. M. Hayden, Y. Maeno, Z. Mao,J. Kulda, and G. J. McIntyre, *Polarized-neutron scattering study of the Cooper-Pair moment in Sr_2RuO_4,* Phys. Rev. Lett. **85**, 5412 (2000) **(Duffy, 2000)**

S. G. Ebbinghaus, J. Hanss, M. Klemm, S. Horn, *Crystal structure and magnetic properties of ZnV_2O_4,* Journal of Alloys and Compounds **370**, 75 (2004) **(Ebbinghaus, 2004)**

Goran Engdahl, Handbook of Giant Magnetostrictive Materials (Academic Press 2000) **(Engdahl, 2000)**

Z. Fang and K. Terakura, *Magnetic phase diagram of $Ca_{2-x}Sr_xRuO_4$ governed by structural distortions***,** Phys. Rev. B **64**, 020509 (2001) **(Fang, 2001)**

D. B. Fraser and R.C. LeCraw, *Novel method of measuring elastic and anelastic properties of solids*, Rev. Sci. Instrum. **35**, 1113 (1964) **(Fraser, 1964)**

O. Friedt, M. Braden, G. Andre´, P. Adelmann, S. Nakatsuji and Y. Maeno, *Structural and magnetic aspects of the metal-insulator transition in $Ca_{2-x}Sr_xRuO_4$,* Phys. Rev. B **63**, 174432 (2001) **(Friedt, 2001)**

J. S. Gardner, S. R. Dunsiger, B. D. Gaulin, M. J. P. Gingras, J. E. Greedan, R. F. Kiefl, M. D. Lumsden, W. A. MacFarlane, N. P. Raju, J. E. Sonier, I. Swainson and Z. Tun, *Cooperative paramagnetism in the geometrically frustrated pyrochlore antiferromagnet $Tb_2Ti_2O_7$*, Phys. Rev. Lett. **82**, 1012 (1999) **(Gardner, 1999)**

J. S. Gardner, B. D. Gaulin, A. J. Berlinsky, P. Waldron, S. R. Dunsiger, N. P. Raju and J. E. Greedan, *Neutron scattering studies of the cooperative paramagnet pyrochlore $Tb_2Ti_2O_7$*, Phys. Rev. B **64**, 224416 (2001) **(Gardner, 2001)**

J. S. Gardner, G. Ehlers, N. Rosov, R. W. Erwin, and C. Petrovic, *Spin-spin correlations in $Yb_2Ti_2O_7$: A polarized neutron scattering study*, Phys. Rev. B **70**, 180404 (2004) **(Gardner, 2004)**

Jason S. Gardner, Michel J. P. Gingras and John E. Greedan, *Magnetic pyrochlore oxide*s, Rev. Mod. Phys. **82**, 53 (2010) **(Gardner, 2010)**

V. O. Garlea, R. Jin, D. Mandrus, B. Roessli, Q. Huang, M. Miller, A.J. Schultz and S.

E. Nagler, *Magnetic and orbital ordering in the spinel MnV_2O_4*, Phys. Rev. Lett. **100**, 066404 (2008) **(Garlea, 2008)**

Bruce D. Gaulin, *The texture of frustrated magnets*, Nature Materials **4**, 269 (2005) **(Gaulin, 2005)**

M. J. P. Gingras, B. C. den Hertog, M. Faucher, J. S. Gardner, S. R. Dunsiger, L. J. Chang, B. D. Gaulin, N. P. Raju, and J. E. Greedan, *Thermodynamic and single-ion properties of Tb^{3+} within the collective paramagnetic spin-liquid state of the frustrated pyrochlore antiferromagnet $Tb_2Ti_2O_7$*, Phys. Rev. B **62**, 6496 (2000) **(Gingras, 2000)**

John E. Greedan, *Geometrically frustrated magnetic materials*, J. Mater. Chem. **11**, 37 (2001) **(Greedan, 2001)**

John E. Greedan, *Frustrated rare earth magnetism: spin glasses, spin liquids and spin ices in pyrochlore oxides*, J. Alloy Compd. **408-412**, 444 (2006) **(Greedan, 2006)**

Vincent Hardy, Yohann Bréard, and Christine Martin, *Phase diagram of the spinel oxide MnV_2O_4*, Physical Review B **78**, 024406 (2008) **(Hardy, 2008)**

M. J. Harris, S. T. Bramwell, D. F. McMorrow, T. Zeiske, and K. W. Godfrey, *Geometrical frustration in the ferromagnetic pyrochlore $Ho_2Ti_2O_7$*, Phy. Rev. Lett **29**, 2554 (1997) **(Harris, 1997)**

Masanobu Higashi, Ryu Abe, Kazuhiro Sayama, Hideki Sugihara, and Yoshimoto Abe, *Improvement of Photocatalytic Activity of Titanate Pyrochlore $Y_2Ti_2O_7$ by Addition of Excess Y*, Chem. Lett. **34**, 1122 (2005) **(Higashi, 2005)**

J. A. Hodges, P. Bonville, A. Forget, A. Yaouanc, P. Dalmas de Réotier, G. André, M. Rams, K. Królas, C. Ritter, P. C. M. Gubbens,C. T. Kaiser,P. J. C. King,and C. Baines, *First-Order Transition in the Spin Dynamics of Geometrically Frustrated $Yb_2Ti_2O_7$*, Phys. Rev. Lett. **88**, 077204 (2002) **(Hodges, 2002)**

Shin-Ichi Ikeda, Yoshiteru Maeno, Satoru Nakatsuji, Masashi Kosaka, and Yoshiya Uwatoko, *Ground state in $Sr_3Ru_2O_7$: Fermi liquid close to a ferromagnetic instability*,

Phys. Rev. B **62**, R6089 (2000) **(Ikeda, 2000)**

M. N. Iliev, V. N. Popov, A. P. Litvinchuk, M. V. Abrashev, J. Backstrom, Y. Y. Sun, R. L. Meng and C. W. Chu, *Comparative Raman studies of Sr_2RuO_4; $Sr_3Ru_2O_7$ and $Sr_4Ru_3O_{10}$*, Physica B **358**, 138 (2005) **(Iliev, 2005)**

K. Ishida, H. Mukuda, Y. Kitaoka, K. Asayama, Z. Q. Mao, Y. Mori and Y. Maeno, *Spin-triplet superconductivity in Sr_2RuO_4 identified by ^{17}O Knight shift*, Nature (London) **396**, 658 (1998) **(Ishida, 1998)**

K. Ishida, H. Mukuda, Y. Kitaoka,Z. Q. Mao, H. Fukazawa,and Y. Maeno, *Ru NMR probe of spin susceptibility in the superconducting state of Sr_2RuO_4*, Phys. Rev. B **63**, 060507 (2001) **(Ishida, 2001)**

George Jacheli, *The ground state phases of orbitally degenerate spinel oxides*, J. of Molecular Structure **838**, 220 (2007) **(Jacheli, 2007)**

Y. M. Jana, A. Sengupna, and D. Ghosh, *Estimation of single ion anisotropy in pyrochlore $Dy_2Ti_2O_7$, a geometrically frustrated system, using crystal field theory*, Journal of Magnetism and Magnetic Materials **248**, 7 (2002) **(Jana, 2002)**

Yong Jiang, John R. Smith and G. Robert Odette, *Prediction of structural, electronic and elastic properties of $Y_2Ti_2O_7$ and Y_2TiO_5*, Acta Mater. **58**, 1536 (2010) **(Jiang, 2010)**

T. Katsufuji, K. Adachi, T. Suzuki, and M. Katsumura, *Magnetic-field switching of crystal structure in spinel MnV_2O_4*, Physica B **383**, 13 (2006) **(Katsufuji, 2006)**

Takuro Katsufuji, Takehito Suzuki, Haruki Takei, Masao Shingu, Kenichi Kato, Keiichi Osaka, Masaki Takata, Hajime Sagayama, and Taka-hisa Arima, *Structural and Magnetic Properties of Spinel FeV_2O_4 with Two Ions Having Orbital Degrees of Freedom*, J. Phys. Soc. Jpn. **77**, 053708-1 (2008) **(Katsufuji, 2008)**

S. Kramer, M. Spears and H. L. Tuller, *Conduction in titanate pyrochlores: role of dopants*, Solid State Ionics **72**, 59 (1994) **(Kramer, 1994)**

H. M. Ledbetter and S. K. Datta, *Effective wave speeds in an SiC-particle-reinforced Al composite*, J. Acoust. Soc. Am. **79**, 239 (1986) **(Ledbetter, 1986)**

S. H. Lee, D. Louca, H. Ueda, S. Park, T. J. Sato, M. Isobe, Y. Ueda., S. Rosenkranz, P. Zschack, J. Iniguez, Y. Qiu and R. Osborn, *Orbital and spin chains in ZnV_2O_4*, Phys. Rev. Lett. **93**, 156407 (2004) **(Lee, 2004)**

R. G. Leisure and F. A. Willis, *Resonant ultrasound spectroscopy***,** J. Phys.: Condens. Matter **9,** 6001 (1997) **(Leisure, 1997)**

R. G. Leisure, S. Kern, F. R. Drymiotis, H. Ledbetter, A. Migliori, and J. A. Mydosh, *Complete elastic tensor through the first-order transformation in $U_2Rh_3Si_5$*, Physical Review Letters **95**, 075506 (2005) **(Leisure, 2005)**

C. Lingner and B. Lüthi, *Elastic and magnetoelastic effects in $TmAl_2$ and other $ReAl_2$ compounds*, Journal of Magnetism and Magnetic Materials **36**, 86 (1983) **(Lingner, 1983)**

Yanbing Luan, Veerle Keppens, Rongying Jin, and David Mandrus, *Resonant ultrasound studies of the layered perovskite system $Ca_{2-x}Sr_xRuO_4$*, J. Acoust. Soc. Am. **126**, 2949 (2009) **(Luan, 2009)**

A. P. Mackenzie, R. K. W. Haselwimmer, A. W. Tyler, G. G. Lonzarich, Y. Mori, S. Nishizaki,and Y. Maeno, *Extremely strong dependence of superconductivity on disorder in Sr_2RuO_4*, Phys. Rev. Lett. **80**, 161 (1998) **(Mackenize, 1998)**

Y. Maeno, H. Hashimoto, K. Yoshida, S. Nishizaki, T. Fugita, J. G. Bednorz and F. Lichtenberg, *Superconductivity in a layered perovskite without copp*er, Nature **372**, 532 (1994) **(Maeno, 1994)**

Julian Maynard, *Resonant ultrasound spectroscopy*, Physics Today **49**, 26 (1996) **(Maynard, 1996)**

I. I. Mazin and D. J. Singh, *Competitions in layered ruthenates: ferromagnetism versus antiferromagnetism and triplet versus singlet pairing*, Phys. Rev. Lett. **82**, 4324 (1999) **(Mazin, 1999)**

A. Migliori, J. L. Sarrao, William M. Visscher, T.M. Bell, Ming Lei, Z. Fisk and R.G. Leisure, *Resonant ultrasound spectroscopic techniques for measurement of the elastic moduli of solids*, Physica B **183**, 1 (1993) **(Migliori, 1993)**

A. Migliori and J. L. Sarrano, Resonant Ultrasound Spectroscopy, (Wiley and Sons Inc., 1997) **(Migliori, 1997)**

Albert Migliori and J. D. Maynard, *Implementation of a modern resonant ultrasound spectroscopy system for the measurement of the elastic moduli of small solid specimens*, Rev. Sci. Instrum. **76**, 121301 (2005) **(Migliori, 2005)**

Albert Migliori, *Resonances and time of flight: ultrasonic probes of condensed matter go digital*, Acoustics Today **4**, 17 (2008) **(Migliori, 2008)**

I. Mirebeau, I. N. Goncharenko, P. Cadavez-Peres, S. T. Bramwell, M. J. Gingras and J. S. Gardner, *Pressure-induced crystallization of a spin liquid*, Nature **420**, 54 (2002) **(Mirebeau, 2004)**

Roderich Moessner and Arthur P. Ramirez, *Geometric frustration*, Physics Today **59**, 24 (2006) **(Moessner, 2006)**

Yukitoshi Motome and Hirokazu Tsunetsugu, *Theory of Successive Transition in Vanadium Spinels and order of orbitals and spins*, Progress of Theoretical Physics Supplement **160**, 203 (2005) **(Motome, 2005)**

M. E. Mullen, B. Lüthi, P. S. Wang, E. Bucher, L.D. Longinotti, J. P. Maita and H. R. Ott, *Magnetic-ion-lattice interaction: Rare-earth antimonides*, Physical Review B **10**, 186 (1974) **(Mullen, 1974)**

Satoru Nakatsuji, Shin-ichi lkeda and Yoshiteru Maeno, *New layered perovskite ruthenates: Ca_2RuO_4*, Physica C **282-287**, 729 (1997) **(Nakatsuji, 1997a)**

Satoru Nakatsuji, Shin-ichi Ikeda and Yoshiteru Maeno, *Ca_2RuO_4: New Mott insulators of layered ruthenate*, J. Phys. Soc. Jpn. **66**, 1868 (1997) **(Nakatsuji, 1997b)**

S. Nakatsuji and Y. Maeno, *Quasi-two-dimensional Mott transition system $Ca_{2-x}Sr_xRuO_4$*, Phys. Rev. Lett. **84**, 2666 (2000) **(Nakatsuji, 2000a)**

S. Nakatsuji and Y. Maeno, *Switching of magnetic coupling by a structural symmetry change near the Mott transition in $Ca_{2-x}Sr_xRuO_4$*, Phys. Rev. B **62**, 6458 (2000) **(Nakatsuji, 2000b)**

M. Niksch, B. Lüthi, and K. Andres, *Low-temperature elastic constants of $CeAl_3$*, Physical Review B **22**, 5774 (1980) **(Niksch, 1980)**

E. Ohmichi, S. Nagai, Y. Maeno, Z. Q. Mao and T. Ishiguro, *Magnetoresistance and susceptibility study of Sr_2RuO_4 under high magnetic fields*, Physica B **294-295**, 375 (2001) **(Ohmichi, 2001)**

Noriki Okuda, Takashi Suzuki, Zhiqiang Mao, Yoshiteru Maeno, and Toshizo Fujita, *Elastic moduli of unconventional superconductor Sr_2RuO_4*, Physica B **312-313**, 800 (2002) **(Okuda, 2002)**

Noriki Okuda, Takashi Suzuki, Zhiqiang Mao, Yoshiteru Maeno, and Toshizo Fujita, *Transverse elastic moduli in spin-triplet superconductor Sr_2RuO_4*, Physica C **388-389**, 497 (2003) **(Okuda, 2003)**

Johnpierre Paglione, C. Lupien, W. A. MacFarlane, J. M. Perz, and Louis Taillefer, Z. Q. Mao and Y. Maeno, *Elastic tensor of Sr_2RuO_4***,** , Phys. Rev. B **65**, 220506 (2002) **(Paglione, 2002)**

R. Plumier and M. Sougi, *Observation of a first order transition in the ferromagnetic spinel MnV_2O_4*, Solid State Comm. **64**, 53 (1987) **(Plumier, 1987)**

R. Plumier and M. Sougi, *Observation of a first-order transition at $T < Tc$ in MnV_2O_4*, Physica B **155**, 315 (1989) **(Plumier, 1989)**

R. Plumier and M. Sougi, *High magnetic field study of the normal spinel MnV_2O_4*, IEEE Trans. Magn. **24**, 1915 (1998) **(Plumier, 1998)**

J. M. Pruneda and Emilio Artacho, *First-principles study of structural, elastic, and bonding properties of pyrochlores*, Phys. Rev. B **72**, 085107 (2005) **(Pruneda, 2005)**

Paolo G. Radaelli, *Orbital ordering in transition metal spinels*, New Journal of Physics **7**, 53 (2005) **(Radaelli, 2005)**

A.P. Ramirez, *Strongly geometrically frustrated magnets*, Annu. Rev. Mater. Sci. **24**, 453 (1994) **(Ramirez, 1994)**

A. P. Ramirez, A. Hayashi, R. J. Cava, R. Siddharthan, and B. S. Shastry, *Zero-point entropy in 'spin ice'*, Nature **399**, 333, 1999 **(Ramirez, 1999)**

W. Rehwald, *The study of structural phase transitions by means of ultrasonic experiments*, Adv. Physics **22**, 721 (1973) **(Rehwald, 1973)**

T. M. Rice and M. Sigrist, *Sr_2RuO_4: an electronic analogue of ^3He?* J. Phys.: Condens. Matter **7**, L643 (1995) **(Rice, 1995)**

S. Rosenkranz, A. P. Ramirez, A. Hayashi, R. J. Cava, R. Siddharthan and B. S. Shastry, *Crystal-field interaction in the pyrochlore magnet $Ho_2Ti_2O_7$*, Journal of Applied Physics **87**, 5914 (2000) **(Rosenkranz, 2000)**

J. P. C. Ruff, B. D. Gaulin, J. P. Castellan, K. C. Rule, J. P. Clancy,J. Rodriguez, and H. A. Dabkowska, *Structural fluctuations in the spin-liquid State of $Tb_2Ti_2O_7$*, Phys. Rev. Lett. **99**, 237202 (2007) **(Ruff, 2007)**

J. P. C. Ruff, Z. Islam, J. P. Clancy, K. A. Ross, H. Nojiri, Y. H. Matsuda, H. A. Dabkowska, A. D. Dabkowski, and B. D. Gaulin, *Magnetoelastics of a spin liquid: X-Ray diffraction studies of $Tb_2Ti_2O_7$ in pulsed magnetic fields*, Phys. Rev. Lett. **105**, 077203 (2010) **(Ruff, 2010)**

J. L. Sarrao, S. R. Chen, W. M. Visscher, Ming Lei, U. F. Kocks, and A. Migliori, *Determination of the crystallographic orientation of a single crystal using resonant ultrasound spectroscopy*, Rev. Sci. Instru. **65**, 2139 (1994) **(Sarrao, 1994 a)**

J. L. Sarrao, D. Mandrus, A. Migliori, Z. Fisk, I. Tanaka, H. Kojima, P. C. Canfield and P. D. Kodali, *Complete elastic moduli of $La_{2-x}Sr_xCuO_4$ (x= 0.00 and 0.14) near the tetragonal-orthorhombic structural phase transition*, Phy. Rev. B **50**, 13125 (1994) **(Sarrao, 1994 b)**

Peter Schiffer, *Magnetic frustration squeezed out*, Nature **420**, 35 (2002) **(Schiffer, 2002)**

E. Schreiber, O.L. Anderson, N. Soga, and N. Warren, *Sound velocity and compressibility for lunar rocks 17 and 46 and for glass spheres from the lunar soil*, Science **167**, 732 (1970) **(Schreiber, 1970)**

E. Schreiber, O. L. Anderson and N. Soga, *Elastic constants and their measurement*, (McGraw-Hill Book Company, 1973) **(Schreiber, 1973)**

R.B. Schwarz and J.F. Vuorinen, *Resonant ultrasound spectroscopy: applications, current status and limitations*, Journal of Alloys and Compounds **310**, 243 (2000) **(Schwarz, 2000)**

M. Chandra Sekhar, K. Padmavathi, J. G. Park and P. Venugopal Reddy, *Elastic behavior of $YMnO_3$ and $ErMnO_3$ manganites*, Mod. Phy. Lett. B **17**, 1119 (2003) **(Sekhar, 2003)**

I. A. Sergienko, V. Keppens, M. McGuire, R. Jin, J. He, S. H. Curnoe, B. C. Sales, P. Blaha, D. J. Singh, K. Schwarz, and D. Mandrus, *Metallic "Ferroelectricity" in the Pyrochlore $Cd_2Re_2O_7$* , Phys. Rev. Lett. **92**, 065501 (2004) **(Sergienko, 2004)**

Y. Sidis, M. Braden, P. Bourges, B. Hennion, S. NishiZaki, Y. Maeno and Y. Mori, *Inelastic neutron scattering studies on Sr_2RuO_4*, Physica B **281&282**, 967 (2000) **(Sidis, 2000)**

S. L. Sondhi, S. M. Girvin, J. P. Carini, ans D. Shahar, *Continuous quantum phase transitions*, Rev. Mod. Phys. **69**, 315 (1997) **(Sondhi, 1997)**

T. Suzuki, M. Katsumura, K. Taniguchi, T. Arima, and T. Katsufuji, *Orbital ordering and magnetic field effect in MnV_2O_4*, Phys. Rev. Lett **98**, 127203 (2007) **(Suzuki, 2007)**

Midori Tanaka, Tetsuzi Tokoro, and Yoshimichi Aiyama, *Jahn-Teller effects on Mossbauer spectra of Fe_{57} in $FeCr_2O_4$ and FeV_2O_4*, J. Phys. Soc. Jpn. **21**, 262 (1966) **(Tanaka, 1966)**

M. A. Tanatar, S. Nagai, Z. Q. Mao, Y. Maeno, and T. Ishiguro, *Thermal conductivity study of Sr_2RuO_4 in oriented magnetic field*, Physica C **341-348**, 1841 (2000) **(Tanatar, 2000)**

O. Tchernyshyov, *Structural, orbital and magnetic order in vanadium spinels*, Phys. Rev. Lett. **93**, 157206 (2004) **(Tchernyshyov, 2004)**

Hirokazu Tsunetsugu and Yukitoshi Motome, *Magnetic transition and orbital degrees of freedom in vanadium spinels*, Phys. Rev. B **68**, 060405 (2003) **(Tsunetsugu, 2003)**

Yutaka Ueda, Naoki Fujiwara and Hiroshi Yasuoka, *Magnetic and structural transitions in* $(Li_xZn_{1-x})V_2O_4$ *with the spinel structure*, J. Phys. Soc. Jpn. **66**, 778, 1997 **(Ueda, 1997)**

Y. P. Varshni, *Temperature dependence of the elastic constants*, Physical Review B **2**, 3952 (1970) **(Varshni, 1970)**

S.-C.Wang, H.-B.Yang, A. K. P. Sekharan, S. Souma, H. Matsui, T. Sato, T. Takahashi, Chenxi Lu, Jiandi Zhang, R. Jin, D. Mandrus, E.W. Plummer, Z. Wang, and H. Ding, *Fermi Surface Topology of* $Ca_{1.5}Sr_{0.5}RuO_4$ *determined by Angle-Resolved Photoelectron Spectroscopy***,** Phys. Rev. Lett. **93**, 177007 (2004) **(Wang, 2004)**

E. O. Wollan and W. C. Koehler, *Neutron diffraction study of the magnetic properties of the series of perovskite-type compounds [(1-x)La, xCa]*MnO_3, Phys. Rev. **100**, 545 (1955) **(Wollan, 1955)**

Yasufumi Yamashita and Kazuo Ueda, *Spin-driven Jahn-Teller distortion in a pyrochlore system*, Phys. Rev. Lett. **85**, 4960 (2000) **(Yamashita, 2000)**

Brian J. Zadler, Jerome H. L. Le Rousseau, John S. Scales and Martin L. Smith, *Resonant ultrasound spectroscopy: theory and application*, Geophys. J. Int. **156**, 154 (2004) **(Zadler, 2004)**

APPENDIX

Rusout files of vanadium spinels and titanate pyrochlores

Rusout file #1

ZnV_2O_4 polycrystal 246.8mg
free moduli are c11, c44
using 10 order polynomials mass= 0.2468 gm rho= 4.460 gm/cc

n	fex	fr	%err	wt	k	i	df/d(moduli)	
1	0.214407	0.214883	0.22	1.00	4	1	0.00	1.00
2	0.287084	0.287593	0.18	1.00	6	2	0.13	0.87
3	0.365683	0.366605	0.25	1.00	7	2	0.17	0.83
4	0.390175	0.391440	0.32	1.00	6	3	0.33	0.67
5	0.396578	0.396376	-0.05	1.00	3	2	0.02	0.98
6	0.417709	0.418226	0.12	1.00	8	2	0.07	0.93
7	0.438039	0.437447	-0.14	1.00	5	1	0.04	0.96
8	0.450845	0.452652	0.40	1.00	2	2	0.07	0.93
9	0.471656	0.471190	-0.10	1.00	1	2	0.16	0.84
10	0.505273	0.506187	0.18	1.00	5	2	0.18	0.82
11	0.528174	0.527543	-0.12	1.00	4	2	0.01	0.99
12	0.532176	0.529567	-0.49	1.00	2	3	0.17	0.83
13	0.580520	0.578631	-0.33	1.00	5	3	0.32	0.68
14	0.591246	0.589859	-0.23	1.00	8	3	0.07	0.93
15	0.624542	0.624447	-0.02	1.00	7	3	0.04	0.96
16	0.629825	0.629990	0.03	1.00	1	3	0.05	0.95
17	0.643752	0.646326	0.40	1.00	6	4	0.08	0.92
18	0.664562	0.664781	0.03	1.00	8	4	0.06	0.94
19	0.679450	0.678815	-0.09	1.00	4	3	0.14	0.86
20	0.697699	0.699783	0.30	1.00	3	3	0.08	0.92
21	0.743482	0.742736	-0.10	1.00	2	4	0.04	0.96
22	0.748604	0.748066	-0.07	1.00	6	5	0.06	0.94
23	0.759650	0.757497	-0.28	1.00	2	5	0.06	0.94
24	0.771816	0.769238	-0.33	1.00	6	6	0.12	0.88
25	0.787664	0.787561	-0.01	1.00	4	4	0.02	0.98
26	0.816798	0.816089	-0.09	1.00	1	4	0.02	0.98

Bulk Modulus= 0.842

c11	c22	c33	c23	c13	c12	c44	c55	c66
1.3895	1.3895	1.3895	0.5683	0.5683	0.5683	0.4106	0.4106	0.4106

d1	d2	d3
0.52280	0.43920	0.24100

loop# 3 rms error= 0.2303 %, changed by 0.0000000 %

length of gradient vector= 0.000001 blamb= 0.000000

eigenvalues	eigenvectors
0.05554	1.00 0.03
63.53687	-0.03 1.00

chisquare increased 2% by the following % changes in independent parameters

0.72	-0.07
0.00	0.07

Rusout file #2

MnV_2O_4 Florida 48.8mg room temperature
free moduli are c11, c12, c44, cut along 100
using 10 order polynomials mass= 0.0488 gm rho= 4.684 gm/cc

n	fex	fr	%err	wt	k	i	df/d(moduli)		
1	0.629655	0.628300	-0.22	1.00	6	2	2.88	-1.97	0.09
2	0.648504	0.647998	-0.08	1.00	4	1	0.06	-0.04	0.98
3	0.696588	0.697073	0.07	1.00	7	2	2.84	-1.93	0.09
4	0.760450	0.760401	-0.01	1.00	5	1	3.23	-2.23	0.00
5	0.851686	0.850910	-0.09	1.00	1	2	2.95	-2.02	0.07
6	0.866573	0.863856	-0.31	1.00	5	2	3.18	-2.19	0.01
7	0.905593	0.903175	-0.27	1.00	6	3	2.35	-1.51	0.16
8	0.942021	0.943643	0.17	1.00	5	3	3.20	-2.20	0.00
9	0.976958	0.981275	0.44	1.00	2	2	1.86	-1.28	0.42
10	0.985723	0.981594	-0.42	1.00	3	2	0.70	-0.48	0.78
11	0.992746	0.994351	0.16	1.00	4	2	0.41	-0.28	0.87

12	1.002050	0.997803	-0.42	1.00	8	2	1.40	-0.95	0.56
13	1.163210	1.162838	-0.03	1.00	1	3	2.68	-1.85	0.17
14	1.168430	1.171788	0.29	1.00	2	3	0.60	-0.37	0.77
15	1.208470	1.210443	0.16	1.00	7	3	2.68	-1.80	0.11
16	1.210580	1.212038	0.12	1.00	1	4	3.05	-2.08	0.03
17	1.219810	1.218533	-0.10	1.00	5	4	2.73	-1.79	0.06
18	1.225750	1.227870	0.17	1.00	3	3	2.13	-1.45	0.31
19	1.241120	1.244101	0.24	1.00	5	5	2.81	-1.86	0.05
20	1.251210	1.247680	-0.28	1.00	8	3	0.26	-0.15	0.90
21	1.264110	1.262100	-0.16	1.00	7	4	2.31	-1.59	0.28
22	1.325630	1.325995	0.03	1.00	6	4	1.54	-1.05	0.51
23	1.338120	1.342590	0.33	1.00	8	4	0.67	-0.45	0.79
24	1.369570	1.368539	-0.08	1.00	1	5	2.29	-1.51	0.22
25	1.384820	1.383518	-0.09	1.00	3	4	2.24	-1.54	0.30
26	1.424370	1.424711	0.02	1.00	1	6	2.10	-1.38	0.28
27	1.457930	1.457973	0.00	1.00	2	4	1.32	-0.91	0.59
28	1.463870	1.465088	0.08	1.00	7	5	1.49	-0.99	0.50
29	1.509910	1.510304	0.03	1.00	7	6	2.19	-1.46	0.27
30	1.525810	1.527578	0.12	1.00	4	3	0.94	-0.61	0.67
31	1.543760	1.545375	0.10	1.00	3	5	3.13	-2.16	0.03

Bulk Modulus= 1.714

c11	c22	c33	c23	c13	c12	c44	c55	c66
2.1570	2.1570	2.1570	1.4922	1.4922	1.4922	0.7422	0.7422	0.7422

d1	d2	d3
0.26360	0.22510	0.17560

loop# 3 rms error= 0.2071 %, changed by -.0000001 %

length of gradient vector= 0.000001 blamb= 0.000000

eigenvalues	eigenvectors
0.00309	0.70 0.14 0.70
4.96290	0.71-0.14-0.69
33.49866	0.00-0.98 0.20

chisquare increased 2% by the following % changes in independent parameters

1.35 1.99 -0.03
0.01 -0.01 -0.14
0.01 -0.02 0.01

Rusout file # 3

FeV_2O_4 4.9 mg
free moduli are c11, c12, c44, cut along 100
free dimensions are d1, d2, d3
using 10 order polynomials mass= 0.0049 gm rho= 4.663 gm/cc

n	fex	fr	%err	wt	k	i	df/d(moduli)		
1	0.905653	0.900753	-0.54	1.00	6	2	7.36	-6.40	0.04
2	1.097130	1.099929	0.26	1.00	5	1	7.75	-6.75	0.00
3	1.140580	1.133799	-0.59	1.00	7	2	7.30	-6.34	0.04
4	1.176060	1.171833	-0.36	1.00	1	2	7.32	-6.36	0.04
5	1.236440	1.240743	0.35	1.00	4	1	0.13	-0.11	0.98
6	1.280080	1.261354	-1.46	0.00	5	2	7.67	-6.67	0.00
7	1.299950	1.299873	-0.01	1.00	6	3	6.54	-5.63	0.09
8	1.411780	1.421093	0.66	1.00	5	3	7.62	-6.63	0.00
9	1.705290	1.707506	0.13	1.00	2	2	3.23	-2.81	0.58
10	1.734880	1.731621	-0.19	1.00	8	2	2.98	-2.59	0.61
11	1.797130	1.797582	0.03	1.00	3	2	4.35	-3.79	0.43
12	1.906610	1.908425	0.10	1.00	1	3	6.12	-5.33	0.20
13	1.952530	1.954967	0.12	1.00	7	3	5.97	-5.19	0.22
14	1.959550	1.960216	0.03	1.00	1	4	7.70	-6.70	0.00
15	1.973600	1.980603	0.35	1.00	7	4	7.68	-6.68	0.00
16	2.016210	2.002208	-0.69	1.00	4	2	3.23	-2.81	0.58
17	2.087580	2.087629	0.00	1.00	5	4	7.13	-6.17	0.04
18	2.109490	2.104161	-0.25	1.00	5	5	7.17	-6.21	0.04
19	2.186980	2.182166	-0.22	1.00	3	3	5.87	-5.10	0.23
20	2.193470	2.201397	0.36	1.00	3	4	7.74	-6.74	0.00
21	2.226470	2.236274	0.44	1.00	2	3	4.63	-4.00	0.37

Bulk Modulus= 2.284

c11	c22	c33	c23	c13	c12	c44	c55	c66
2.4991	2.4991	2.4991	2.1766	2.1766	2.1766	0.7286	0.7286	0.7286

d1	d2	d3
0.12109	0.11795	0.07357

loop# 2 rms error= 0.3550 %, changed by -.0000007 %

length of gradient vector= 0.000006 blamb= 0.000000

eigenvalues	eigenvectors
0.00027	0.71-0.12 0.66-0.21 0.01 0.05
0.69090	0.71 0.12-0.66 0.21-0.01-0.05
18.66201	0.00-0.98-0.18-0.01 0.00 0.01
845.93273	0.00 0.04-0.20-0.71-0.66-0.14
1777.93695	0.00 0.04-0.19-0.63 0.75-0.05
7469.50654	0.00 0.03-0.10-0.11-0.05 0.99

chisquare increased 2% by the following % changes in independent parameters

5.47	6.29	0.02	-0.02	-0.03	-0.03
-0.02	0.02	-0.52	0.28	0.28	0.33
0.02	-0.02	-0.02	-0.24	-0.24	-0.20

Rusout file # 4

$Y_2Ti_2O_7$ 43.4mg

free moduli are c11, c12, c44, cut along 100

free dimensions are d1, d2, d3

using 10 order polynomials mass= 0.0434 gm rho= 4.831 gm/cc

n	fex	fr	%err	wt	k	i	df/d(moduli)		
1	0.782481	0.768809	-1.75	0.00	4	1	0.01	0.00	0.99
2	1.073900	1.077605	0.35	1.00	6	2	0.94	-0.20	0.27
3	1.170840	1.164649	-0.53	1.00	7	2	0.89	-0.18	0.29
4	1.212680	1.217165	0.37	1.00	3	2	0.06	-0.01	0.95
5	1.232420	1.224033	-0.68	1.00	4	2	0.05	-0.01	0.96
6	1.373480	1.378115	0.34	1.00	2	2	0.14	-0.03	0.89
7	1.432060	1.421948	-0.71	1.00	6	3	0.77	-0.11	0.34
8	1.434097	1.445297	0.78	1.00	8	2	0.47	-0.10	0.63
9	1.455530	1.459823	0.29	1.00	5	1	1.34	-0.34	0.00
10	1.501870	1.512478	0.71	1.00	8	3	0.07	0.00	0.93
11	1.523470	1.526486	0.20	1.00	1	2	0.91	-0.20	0.29

12	1.616640	1.609866	-0.42	1.00	2	3	0.68	-0.13	0.44
13	1.649460	1.648383	-0.07	1.00	5	2	1.30	-0.31	0.02
14	1.711540	1.697591	-0.81	1.00	8	4	0.27	-0.05	0.78
15	1.781640	1.814362	1.84	0.00	5	3	1.31	-0.31	0.00
16	1.898390	1.903128	0.25	1.00	4	3	0.10	0.00	0.90
17	1.903190	1.912897	0.51	1.00	7	3	0.70	-0.16	0.46
18	1.993050	2.002868	0.49	1.00	1	3	0.77	-0.15	0.38
19	2.025030	2.018615	-0.32	1.00	2	4	0.31	-0.07	0.76
20	2.032960	2.035933	0.15	1.00	6	4	0.82	-0.17	0.35
21	2.037340	2.038247	0.04	1.00	7	4	0.67	-0.11	0.43
22	2.044720	2.044211	-0.02	1.00	5	4	1.08	-0.17	0.10
23	2.055230	2.044580	-0.52	1.00	3	3	0.90	-0.19	0.29
24	2.072820	2.060478	-0.60	1.00	1	4	1.04	-0.25	0.22
25	2.129050	2.142680	0.64	1.00	5	5	1.14-	0.18	0.04
26	2.153790	2.142970	-0.50	1.00	6	5	0.44-	0.09	0.66

Bulk Modulus= 1.707

c11	c22	c33	c23	c13	c12	c44	c55	c66
3.2945	3.2945	3.2945	0.9138	0.9138	0.9138	0.9718	0.9718	0.9718

d1	d2	d3
0.25460	0.21049	0.16765

loop# 7 rms error= 0.4858 %, changed by -.0000006 %

length of gradient vector= 0.000009 blamb= 0.000000

eigenvalues	eigenvectors
0.00619	0.61 0.77-0.18 0.00 0.00 0.01
0.73193	0.79-0.60 0.12 0.00 0.00-0.01
3.66627	-0.01-0.22-0.98-0.01-0.01 0.01
707.68663	0.00 0.00 0.01-0.95-0.13 0.28
996.22934	0.00 0.00 0.01 0.25-0.85 0.45
2358.80191	0.00-0.01 0.01 0.18 0.50 0.84

chisquare increased 2% by the following % changes in independent parameters

1.12	5.25	-0.05	-0.04	0.01	0.02
0.13	-0.36	-0.12	0.01	-0.01	-0.04
-0.01	0.03	-0.25	0.02	0.03	0.02

Rusout file # 5

$Tb_2Ti_2O_7$ _oriented single crystal sample 1
free moduli are c11, c12, c44, cut along 100
free dimensions are d1, d2, d3
using 10 order polynomials mass= 0.1168 gm rho= 6.451 gm/cc

n	fex	fr	%err	wt	k	i	df/d(moduli)		
1	0.628334	0.620990	-1.17	0.00	4	1	0.03	-0.01	0.98
2	0.736198	0.730769	-0.74	1.00	4	2	0.04	-0.02	0.97
3	0.874317	0.874517	0.02	1.00	6	2	1.24	-0.48	0.24
4	0.879600	0.879654	0.01	1.00	7	2	1.23	-0.47	0.24
5	0.901931	0.904867	0.33	1.00	3	2	0.09	-0.03	0.94
6	0.906073	0.911220	0.57	1.00	2	2	0.09	-0.03	0.94
7	0.960030	0.964140	0.43	1.00	8	2	0.12	-0.05	0.93
8	1.005410	1.006637	0.12	1.00	1	2	1.32	-0.53	0.21
9	1.043460	1.046234	0.27	1.00	5	1	1.69	-0.69	0.00
10	1.086320	1.089712	0.31	1.00	6	3	0.84	-0.23	0.39
11	1.098030	1.096026	-0.18	1.00	5	2	1.69	-0.69	0.00
12	1.105410	1.104426	-0.09	1.00	8	3	0.91	-0.31	0.40
13	1.109310	1.108052	-0.11	1.00	7	3	0.85	-0.24	0.39
14	1.139500	1.144243	0.42	1.00	5	3	1.70	-0.70	0.00
15	1.173840	1.181225	0.63	1.00	1	3	0.77	-0.19	0.42
16	1.190530	1.185263	-0.44	1.00	2	3	1.04	-0.36	0.33
17	1.198750	1.199123	0.03	1.00	3	3	1.06	-0.37	0.31
18	1.229890	1.220145	-0.79	1.00	8	4	0.18	-0.07	0.89
19	1.297610	1.305451	0.60	1.00	4	3	0.07	-0.01	0.94
20	1.317300	1.318462	0.09	1.00	5	4	1.35	-0.40	0.05
21	1.365250	1.359142	-0.45	1.00	2	4	0.36	-0.14	0.78
22	1.371740	1.361782	-0.73	1.00	5	5	1.43	-0.45	0.02
23	1.375640	1.371110	-0.33	1.00	3	4	0.38	-0.15	0.77

Bulk Modulus= 2.210

c11	c22	c33	c23	c13	c12	c44	c55	c66
3.6362	3.6362	3.6362	1.4977	1.4977	1.4977	0.9781	0.9781	0.9781

d1	d2	d3
0.28603	0.25330	0.24991

loop#10 rms error= 0.4262 %, changed by 0.0000006 %

length of gradient vector= 0.000016 blamb= 0.000000

eigenvalues	eigenvectors
0.00642	0.67 0.71-0.21 0.00 0.00 0.00
1.30793	0.74-0.65 0.18 0.00 0.00 0.00
3.96391	-0.01-0.28-0.96 0.00 0.01 0.00
399.71479	0.00 0.00 0.01-0.11 0.84-0.52
511.94601	0.00 0.00 0.00 0.75-0.27-0.60
7687.71629	0.00 0.00 0.00-0.65-0.46-0.61

chisquare increased 2% by the following % changes in independent parameters

0.92 2.47 -0.03 -0.02 0.01 0.01
0.07 -0.15 -0.10 0.01 0.00 -0.01
-0.01 0.02 -0.20 0.02 0.00 -0.01

Rusout file # 6

$Tb_2Ti_2O_7$ sample2 300K
free moduli are c11, c12, c44, cut along 100
free dimensions are d1, d2, d3
using 10 order polynomials mass= 0.1482 gm rho= 6.538 gm/cc

n	fex	fr	%err	wt	k	i	df/d(moduli)		
1	0.587236	0.579542	-1.31	0.00	4	1	0.03	-0.01	0.98
2	0.664427	0.662109	-0.35	1.00	4	2	0.04	-0.01	0.98
3	0.815857	0.818316	0.30	1.00	7	2	1.20	-0.43	0.23
4	0.829712	0.827348	-0.28	1.00	6	2	1.18	-0.42	0.24
5	0.834014	0.832356	-0.20	1.00	2	2	0.08	-0.02	0.95
6	0.839116	0.842477	0.40	1.00	3	2	0.08	-0.03	0.94
7	0.876782	0.879262	0.28	1.00	8	2	0.10	-0.03	0.93
8	0.915848	0.915693	-0.02	1.00	1	2	1.25	-0.47	0.21
9	0.974381	0.976463	0.21	1.00	5	1	1.62	-0.62	0.00
10	0.988237	0.989607	0.14	1.00	7	3	0.79	-0.18	0.39
11	1.012397	1.012683	0.03	1.00	5	2	1.62	-0.62	0.00
12	1.019658	1.018053	-0.16	1.00	6	3	0.81	-0.19	0.39
13	1.022960	1.023768	0.08	1.00	8	3	0.90	-0.28	0.38

14	1.042668	1.049072	0.61	1.00	5	3	1.62	-0.62	0.00
15	1.064677	1.068380	0.35	1.00	1	3	0.74	-0.16	0.41
16	1.081834	1.080580	-0.12	1.00	3	3	0.98	-0.31	0.33
17	1.098691	1.101984	0.30	1.00	2	3	1.01	-0.32	0.31
18	1.145969	1.138822	-0.62	1.00	8	4	0.19	-0.07	0.88
19	1.194790	1.198378	0.30	1.00	4	3	0.07	-0.01	0.94
20	1.207695	1.208677	0.08	1.00	5	4	1.30	-0.34	0.04
21	1.240617	1.235245	-0.43	1.00	3	4	0.32	-0.12	0.80
22	1.246069	1.242088	-0.32	1.00	5	5	1.36	-0.38	0.02
23	1.257324	1.255366	-0.16	1.00	2	4	0.35	-0.13	0.78
24	1.272130	1.266800	-0.42	1.00	7	4	1.16	-0.40	0.24
25	1.278183	1.271208	-0.55	1.00	6	4	1.18	-0.41	0.23
26	1.290388	1.278312	-0.94	1.00	1	4	1.28	-0.46	0.17
27	1.351071	1.358793	0.57	1.00	6	5	0.64	-0.22	0.58
28	1.357824	1.365127	0.54	1.00	1	5	0.79	-0.26	0.48
29	1.362076	1.366387	0.32	1.00	7	5	0.61	-0.21	0.60

Bulk Modulus= 2.063

c11	c22	c33	c23	c13	c12	c44	c55	c66
3.4971	3.4971	3.4971	1.3454	1.3454	1.3454	0.9725	0.9725	0.9725

d1	d2	d3
0.30314	0.27026	0.27669

loop# 6 rms error= 0.3844 %, changed by 0.0000000 %

length of gradient vector= 0.000039 blamb= 0.000000

eigenvalues	eigenvectors
0.00888	0.67-0.70 0.26 0.00 0.00 0.00
1.50840	0.75 0.63-0.22 0.00 0.00 0.00
4.80286	-0.01 0.34 0.94 0.00-0.01 0.00
340.87130	0.00 0.00-0.01 0.24-0.81-0.54
445.68457	0.00 0.00 0.00 0.56 0.56-0.60
10568.33075	0.00 0.00 0.00-0.79 0.16-0.59

chisquare increased 2% by the following % changes in independent parameters

0.82	2.39	-0.03	-0.02	0.01	0.01
-0.07	0.15	0.12	-0.01	0.01	0.00
0.01	-0.03	0.18	-0.01	0.00	0.00

Rusout file # 7

$Tb_2Ti_2O_7$ Florida 30 mg sample 3
free moduli are c11, c12, c44, cut along 100
using 10 order polynomials mass= 0.0300 gm rho= 6.647 gm/cc

n	fex	fr	%err	wt	k	i	df/d(moduli)		
1	0.754567	0.750039	-0.60	1.00	4	1	0.01	0.00	0.99
2	1.055650	1.057194	0.15	1.00	6	2	1.19	-0.42	0.23
3	1.228690	1.228452	-0.02	1.00	7	2	1.08	-0.35	0.27
4	1.237040	1.237584	0.04	1.00	3	2	0.07	-0.02	0.95
5	1.321130	1.329879	0.66	1.00	6	3	0.88	-0.21	0.33
6	1.384700	1.394894	0.74	1.00	4	2	0.10	-0.04	0.94
7	1.433560	1.432029	-0.11	1.00	8	2	0.59	-0.20	0.60
8	1.449400	1.449937	0.04	1.00	5	1	1.61	-0.61	0.00
9	1.480620	1.461493	-1.29	1.00	1	2	1.10	-0.36	0.27
10	1.491190	1.488363	-0.19	1.00	2	2	0.63	-0.23	0.60
11	1.583620	1.587514	0.25	1.00	2	3	0.31	-0.06	0.76
12	1.624910	1.626812	0.12	1.00	5	2	1.52	-0.53	0.01
13	1.639500	1.639498	0.00	1.00	8	3	0.09	-0.02	0.92
14	1.800070	1.804905	0.27	1.00	5	3	1.48	-0.48	0.00
15	1.902110	1.894364	-0.41	1.00	8	4	0.32	-0.10	0.78
16	1.986380	1.989660	0.17	1.00	7	3	0.73	-0.27	0.54
17	2.011000	2.024578	0.68	1.00	1	3	1.06	-0.39	0.33
18	2.052590	2.040002	-0.61	1.00	4	3	0.15	-0.02	0.87
19	2.090470	2.090905	0.02	1.00	2	4	0.34	-0.11	0.77
20	2.108110	2.109252	0.05	1.00	6	4	0.66	-0.21	0.55
21	2.197070	2.194962	-0.10	1.00	6	5	0.51	-0.16	0.66
22	2.243640	2.241143	-0.11	1.00	3	3	0.80	-0.29	0.49
23	2.297490	2.306401	0.39	1.00	1	4	1.03	-0.35	0.32
24	2.302470	2.306839	0.19	1.00	6	6	0.45	-0.15	0.70
25	2.318370	2.309718	-0.37	1.00	5	4	1.22	-0.36	0.14
26	2.326530	2.316315	-0.44	1.00	7	4	1.05	-0.34	0.29
27	2.332480	2.341550	0.39	1.00	2	5	0.43	-0.13	0.70
28	2.353790	2.360082	0.27	1.00	5	5	1.25	-0.39	0.14
29	2.382120	2.367440	-0.62	1.00	3	4	1.14	-0.38	0.24
30	2.434880	2.444667	0.40	1.00	4	4	0.39	-0.14	0.75

Bulk Modulus= 2.049

c11	c22	c33	c23	c13	c12	c44	55	c66
3.4715	3.4715	3.4715	1.3379	1.3379	1.3379	0.9662	0.9662	0.9662

d1	d2	d3
0.20500	0.18150	0.12130

loop# 4 rms error= 0.4305 %, changed by -.0000002 %

length of gradient vector= 0.000000 blamb= 0.000000

eigenvalues	eigenvectors
0.00356	0.66 0.71 0.23
1.23034	0.75-0.63-0.20
5.99473	-0.01-0.30 0.95

chisquare increased 2% by the following % changes in independent parameters

1.51 4.44 -0.05
0.09 -0.20 -0.13
0.01 -0.03 0.19

Rusout file # 8

$Yb_2Ti_2O_7$ 19.8mg
free moduli are c11, c12, c44, cut along 100
using 10 order polynomials mass= 0.0198 gm rho= 6.138 gm/cc

n	fex	fr	%err	wt	k	i	df/d(moduli)		
1	0.851266	0.848283	-0.35	1.00	4	1	0.01	0.00	0.99
2	1.271140	1.273151	0.16	1.00	6	2	1.12	-0.37	0.25
3	1.355770	1.356614	0.06	1.00	3	2	0.05	-0.01	0.96
4	1.448140	1.447668	-0.03	1.00	4	2	0.07	-0.02	0.95
5	1.469990	1.468630	-0.09	1.00	7	2	0.97	-0.28	0.32
6	1.489380	1.490874	0.10	1.00	6	3	0.75	-0.13	0.38
7	1.585960	1.586923	0.06	1.00	1	2	0.97	-0.29	0.32

8	1.643340	1.642363	-0.06	1.00	8	2	0.56	-0.18	0.62
9	1.647120	1.646008	-0.07	1.00	2	2	0.35	-0.12	0.77
10	1.705050	1.703884	-0.07	1.00	5	1	1.55	-0.55	0.00
11	1.726710	1.730024	0.19	1.00	8	3	0.13	-0.01	0.89
12	1.737580	1.737801	0.01	1.00	2	3	0.43	-0.10	0.67
13	1.873660	1.872257	-0.07	1.00	5	2	1.47	-0.47	0.00
14	2.032060	2.036302	0.21	1.00	5	3	1.41	-0.42	0.00
15	2.098930	2.100358	0.07	1.00	8	4	0.32	-0.09	0.77
16	2.197250	2.200793	0.16	1.00	4	3	0.10	-0.01	0.91
17	2.203190	2.201219	-0.09	1.00	2	4	0.32	-0.09	0.77
18	2.250010	2.251060	0.05	1.00	7	3	0.78	-0.27	0.49
19	2.281040	2.282129	0.05	1.00	1	3	0.89	-0.31	0.41
20	2.367050	2.364325	-0.12	1.00	6	4	0.83	-0.25	0.42
21	2.411300	2.414318	0.13	1.00	6	5	0.35	-0.09	0.75
22	2.484640	2.487671	0.12	1.00	1	4	0.95	-0.27	0.33
23	2.491310	2.488861	-0.10	1.00	7	4	0.92	-0.26	0.34
24	2.519270	2.512520	-0.27	1.00	5	4	1.19	-0.31	0.12
25	2.526290	2.528626	0.09	1.00	3	3	0.93	-0.29	0.37
26	2.553130	2.557307	0.16	1.00	6	6	0.48	-0.16	0.68
27	2.567050	2.566571	-0.02	1.00	3	4	0.82	-0.25	0.44
28	2.590230	2.589463	-0.03	1.00	5	5	1.21	-0.32	0.11
29	2.677200	2.676222	-0.04	1.00	7	5	1.07	-0.31	0.24
30	2.688840	2.682765	-0.23	1.00	2	5	0.41	-0.11	0.70

Bulk Modulus= 1.819

c11	c22	c33	c23	c13	c12	c44	c55	c66
3.1841	3.1841	3.1841	1.1360	1.1360	1.1360	0.8221	0.8221	0.8221

d1	d2	d3
0.17370	0.16450	0.11290

loop# 2 rms error= 0.1331 %, changed by -.0004116 %

length of gradient vector= 0.000000 blamb= 0.000000

eigenvalues	eigenvectors
0.00605	0.65 0.73 0.20
1.33763	0.76-0.63-0.16
7.97276	-0.01-0.26 0.97

chisquare increased 2% by the following % changes in independent parameters

0.38 1.25 -0.01
0.03 -0.07 -0.04
0.00 -0.01 0.06

Rusout file # 9

$Ho_2Ti_2O_7$ 67.3mg sample 1
free moduli are c11, c12, c44, cut along 100
using 10 order polynomials mass= 0.0673 gm rho= 6.989 gm/cc

n	fex	fr	%err	wt	k	i	df/d(moduli)		
1	0.670835	0.666921	-0.58	1.00	4	1	0.02	-0.01	0.99
2	0.933017	0.935746	0.29	1.00	6	2	1.05	-0.31	0.26
3	0.943972	0.953351	0.99	1.00	4	2	0.05	-0.02	0.97
4	0.997549	0.982881	-1.47	0.00	7	2	1.00	-0.29	0.28
5	1.024970	1.025313	0.03	1.00	3	2	0.07	-0.02	0.95
6	1.104990	1.107385	0.22	1.00	2	2	0.11	-0.03	0.92
7	1.195270	1.193892	-0.12	1.00	8	2	0.22	-0.07	0.85
8	1.212980	1.213134	0.01	1.00	5	1	1.50	-0.50	0.00
9	1.227430	1.228924	0.12	1.00	6	3	0.81	-0.17	0.36
10	1.255470	1.256567	0.09	1.00	8	3	0.48	-0.11	0.63
11	1.264230	1.262243	-0.16	1.00	1	2	1.07	-0.33	0.26
12	1.349340	1.350816	0.11	1.00	5	2	1.48	-0.49	0.01
13	1.369090	1.369474	0.03	1.00	2	3	0.82	-0.22	0.40
14	1.387460	1.384143	-0.24	1.00	8	4	0.24	-0.07	0.83
15	1.459310	1.463738	0.30	1.00	5	3	1.50	-0.50	0.00
16	1.485900	1.484556	-0.09	1.00	7	3	0.81	-0.21	0.39
17	1.553790	1.553218	-0.04	1.00	1	3	0.75	-0.16	0.41
18	1.557810	1.557432	-0.02	1.00	4	3	0.09	-0.01	0.92
19	1.584160	1.580026	-0.26	1.00	3	3	0.99	-0.28	0.29
20	1.623410	1.624430	0.06	1.00	5	4	1.18	-0.26	0.08
21	1.651330	1.646497	-0.29	1.00	2	4	0.35	-0.10	0.76
22	1.669150	1.667098	-0.12	1.00	6	4	0.99	-0.29	0.30
23	1.679180	1.676597	-0.15	1.00	7	4	0.77	-0.23	0.46
24	1.694250	1.689758	-0.27	1.00	1	4	1.22	-0.41	0.19
25	1.716580	1.714220	-0.14	1.00	5	5	1.28	-0.30	0.03
26	1.747180	1.752105	0.28	1.00	7	5	0.95	-0.26	0.31
27	1.750610	1.754671	0.23	1.00	6	5	0.50	-0.14	0.65

28	1.777080	1.771963	-0.29	1.00	3	4	0.58	-0.19	0.61
29	1.797430	1.797281	-0.01	1.00	1	5	0.98	-0.26	0.28
30	1.876600	1.876188	-0.02	1.00	6	6	0.29	-0.07	0.78

Bulk Modulus= 2.005

c11	c22	c33	c23	c13	c12	c44	c55	c66
3.5545	3.5545	3.5545	1.2299	1.2299	1.2299	0.9847	0.9847	0.9847

d1	d2	d3
0.25180	0.20990	0.18220

loop# 2 rms error= 0.2752 %, changed by -.0000307 %

length of gradient vector= 0.000001 blamb= 0.000000

eigenvalues	eigenvectors
0.00706	0.65 0.73 0.21
1.16480	0.76-0.63-0.17
5.27597	-0.01-0.27 0.96

chisquare increased 2% by the following % changes in independent parameters

0.65	2.17	-0.03
0.06	-0.14	-0.08
0.01	-0.02	0.13

Rusout file # 10

$Ho_2Ti_2O_7$ sample 2 69.3mg
free moduli are c11, c12, c44, cut along 100
using 10 order polynomials mass= 0.0693 gm rho= 6.978 gm/cc

n	fex	fr	%err	wt	k	i	df/d(moduli)		
1	0.668194	0.663599	-0.69	1.00	4	1	0.02	0.00	0.99
2	0.926053	0.933330	0.79	1.00	4	2	0.05	-0.02	0.97
3	0.959970	0.951079	-0.93	1.00	6	2	1.05	-0.31	0.26
4	1.005230	1.004616	-0.06	1.00	3	2	0.06	-0.01	0.95
5	1.019090	1.017640	-0.14	1.00	7	2	0.98	-0.27	0.29
6	1.112020	1.111730	-0.03	1.00	2	2	0.11	-0.03	0.92

7	1.161830	1.160973	-0.07	1.00	6	3	0.76	-0.13	0.37
8	1.164770	1.165308	0.05	1.00	8	2	0.17	-0.05	0.89
9	1.191910	1.191421	-0.04	1.00	1	2	1.02	-0.29	0.28
10	1.216280	1.219535	0.27	1.00	5	1	1.48	-0.48	0.00
11	1.246340	1.244626	-0.14	1.00	8	3	0.56	-0.13	0.57
12	1.311540	1.314370	0.22	1.00	2	3	0.76	-0.19	0.43
13	1.325270	1.327247	0.15	1.00	5	2	1.45	-0.45	0.01
14	1.414840	1.413296	-0.11	1.00	8	4	0.25	-0.07	0.82
15	1.420230	1.423025	0.20	1.00	5	3	1.45	-0.45	0.00
16	1.489200	1.490157	0.06	1.00	7	3	0.80	-0.19	0.40
17	1.530020	1.530594	0.04	1.00	1	3	0.77	-0.17	0.40
18	1.535840	1.535351	-0.03	1.00	4	3	0.08	0.00	0.92
19	1.576540	1.575043	-0.09	1.00	2	4	0.30	-0.09	0.78
20	1.583440	1.581098	-0.15	1.00	3	3	0.99	-0.26	0.28
21	1.610760	1.608862	-0.12	1.00	5	4	1.18	-0.25	0.07
22	1.640820	1.638910	-0.12	1.00	6	4	0.96	-0.26	0.31
23	1.660450	1.659554	-0.05	1.00	7	4	0.82	-0.24	0.42
24	1.667470	1.668470	0.06	1.00	1	4	1.11	-0.36	0.24
25	1.683080	1.682190	-0.05	1.00	5	5	1.23	-0.27	0.03
26	1.737040	1.739631	0.15	1.00	7	5	0.94	-0.24	0.30
27	1.754870	1.753423	-0.08	1.00	3	4	0.56	-0.18	0.62
28	1.757930	1.762464	0.26	1.00	6	5	0.50	-0.15	0.65
29	1.767230	1.766465	-0.04	1.00	1	5	0.95	-0.24	0.29
30	1.831280	1.827415	-0.21	1.00	6	6	0.28	-0.06	0.79
31	1.897430	1.899026	0.08	1.00	3	5	0.40	-0.08	0.68
32	1.907320	1.903540	-0.20	1.00	1	6	1.20	-0.36	0.16
33	1.914110	1.907627	-0.34	1.00	2	5	0.45	-0.11	0.66
34	1.937580	1.942727	0.27	1.00	6	7	0.66	-0.16	0.50
35	1.987220	1.992333	0.26	1.00	4	4	0.38	-0.12	0.74
36	1.998450	1.996694	-0.09	1.00	7	6	1.06	-0.31	0.25
37	2.021730	2.023700	0.10	1.00	5	6	0.93	0.02	0.05
38	2.028090	2.030979	0.14	1.00	8	5	0.43	-0.12	0.69
39	2.083620	2.093423	0.47	1.00	2	6	0.53	-0.13	0.61
40	2.088060	2.093531	0.26	1.00	5	7	0.82	-0.22	0.40
41	2.105770	2.106514	0.04	1.00	7	7	0.36	-0.09	0.73
42	2.128570	2.130438	0.09	1.00	3	6	0.83	-0.23	0.41
43	2.141960	2.139142	-0.13	1.00	8	6	0.44	-0.10	0.66
44	2.153790	2.147718	-0.28	1.00	4	5	0.52	-0.12	0.60
45	2.205410	2.209871	0.20	1.00	1	7	0.66	-0.18	0.51
46	2.227430	2.228703	0.06	1.00	1	8	0.37	-0.09	0.73
47	2.240640	2.234198	-0.29	1.00	4	6	0.38	-0.09	0.71
48	2.250010	2.260182	0.45	1.00	5	8	0.67	-0.16	0.48

49	2.273420	2.261357	-0.53	1.00	7	8	0.70	-0.18	0.48
50	2.278460	2.285999	0.33	1.00	5	9	0.55	-0.14	0.60

Bulk Modulus= 1.935

c11	c22	c33	c23	c13	c12	c44	c55	c66
3.4842	3.4842	3.4842	1.1608	1.1608	1.1608	0.9765	0.9765	0.9765

d1	d2	d3
0.24690	0.22040	0.18250

loop#10 rms error= 0.2779 %, changed by -.0000660 %

length of gradient vector= 0.000001 blamb= 0.000000

eigenvalues	eigenvectors
0.02620	0.64 0.73 0.23
1.39189	0.77-0.61-0.18
9.16988	-0.01-0.29 0.96

chisquare increased 2% by the following % changes in independent parameters

0.45	1.61	-0.02
0.07	-0.18	-0.10
0.01	-0.02	0.13

Rusout file # 11

$Dy_2Ti_2O_7$ 43.8mg
free moduli are c11, c12, c44, cut along 100
using 10 order polynomials mass= 0.0438 gm rho= 6.889 gm/cc

n	fex	fr	%err	wt	k	i	df/d(moduli)		
1	0.839140	0.834395	-0.57	1.00	4	1	0.02	-0.01	0.99
2	1.020890	1.018126	-0.27	1.00	4	2	0.04	-0.01	0.97
3	1.183560	1.185367	0.15	1.00	6	2	1.09	-0.35	0.25
4	1.208110	1.209303	0.10	1.00	7	2	1.07	-0.33	0.26
5	1.222570	1.223308	0.06	1.00	3	2	0.07	-0.02	0.95
6	1.255290	1.257103	0.14	1.00	2	2	0.08	-0.02	0.94

7	1.329890	1.330927	0.08	1.00	8	2	0.10	-0.03	0.93
8	1.415080	1.411716	-0.24	1.00	1	2	1.16	-0.39	0.23
9	1.448920	1.453025	0.28	1.00	5	1	1.53	-0.53	0.00
10	1.464170	1.462873	-0.09	1.00	6	3	0.78	-0.16	0.38
11	1.509610	1.508319	-0.09	1.00	8	3	0.80	-0.21	0.42
12	1.543340	1.540243	-0.20	1.00	5	2	1.53	-0.53	0.00
13	1.564230	1.564236	0.00	1.00	7	3	0.80	-0.18	0.38
14	1.611840	1.615293	0.21	1.00	2	3	0.90	-0.25	0.35
15	1.615980	1.619601	0.22	1.00	5	3	1.54	-0.54	0.00
16	1.645560	1.642627	-0.18	1.00	1	3	0.71	-0.12	0.42
17	1.661890	1.655559	-0.38	1.00	8	4	0.16	-0.05	0.89
18	1.695750	1.692799	-0.17	1.00	3	3	0.97	-0.27	0.31
19	1.782600	1.785707	0.17	1.00	4	3	0.07	0.00	0.93
20	1.821790	1.816064	-0.31	1.00	5	4	1.22	-0.27	0.05
21	1.867350	1.861017	-0.34	1.00	2	4	0.31	-0.10	0.79
22	1.894310	1.890712	-0.19	1.00	5	5	1.30	-0.31	0.02
23	1.916580	1.907725	-0.46	1.00	6	4	1.07	-0.32	0.25
24	1.924670	1.924334	-0.02	1.00	3	4	0.37	-0.12	0.75
25	1.939080	1.925174	-0.72	1.00	7	4	1.12	-0.35	0.23
26	1.945860	1.937174	-0.45	1.00	1	4	1.25	-0.41	0.16
27	2.004450	2.012234	0.39	1.00	7	5	0.61	-0.18	0.56
28	2.029110	2.037176	0.40	1.00	6	5	0.56	-0.17	0.61
29	2.042380	2.043686	0.06	1.00	1	5	0.81	-0.24	0.42
30	2.151390	2.159587	0.38	1.00	1	6	1.12	-0.35	0.23
31	2.237820	2.243948	0.27	1.00	6	6	0.81	-0.23	0.42
32	2.249640	2.256561	0.31	1.00	7	6	0.92	-0.28	0.36
33	2.261410	2.261862	0.02	1.00	6	7	0.30	-0.08	0.78
34	2.272340	2.274356	0.09	1.00	3	5	0.50	-0.13	0.63
35	2.279600	2.284744	0.23	1.00	2	5	0.51	-0.14	0.63
36	2.288360	2.291697	0.15	1.00	5	6	0.87	0.07	0.05
37	2.345020	2.348212	0.14	1.00	7	7	0.31	-0.08	0.77
38	2.377020	2.380694	0.15	1.00	4	4	0.47	-0.16	0.69
39	2.381280	2.386653	0.23	1.00	8	5	0.44	-0.13	0.69
40	2.425510	2.434592	0.37	1.00	5	7	0.77	-0.22	0.45
41	2.437640	2.446642	0.37	1.00	2	6	0.60	-0.17	0.57
42	2.455050	2.453662	-0.06	1.00	3	6	0.70	-0.20	0.51
43	2.519870	2.519824	0.00	1.00	8	6	0.57	-0.16	0.59
44	2.525210	2.522847	-0.09	1.00	1	7	0.34	-0.09	0.76
45	2.555110	2.553766	-0.05	1.00	4	5	0.56	-0.14	0.58
46	2.581880	2.581697	-0.01	1.00	5	8	0.59	-0.17	0.58
47	2.637580	2.640253	0.10	1.00	1	8	0.66	-0.21	0.54
48	2.684640	2.670362	-0.53	1.00	4	6	0.44	-0.11	0.67

49	2.688360	2.704614	0.60	1.00	5	9	0.71	-0.20	0.49
50	2.734220	2.725549	-0.32	1.00	7	8	0.74	-0.22	0.48

Bulk Modulus= 1.970

c11	c22	c33	c23	c13	c12	c44	c55	c66
3.4666	3.4666	3.4666	1.2213	1.2213	1.2213	0.9738	0.9738	0.9738

d1	d2	d3
0.20480	0.18080	0.17170

loop# 3 rms error= 0.2833 %, changed by -.0000013 %

length of gradient vector= 0.000000 blamb= 0.000000

eigenvalues	eigenvectors
0.03278	0.65 0.72 0.24
1.56329	0.76-0.62-0.19
9.36544	-0.01-0.30 0.95

chisquare increased 2% by the following % changes in independent parameters

0.42	1.37	-0.02
0.07	-0.16	-0.10
0.01	-0.02	0.13

VITA

Yanbing Luan obtained her B.S. in Corrosion and Protection in August 1999 from the University of Science and Technology Beijing (USTB), China. After graduation, she enrolled in the graduate school of USTB and earned her M.S. in Materials Science in March 2002. The title of her thesis was "Assessment, Prediction, Consultation and Decision System of Atmospheric Corrosion of Metallic Materials".

Yanbing Luan came to the United States in July 2002, holding a J-2 visa. She studied at Purdue University's language school ESL for half a year to improve her English. Then in 2003, to enrich her lab experience, she began volunteering work in the Turner Lab of the School of Materials Engineering at Purdue University, where she participated in the research on the synthesis of nanostructured materials by using porous anodic alumina (PAA) as the template.

In August 2005, Yanbing Luan entered the University of Tennessee-Knoxville as a Ph.D. student in Materials Science and Engineering. As a research assistant, she worked on the elastic properties of complex transition metal oxides using Resonant Ultrasound Spectroscopy under the guidance of Dr. Veerle Keppens. She completed her Ph.D. in Materials Science and Engineering in May 2011.